12-12-2014

Structural Characterization of Porous Materials: Understanding Mass Transport through Asymmetric Membranes during Forward Osmosis

Seetha Soundara Manickam
seethasmanickam@gmail.com

ABSTRACT

Structural Characterization of Porous Materials: Understanding Mass Transport through Asymmetric Membranes during Forward Osmosis

Seetha Soundara Manickam, PhD

University of Connecticut, 2014

Engineered osmosis (EO) is an emerging membrane separations-based technology platform comprising of forward osmosis, pressure-retarded osmosis, and direct osmotic dilution/concentration processes. EO relies on a water flux driven across a semi-permeable membrane as a result of osmotic pressure gradients between two solutions, the relatively dilute feed and a concentrated draw solution. However, the support layer in EO membranes presents a resistance to solute transport resulting in internal concentration polarization (ICP) phenomena which results in the actual driving force being far lower than what is available. Severity of ICP is largely influenced by the structure of the support layer in the composite EO membranes. The successful commercialization of EO requires, among other key factors, tailoring of membranes with optimum structures. To this end, there is a flurry of research on the fabrication of novel membranes but no adequate methods to characterize and understand how these structures affect membrane transport. This thesis is among the first few to present efforts to comprehensively characterize EO membrane structures and understand how they relate to transport. New approaches to soft materials characterization have been developed and limitations of traditional approaches have been convincingly proved. Numerical simulation studies have been employed to inform future membrane designers on optimal structures for transport. It is believed that this work is an important step towards understanding and optimizing membrane structure for separations technologies, especially forward osmosis.

Structural Characterization of Porous Materials: Understanding Mass Transport through Asymmetric Membranes during Forward Osmosis

Seetha Soundara Manickam

B.S., Anna University, 2008

M.S., University of Connecticut, 2012

A Dissertation

Submitted in Partial Fulfillment of the

Requirements for the Degree of Doctor of Philosophy

at the

University of Connecticut

2014

2014

APPROVAL PAGE

Doctor of Philosophy Dissertation

Structural Characterization of Porous Materials: Understanding Mass Transport through Asymmetric Membranes during Forward Osmosis

Presented by

Seetha Soundara Manickam, B.S., M.S.

Major Advisor_____

Dr. Jeffrey R. McCutcheon

Associate Advisor_____

Dr. Baikun Li

Associate Advisor_____

Dr. Richard Parnas

Associate Advisor_____

Dr. Ugur Pasaogullari

Associate Advisor_____

Dr. Leslie Shor

University of Connecticut

2014

Acknowledgments

First and foremost, I would like to express my sincere gratitude to my major advisor, Prof. Jeffrey McCutcheon who has been an immense source of support to me for the past 5 years. I thank him for taking me on as his student and for shaping my professional development. The work outlined in this dissertation would not have been possible without his help. I also greatly acknowledge the freedom he granted me in my research projects and for giving me the opportunity to develop professional skills by attending various conferences (Cancun!). I thank him for his patience as he honed my writing and presentation skills and for his empathy during my times of need. Last but not least, I thank him for all his patience and time as he helped me in my job search – he was immensely helpful and I would not have been able to find the opportunity at Phillips 66 if not for him sending me to NAMS this year and helping me develop my skill sets during the course of my PhD. Thank you for everything, Prof. McCutcheon.

I would like to thank my advisory committee members, Profs. Baikun Li, Richard Parnas, Ugur Pasaogullari and Leslie Shor for their time and valuable guidance, especially during my proposal defense. I also wish to thank the faculty members in the Chemical Engineering department for their support during my PhD. I greatly thank Ms. Leah Winterberger, Ms. Susan Soucy and Ms. Marita Decozio-Wiley for all their timely support and guidance during my time here; Leah, thanks for all your help always! I greatly acknowledge the help and favors I've received from Mr. Pete Menard, Mr. Mark Drobney and Mr. Joe Csiki – especially Mark, thanks for all the things you've built for me! I would also like to thank all the folks at C2E2 who've been so very helpful to me as I spent a large amount of my research time at the center. I also gratefully acknowledge the collaborators in all my research projects – Prof. Baikun Li's group, PMI, Jeff Gelb at Xradia and Prof. Guy Ramon at Technion. Special thanks to Jeff for all his support and to Guy who taught me what I know about modeling and for being a great teacher!

I would like to thank all of my labmates – Dan, Jason, Ngoc, Liwei, Jian, Maqsud, Mihdhar, Basma, Mustafa, Alan, Brendan and Kevin for being great friends during my time here and helping me maintain my sanity! You guys were immensely helpful and I gratefully acknowledge the huge role you've played in my grad school life! I especially thank Jason for his timely and valuable help during all the times I've needed help with plumbing the furnace and other odd fixes. I also wish to thank the undergraduate students whom I've mentored during my time here – Breanne, Ali, Gosia, Lior, James and Radhe. They gave me the opportunity to learn how it is to be a mentor and it was fun working with them.

I thank all of my friends, both at UConn and elsewhere who made my life here pleasant and enjoyable. I especially thank Krishna and Shalini who have been huge pillars of support. Shalini, thanks for all the fun times and for being there for me when I needed you the most and for being such a wonderful friend! And thank you for all the job search tips! I cannot begin to thank Krishna enough – I could not have imagined having gotten through grad school life without your

help. You have been wonderfully supportive and been an amazing friend whenever I've needed you. Thank you for all the good times, the food, and your care and for just, everything!!

Finally, I thank my family because of whom I have come this far. They are the pillars of my existence and I am grateful for all their support, love and care. I thank my sisters, Devika and Shobana, Prem, Siththappa and of course, Amma and Appa. I dedicate this thesis to my Appa who is responsible for all the good things that happen to me and is my hero. And of course, Muruga, I thank you – you are the one that makes things happen.

Table of Contents

LIST of FIGURES

Chapter 2. Background and Literature Review

Chapter 3. Activated Carbon Nanofibers Nonwoven as an Anode for Microbial Fuel Cells

Chapter 6. Understanding Variations in Structural Parameters – Fabrication and Testing of Model Membranes

Chapter 7. Impact of Structural Metrics on Membrane Performance – Modeling and Simulation of Transport Phenomena

LIST of TABLES

Chapter 1

Introduction

1.1. Motivation

Water and energy scarcity are two of the biggest issues faced by mankind in the 21st century. Only 2.5% of the earth's water supply is in the form of fresh water sources and of this only 0.3% is in the form of renewable sources. Further, the energy that is needed for accessing these waters comes from sources that are fast depleting. Water, in turn, is a critical raw material for tapping energy sources and thus we are presented with a water-energy nexus where the dependence of one commodity on the other becomes important factors in deciding human survival.

There is a vast amount of both human-generated wastewater and saline water on the earth that, if properly treated, could provide a virtually inexhaustible supply of water. In the case of wastewater, several technologies are already in place that are commercially used to treat waters from different sources. However, in light of the growing energy and water crises there is a need to look toward more sustainable technologies. Microbial fuel cells (MFCs) and engineered osmosis (EO) are two such methods of sustainable treatment of wastewaters and waters, respectively [1]. In MFCs, anaerobic respirations of bacteria growing in a biofilm supported by the anode serve to both break down the complex macromolecules present in the influent wastewater as well as generate electricity by the flow of electrons that are a by-product of the respiration. MFCs hold a lot of promise in making the energy-intensive wastewater treatment process self-supporting. However, there are certain roadblocks in its commercialization, including the development of electrode materials with suitable properties, improved system configuration and so on [2]. Of these, a major concern and thereby, a major research opportunity, has been the development of an anode with suitable substrate properties. The anode that support

the bacterial biofilm needs to possess certain important properties: firstly, it should possess large bio-available surface areas for sufficient biofilm growth and attachment. Secondly, the material should be porous in order to promote enhanced mass transfer for convection in flow-through systems. Thirdly, tt should also have sufficient strength to withstand the weight of the biofilm so that anode fragments do not shed in to the effluent. Finally, in order to function as an electrode the material should be reasonably conductive. In addition to this, the materials should obviously also be non-toxic, adaptable to different system geometries and be scalable and inexpensive in manufacturing. The development, fabrication and characterization of one such novel anode material, activated carbon nanofiber nonwovens (ACNFN) marks the beginning of the research work outlined in this dissertation. The results from this work highlighted the importance of pore structure on transport and ultimately, performance. The remainder of the dissertation then focuses on examining the influence of such pore structures on transport through such materials. Asymmetric membrane structures used in EO were identified as an ideal candidate for this study.

EO is an emerging technology platform for sustainable production of water and energy and comprises a number of membrane-based technologies. These include forward osmosis (FO) [3-7], pressure-retarded osmosis (PRO) [8-10] and direct osmotic concentration [11, 12], which can be used for desalination, power production and dewatering, respectively. These technologies rely on osmotic gradients between a concentrated draw solution and a relatively dilute feed solution. The desired end-product can then be recovered from the diluted draw solution. The absence of hydraulic pressures also lessens the severity of membrane fouling in EO as opposed to that in RO [ref].

Though the concept of EO was first discussed as early as the mid-1960's only in the last decade has there been renewed interest in this technology with the development of several novel

membranes and the engineering of new draw solutions [ref]. Critical to the success of the EO technology is the development of a membrane structure that can mitigate the detrimental effects of internal concentration polarization (ICP) which is one of the significant impediments to the commercialization of EO [ref]. EO membranes typically consist of an ultra-thin selective layer, which performs the actual selectivity function, supported on a porous layer that provides mechanical support. The porous support is further backed by another nonwoven layer providing additional integrity [ref]. ICP signifies the resistance to solute transport offered by the membrane support structure. It causes the actual driving force for transport to be far lower than the available driving force. The influence of the membrane structure on the severity of ICP is commonly denoted by a metric known as the intrinsic structural parameter, S_{int}, given as $t\tau/\varepsilon$ where t is the thickness, τ, tortuosity and ε, porosity of the membrane structure. Thus, structure-performance relationships play a crucial role in membrane performance in EO. Most EO membranes have complex structures that are not easily characterized by the methods already available. The absence of suitable characterization approaches for soft materials leads to a dearth of reliable information of the influence of membrane structure on transport in EO processes. This dissertation outlines work on understanding the impact of asymmetric membrane structures on mass transport in osmotically-driven separations. Specifically, protocols have been developed for characterizing porous soft materials and the utility of porous materials characterization has been demonstrated using a model membrane. Finally, the influence of individual structural features on transport in asymmetric membranes using mass transfer models has been examined. **1.2. Objectives and Scope of Dissertation**

The overall goal of the research outlined in this dissertation is to demonstrate the use of characterization techniques in order to better understand structure-performance relations in EO

membranes and to inform future membrane designers on achieving optimal performance through tuning of structural metrics.

Specific objectives include:

1. Fabricating and characterizing ACNFN as a novel anode for MFCs. The unique structure of ACNFN is expected to influence the performance of this material.

2. Explore the use of different characterization techniques for soft materials using polymeric nonwovens, commonly used as backing layers in TFC membranes, as a platform material.

3. Use the developed characterization approaches to determine the intrinsic S values of TFC membranes.

4. Explain in detail the deviation of "effective" S values from intrinsic S values via the fabrication and characterization of model TFC membranes.

5. Numerical modeling and simulation of FO membrane transport to clearly elucidate the role of different structural metrics on performance.

1.3. Dissertation Organization

Chapter 2 provides a brief literature review of the techniques commonly used to characterize soft materials and a detailed background of the motivation for the work outlined in this dissertation. Both analytical (capillary flow porometry, liquid extrusion porosimetry and mercury intrusion porosimetry) and imaging (x-ray computed tomography) are discussed in this chapter. The operating principles, advantages, disadvantages and applicability of the different techniques are discussed in detail. A review of semi-empirical methods commonly used to characterize EO membrane structures are also provided.

Chapter 3 describes the development, fabrication and characterization of ACNFN as a novel anode material for MFCs. ACNFN is proposed as a high "bioavailable" surface area anode material with superior mass transport properties owing to its open, porous structure [ref]. ACNFN was fabricated by pyrolysis and physical activation of an electrospun polyacrylonitrile precursor. The material was then characterized to evaluate its physico-chemical characteristics. Electrochemical testing in a single chamber MFC revealed that ACNFN far outperformed two other conventional anode materials, granular activated carbon and carbon cloth, in terms of sustained voltage generation and current densities produced. The impressive performance of ACNFN is attributed to its open porous nonwoven structure, favorable for mass transport. Structure-performance relationships are identified as being crucial to the successful application of such porous materials.

The next step in this work was then to evaluate the structure-performance relationships in nonwovens using a suite of characterization techniques. Nonwovens present an ideal platform for such a study since they their structures are relatively simple enough to reasonably capture idiosyncrasies in the different techniques while also being able to evaluate a range of different structural metrics. Furthermore, nonwovens are used as backing layers in TFC membranes used in EO. This is outlined in **Chapter 4** which introduces the use of a new technique to characterize soft materials, x-ray computed tomography (XCT), and discusses its pros and cons versus that of a more traditional technique, mercury intrusion porosimetry (MIP) [ref]. Both commercial polyester nonwovens as well as electrospun polyacrylonitrile nanofibers were evaluated in this study. The applicability, pros and cons of the different techniques in characterizing soft materials were understood.

From the previous study, it was possible to evaluate different characterization techniques for soft materials as well as to characterize nonwovens that form part of the TFC membranes used in EO. In **Chapter 5** these techniques were extended to entire TFC membrane structures, consisting of nonwoven backing layers, and these were characterized using two of the techniques explored in Chapter 4. Specifically, two TFC RO membranes from Dow Water and Process Solutions were tested in this study using MIP and XCT. Structural metrics were calculated and for the first time in membrane literature, the intrinsic S values of TFC membranes were calculated [ref]. These values were then compared to the effective S values and the discrepancies explained and evaluated. Non-wetting of the hydrophobic polysulfone support in osmotic flux tests leading to artificially enhanced S_{eff} values were recognized as being a possible issue.

Chapter 6 then deals with circumnavigating this issue by fabricating and characterizing a model TFC membrane made from a hydrophilic support [ref]. Track-etched membranes were used as a support and *in-situ* interfacial polymerization was performed to form a polyamide layer on this support. The intrinsic S value was simply calculated using SEM measurements and effective S values, at different draw solution concentrations and in the two membrane configurations (FO and PRO mode), were calculated from osmotic flux tests and the resulting differences were examined in detail. It was experimentally validated that current empirical models to calculate S_{eff} do not fully capture the different resistances to transport across the membrane and thus do not accurately quantify its structure and that these simplifying approaches are often times severely flawed. In such a scenario there exists a need to develop a method to determine how exactly the support layer contributes to mass transport resistance.

This is then the focus of **Chapter 7** where the influence of different structural metrics on support layer transport is examined [ref]. A numerical simulation approach is used for this since this can

serve as a relatively rapid method of evaluating the effect of different parameters on a given process. The influence of different structural metrics like support pore radius, support porosity and support thickness along with the effect of varying draw and feed concentrations were studied. Flux performance is largely affected by ICP and thus membrane structure optimization efforts should focus on effective ways of mitigating this detrimental phenomenon. This was seen to be best done by decreasing support thickness over either increasing porosity or support pore radius. The results also indicated that there is a need to look beyond the traditional optimization of thickness, tortuosity and porosity as even parameters like support pore radius, which do not feature in the intrinsic structural parameter formula, seem to affect performance to a non-insignificant degree. The simulated results yielded interesting insights on the impact of support layer properties that can inform future osmotic membrane designers on the parameters that would benefit from optimization for enhanced flux performance.

Chapter 8 is an outlook on the challenges and opportunities available for structural characterization in both membranes for EO as well as soft materials beyond this application. Some thoughts on suggested optimal structural metrics for EO membranes are also presented as well as future areas of work that would benefit emerging membrane-based separation technologies.

1.4. Novel Contributions

This dissertation contributes to the general understanding of structures of soft materials and its influence on transport in osmotic processes. The specific contributions are listed below:

1. *Proposed the use of ACNFN as a novel anode material for MFCs.* The use of carbon nanofibers-based nonwovens was proposed as an anode material in MFCs. The material's

structure was clearly seen to be crucial in determining performance lending an impetus to the comprehensive study of soft material structures, an area largely ignored.

2. *Developed characterization approaches for examining soft materials*. The applicability, pros and cons of novel analytical and imaging techniques were studied in detail. A new non-destructive 3D imaging tool, XCT, was introduced as a novel way of characterizing soft materials. This work demonstrated the utility of porous materials characterization in understanding complex asymmetric membrane structures.

3. *Developed methods to accurately characterize structural parameters of TFC membranes.* This study was also the first to experimentally prove that there are discrepancies between intrinsic and effective S values.

4. *Demonstrated inaccuracies in existing structural parameter measurement methods.* A model TFC membrane whose intrinsic S value could be determined a priori by using a well-characterized track-etched membrane as a support. This also represents the first time a TFC membrane had been fabricated using a track-etched membrane.

5. *Developed 3D numerical simulations that illustrated concentration gradients in asymmetric membranes during osmosis.* The influence of different structural metrics on support layer transport phenomena in FO processes was studied using numerical simulations. The results indicated that there is a need to look beyond the traditional optimization of thickness, tortuosity and porosity as even parameters like support pore radius, which do not feature in the intrinsic structural parameter formula, seem to affect performance to a non-insignificant degree.

1.5. References

1. Liu, H., R. Ramnarayanan, and B.E. Logan, *Production of Electricity during Wastewater Treatment Using a Single Chamber Microbial Fuel Cell.* Environmental Science and Technology, 2004. **38**(7): p. 2281-2285.
2. Torres, C.I., A.K. Marcus, and B.E. Rittmann, *Proton transport inside the biofilm limits electrical current generation by anode-respiring bacteria.* Biotechnology and Bioengineering, 2008. **100**(5): p. 872-881.
3. Cath, T.Y., N.T. Hancock, C.D. Lundin, C. Hoppe-Jones, and J.E. Drewes, *A multi-barrier osmotic dilution process for simultaneous desalination and purification of impaired water.* Journal of Membrane Science, 2010. **362**(1): p. 417-426.
4. Choi, Y.-J., J.-S. Choi, H.-J. Oh, S. Lee, D.R. Yang, and J.H. Kim, *Toward a combined system of forward osmosis and reverse osmosis for seawater desalination.* Desalination, 2009. **247**(1): p. 239-246.
5. Kessler, J.O. and C.D. Moody, *Drinking water from sea water by forward osmosis.* Desalination, 1976. **18**(3): p. 297-306.
6. Martinetti, C.R., A.E. Childress, and T.Y. Cath, *High recovery of concentrated RO brines using forward osmosis and membrane distillation.* Journal of Membrane Science, 2009. **331**(1): p. 31-39.
7. McCutcheon, J.R., R.L. McGinnis, and M. Elimelech, *A novel ammonia-carbon dioxide forward (direct) osmosis desalination process.* Desalination, 2005. **174**(1): p. 1-11.
8. Lee, K.L., R.W. Baker, and H.K. Lonsdale, *Membranes for power generation by pressure-retarded osmosis.* Journal of Membrane Science, 1981. **8**(2): p. 141-171.
9. Sepp□l□, A. and M.J. Lampinen, *Thermodynamic optimizing of pressure-retarded osmosis power generation systems.* Journal of Membrane Science, 1999. **161**(1): p. 115-138.
10. Skilhagen, S.E., J.E. Dugstad, and R.J. Aaberg, *Osmotic power - power production based on the osmotic pressure difference between waters with varying salt gradients.* Desalination, 2008. **220**(1): p. 476-482.
11. Garcia-Castello, E.M. and J.R. McCutcheon, *Dewatering press liquor derived from orange production by forward osmosis.* Journal of Membrane Science, 2011. **372**(1): p. 97-101.
12. Jin, X., J. Shan, C. Wang, J. Wei, and C.Y. Tang, *Rejection of pharmaceuticals by forward osmosis membranes.* Journal of hazardous materials, 2012. **227**: p. 55-61.
13. Manickam, S.S., J. Gelb, and J.R. McCutcheon, *Pore structure characterization of asymmetric membranes: Non-destructive characterization of porosity and tortuosity.* Journal of Membrane Science, 2014. **454**: p. 549-554.
14. Cath, T.Y., M. Elimelech, J.R. McCutcheon, R.L. McGinnis, A. Achilli, D. Anastasio, A.R. Brady, A.E. Childress, I.V. Farr, N.T. Hancock, J. Lampi, L.D. Nghiem, M. Xie, and N.Y. Yip, *Standard Methodology for Evaluating Membrane Performance in Osmotically Driven Membrane Processes.* Desalination, 2012. **312**(0): p. 31-38.
15. S Manickam, S. and J.R. McCutcheon, *Characterization of polymeric nonwovens using porosimetry, porometry and X-ray computed tomography.* Journal of Membrane Science, 2012. **407**: p. 108-115.
16. Wong, M.C.Y., K. Martinez, G.Z. Ramon, and E. Hoek, *Impacts of operating conditions and solution chemistry on osmotic membrane structure and performance.* Desalination, 2012. **287**: p. 340-349.

Chapter 2

Background and Literature Review

Abstract

Asymmetric membranes are used in several membrane separations like ultrafiltration, nanofiltration, reverse osmosis and engineered osmosis (EO), to name a few examples. The first three are pressure-driven technologies in which separation is mainly driven by the selective layer and the support layer mostly only provides mechanical support. In EO, however, the support layer plays a crucial role in determining performance. There have been several studies on understanding the influence of support structures on membrane fabrication, compression behavior and transport phenomena. This review summarizes work in this area with a focus on structure-transport relationships. Both semi-empirical models and structural characterization techniques are used to understand this behavior. The use of numerical models has long been the most popular approach, though it has certain limitations because of the differences in methods and assumptions used by different researchers. Direct structural characterization of membranes is a newer and promising concept, however again there are some limitations. A timeline of numerical model development is presented along with their utility and limitations. Analytical and imaging characterization techniques are also summarized, detailing their operating principles, pros and cons in evaluating soft materials. Finally, suggestions for future research in this area that would benefit the community are also presented.

2.1. Introduction

2.1.1 Asymmetric membranes in membrane separations technologies

Asymmetric membranes are used in a number of membrane-based technologies for both gas and liquid separations. Specifically, in the field of liquid separations, these membranes are used in ultrafiltration (UF), nanofiltration (NF), reverse osmosis (RO) and engineered osmosis (EO). The first three are pressure-driven technologies in which the use of asymmetric membranes is well-studied and the last one is an emerging technology for sustainable production of power and water. Membrane structures and chemistries vary for these different applications based on process needs but overall, membrane types can be classified into integrally-skinned and thin-film composite (TFC) platforms. The former has low permselectivities and is now-a-days mostly only used in UF applications whereas NF, RO and EO employ heavily the TFC design. Both membranes have a "skin" or selective layer that performs the actual separation function, supported on a porous layer that provides mechanical integrity and support. Membrane design for these processes, and hence the resulting structure, is dictated by the specific needs and varies widely between UF, NF/RO and EO.

2.1.2 Asymmetric membranes in pressure-driven applications

In case of pressure-driven applications like UF, NF and RO, a hydraulic pressure gradient is applied as the driving force for separation that causes certain solutes to be retained by the semipermeable membrane while other solutes and solvents pass through as permeate. In these processes, the separation (permselectivity) is governed almost entirely by the selective layer and the support layer does not play an active role here. In semipermeable asymmetric membranes for liquid separations, the selective layer is either made of the same polymer as the support layer (in

case of integrally-skinned membranes) or is made of a different polymer which has optimal separation properties [1] in case of composite membranes. Transport though this layer is thought to occur entirely by the solution-diffusion mechanism [2, 3] and in order to reduce resistance to this transport, and this ultimately enhance performance, it is desired that the selective layer be as thin as possible. Fabrication of this selective layer occurs along with that of the support layer in case of integrally-skinned membranes, by a process known as phase inversion [1]. For TFC membranes, the selective layer can be made from a number of different methods, viz. *in-situ* interfacial polymerization, spin coating or float casting, plasma polymerization [1] and layer-by-layer deposition [1, 4-7]. Of these, *in-situ* interfacial polymerization is the most popular method and usually involves fabrication of an aliphatic or aromatic polyamide thin-film by a polycondensation reaction on the porous support. Reaction conditions, chemistries and kinetics are the key factors influencing selective layer formation and hence, membrane performance and thus are almost always the parameters of interest to membrane scientists.

The role of the support role was previously only thought to be limited to membrane fabrication where its chemistry and structure determined the "workability" of the membrane in the intended application [8, 9]. Numerical simulation studies by Ramon and coworkers in 2012 [10] however revealed that the support plays a more significant role than previously thought. Support pore size and porosity were shown to affect water flux and solute rejection in NF, brackish water RO and seawater RO membranes. Further, it was suggested that support layer properties also influence permeability and fouling behaviors. However, this was not entirely startling since the effect of support layers on TFC membrane performance had been discussed by Lonsdale et al. over four decades ago [11]. Despite this and other studies it remains that membrane fabrication for pressure-driven applications focuses mostly on optimizing the

properties of the selective layer. There are some novel support layer morphologies and chemistries being developed, for instance for RO desalination applications [12], but much of the membrane fabrication processes for commercial use are now secretive and protected by licenses with the manufacturers.

2.1.3 Asymmetric membranes in osmotic processes

2.1.3.1 Engineered osmosis

EO represents a membrane separations-based technology platform that has applications in diverse fields. EO consists of a number of subset technologies, classified based on differences in operating principles and desired end-products. Namely, these are forward osmosis, FO (applications in desalination, treatment of contaminated waters and wastewaters), pressure-retarded osmosis, PRO (salinity gradient power, energy storage devices), direct osmotic concentration, DOC (treatment of sensitive solutions like certain foods, juices and pharmaceutical solutions, direct potable reuse systems) and direct osmotic dilution, DOD (point-of-use water systems, for e.g. in outdoor and emergency relief situations, with contaminated water sources etc.). In EO, a water flux is driven across a semipermeable membrane as a result of osmotic pressure gradients between two solutions, the relatively dilute feed and a concentrated draw solution. As with all other membrane separations processes, permselectivity of the membrane is one of the critical factors influencing both separation as well as water flux performance. To this end, a major area of study has been on membrane design and optimization [6, 13-21], the other fields being engineering of draw solutions [22-26] and design of membrane systems and configurations [27-30].

2.1.3.2 Membranes for EO

Asymmetric membrane design and fabrication began as early as the 1960's with the prototype integrally-skinned membranes made by the Loeb-Sourirajan process [31]. These cellulose acetate membranes made by phase inversion had a selective skin layer, performing the actual separation process, supported on a porous layer, both made of the same polymer. While these membranes revolutionized the desalination industry by becoming first reverse osmosis (RO) membranes used [3], they also had their share of limitations. The most important one was poor permselectivities owing to their thick skin layers [9]. Further, since both the skin and the support were made from the same polymer, these layers could not be individually optimized to tune their properties [1]. Also, this limited the kinds of polymers that could be used to make these membranes, with only a handful of options available [1]. Of those, the most popular was cellulose acetate which unfortunately had disadvantages of undergoing hydrolysis [1, 12] and exhibiting osmotic de-swelling at high solute concentrations [32, 33]. This resulted in the advent of the thin-film composite (TFC) membrane design that is now the workhorse of the RO industry. TFC membranes consist of an ultrathin selective layer, usually made of polyamide, supported on a porous layer, that can be made from a number of polymers, that is further backed by either a porous nonwoven (usually) or woven (rarely) layer. First generation EO studies simply used existing TFC RO membranes with the intention of benefiting from decades-long research and development efforts invested in fabricating those membranes [28, 34-36]. However, these studies all reported far lower fluxes than what was expected based on the available driving force [28, 34-36]. This was because of a principal difference in the applied driving force between RO and EO – osmotic gradients between two solutions in EO versus hydraulic pressure applied on a single stream in RO.

2.1.3.3 Concentration polarization in EO and the structural parameter

Support layers in TFC RO membranes are relatively thick, tortuous structures with modest porosities [37]. In EO, either draw (in FO) or feed (in PRO) solutes need to transport freely through the support structure in order for the available driving force to be realized at the selective-support layer interface. However, unfavorable support structures present a resistance to solute transport resulting in internal concentration polarization (ICP) phenomena which results in the actual driving force being far lower than what is available. Severity of ICP is largely influenced by the structure of the support layer, commonly denoted by a metric known as the intrinsic structural parameter, S_{int}. S_{int} is given as

$$S_{\text{int}} = \frac{t\tau}{\varepsilon} \qquad (2.1)$$

where t is the thickness, τ is the tortuosity, and ε is the porosity of the support layer. Obviously, membranes with low S_{int} values are preferred in order to reduce the severity of ICP. To this end, there has been an intense research thrust towards the development and fabrication of novel membrane structures for EO since the 1990's [38]. Alongside this, there have also been concurrent efforts on developing methods to compare and contrast the different membranes made using the structural parameter concept. To calculate S_{int} using Eqn. 1 we would need to independently estimate the three structural metrics. While thickness can be easily determined using either a micrometer or cross-sectional images of the membrane, it is a challenge to accurately estimate porosity and more so, tortuosity. This is because pore structure characterization of soft materials is currently an underdeveloped field, with no known approaches for comprehensively characterizing 3D structures. Thus, the EO community commonly uses numerical models to calculate an *"effective"* structural parameter (S_{eff}) rather than estimating the *"intrinsic"* value.

2.1.4 Use of numerical models to calculate effective structural resistances

To calculate an effective structural parameter, empirical models based on experimental flux measurements are used that are derived from the flux governing equation,

$$J_w = A(\sigma \Delta \pi_m - \Delta P) \qquad (2.2)$$

where J_w is the water flux, A is the water permeance of the membrane, σ is the reflection coefficient, $\Delta\pi_m$ is the osmotic pressure gradient across the membrane selective layer and ΔP is applied hydraulic pressure gradient.

Using the van't Hoff approximation for dilute solutions, the osmotic pressure terms are assumed to be linearly proportional to the concentrations thus expressing Eqn. 2.2 in terms of concentrations. These membrane interface concentrations are then expressed in terms of the bulk solution concentrations after correcting for boundary layer resistances using concentration polarization (CP) moduli. These CP moduli are derived from film theory principles,

$$CP\ modulus\ =\ \exp\left(\frac{J_w}{k}\right) \qquad (2.3)$$

where the mass transfer coefficient k is further given as

$$k = \frac{D}{\delta} = \frac{D_s \varepsilon / \tau}{\delta} \qquad (2.4)$$

Here, D is the solute diffusivity in the boundary layer, D_s is the solute diffusivity in free space and δ is the film thickness which becomes the support layer thickness in case of the ICP modulus. In this way the effective boundary layer (film) thickness becomes the structural parameter in the ICP modulus. Since real membranes are not perfectly selective corrections have

to be made for solute permeation. This is done using the equation for reverse solute flux through the membrane,

$$J_s = B\Delta C_m = B(C_{D,m} - C_{F,m}) \qquad (2.5)$$

here, J_s is the reverse solute flux, B is the solute permeability coefficient of the membrane and subscripts D and F correspond to the draw and feed solutions, respectively. Writing a solute mass balance over the membrane and equating it to Eqn. 2.5, for $C_{D,m}$ and $C_{F,m}$ can be solved for, using a few boundary conditions. This enables one to calculate the structural parameter indirectly, as a fitted parameter, as the resistance to transport caused by the support layer. This approach, while feasible, has some inherent limitations which are outlined below.

1. The biggest criticism of the empirical method of calculating S_{eff} has been that this approach lumps the different transport resistances across the membrane into one single parameter, thus effectively making the true resistance to transport caused by the support layer alone indistinguishable from the others. Fig. 2.1 is a schematic demonstrating the different resistances to transport, in series, across an asymmetric membrane. While the two external concentration polarization regions (R_1 and R_6) can be accounted for using film theory principles (Eqn. 2.3 and 2.4), till date there exist no models that distinguish selective layer resistances (R_2, R_3 and R_4) from the support layer resistance, R_5. The resistance to water sorption (R_2), or partitioning, into the selective layer, is generally ignored for hydrophilic polymers or simply lumped in with diffusive transport resistance through the selective layer (R_3) that is assumed to occur by the solution-diffusion mechanism [11]. Desorption from the selective layer (R_4) and internal CP (R_5) is more complicated, however, since they are directly impacted by the membrane structure. Overall, selective layer resistances do not feature in the intrinsic structural

parameter equation (Eqn. 2.1) and thus their incorporation in S_{eff} means that comparison of different membrane supports on such a basis is unfair and flawed.

Furthermore, the empirical models assume that the resistance R_5 is based solely on bulk structural properties of the support layer (bulk porosity and tortuosity). However, as Fig. 2.1 suggests, three independent resistances exist on the support layer side of the membrane (R_4, R_5 and R_6), only one of which (R_5) is dependent on these characteristics. From a perspective of developing better approaches for membrane and system design, these resistances need to be decoupled from one another. Even in the case of R_5, bulk property evaluations have limited use. For instance in the case of porosity, the *surface* porosity of the support layer plays a critical role at the interior interface of the selective layer. For water to desorb from the selective layer, it must do so at a surface pore in the support layer. This results in a longer diffusion pathway, thus increasing the effective thickness of the selective layer and reducing permeance. Possibly the only study that describes this phenomenon is from Lonsdale in 1971 [11]. This phenomenon is also discussed very briefly in a textbook by Mulder [1], where a simplistic model describing effective thickness is presented as a function of surface porosity of a TFC membrane support. Such features, that can have a significant impact on membrane design, are not incorporated in the empirical models.

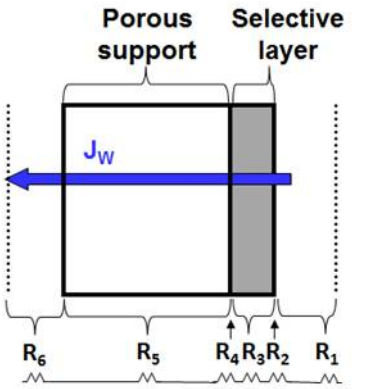

R_1	External concentration polarization
R_2	Sorption into selective layer
R_3	Diffusion through selective layer
R_4	Desorption from selective layer
R_5	Internal concentration polarization
R_6	External concentration polarization

Fig. 2.1. Illustration of mass transfer resistances in series for osmotic flow across asymmetric EO membranes with the membrane oriented in FO mode.

2. Assumption of van't Hoff's equation (π=iCRT) is strictly valid only for dilute solutions which may not always be satisfied. It is typically assumed that ICP causes significant dilution of concentrated solutions to an extent where this simplifying assumption can be used. However, even in cases where only modest draw concentrations were used, this assumption has shown to be flawed [39, 40]. Park et al. [41] investigate this assumption in their study where they used a finite element method-based numerical model to solve for a constant structural parameter and showed that the assumption of van't Hoff's equation tends to cause inconsistencies in the S values calculated.

3. The effective structural parameter is calculated from experimental flux measurements and thus is made to be a function of test conditions rather than membrane structural metrics. This means that any errors in experimental measurements will be reflected in the estimated S_{eff} value

as well. Unless uniform test conditions are used to test different membranes making a comparison between those supports would be invalid.

4. Related to the above point is the fact that the fitted parameter approach uses selective layer properties (A and B) in its calculations. These are typically obtained from RO tests, where unlike in FO, a hydraulic pressure is applied to the selective layer that may result in slightly different transport behavior in RO than in the latter. This approach also requires that the membranes be 'tight' with high salt rejections. This point has been contented from as early as 1976 when Loeb [42] mentioned the need for verifying if membrane water permeance (A) was the same in RO and PRO, to early 2010's [37, 43]. Loeb and his coauthors later verified that to be true in part two of their publication [44] but this was done using deionized water as the feed (no ICP) and assuming no solute leakage (i.e. B=0). Further, PRO is somewhat similar to RO in that both cases involve pressurizing the stream flowing along the selective layer side. This is not the case in FO, meaning that selective layer transport properties could be different between FO and RO. Until now, the RO method remained the only way of determining A and B. Tiraferri et al. recently proposed a new method of measuring A and B solely from FO flux measurements [45]. Their work showed that selective layer properties calculated from RO can be quite different from that calculated from FO tests with the ratio of $(A/B)_{FO}$: $(A/B)_{RO}$ ranging from 40 to 120% for commercial and lab-made TFC membranes. However, their method is yet to gain widespread adoption with the estimates from it being systematically different from the standard method [46].

Despite these drawbacks, it remains that semi-empirical methods are the most popular in the EO community due to their simplicity. It should be mentioned that in a rough sense, the fitted parameter approach enables one to assess the resistance to transport caused by the membrane structure in "real time" since the flux measurements would incorporate effects such as

swelling/de-swelling, for instance, that the membrane experiences during operation. The method, at best, serves this purpose however its use can result in erroneous results when it is used to compare different membranes or even evaluate the same membrane under different circumstances [33, 47-49]. Unfortunately, that is exactly the situation in an evolving field like EO where new membranes are being developed by the month by various research groups across the globe.

2.1.5 Use of pore structure characterization to determine intrinsic structural properties

In the pursuit of addressing needs to understand structure-transport-performance relationships in asymmetric membranes, work on using pore structure characterization methods have recently begun to emerge. At the outset structural characterization of soft materials is an underdeveloped field with several challenges in terms of the applicability and utility of commonly-used techniques. The approach developed should first of all, be capable of three-dimensional characterization since almost all asymmetric membranes have complex structures that exhibit anisotropy in both 2D and obviously, 3D as well. Secondly, the technique used should not alter or affect the membrane structure in any significant way – in other words the technique should not lend undesirable biases during measurements. Finally, the method should yield reproducible results and as much as feasible, be relatively simple to use. There are various parameters of interest to be calculated – for instance, in order to estimate the intrinsic S value, bulk structural metrics like porosity and tortuosity are needed and for a more thorough analysis, structural information on differential element sizes would be helpful. Additionally, pore diameter and pore geometry are also of interest since the former has been identified as influencing selective layer formation [8, 10, 11, 50, 51] and the latter, ICP phenomena [18].

Work in this area has involved both conventional characterization techniques, such as scanning electron microscopy (SEM) and porosimetry as well as newer, more novel tools like electrochemical impedance spectroscopy (EIS) and x-ray computed tomography (XCT). In this review, the operating principles, applicability (to soft materials), pros and cons of the methods used thus far have been summarized.

Overall, this article is a review on impact of support structures on asymmetric membrane fabrication and performance (Section 2.2) and methods, both indirect and direct, used to characterize asymmetric membranes (Section 2.4 and 2.5, respectively). It is to be noted that the review of the "indirect" methods (viz. the use of numerical models) is geared entirely toward membranes for osmotic processes. Specifically, Section 2.1.4 and Section 2.4 are relevant entirely only to osmotic processes, although some of the equations describing transport could be extrapolated to other membrane processes as relevant. However, the reader should exercise caution if doing so as no straightforward comparisons are suggested therein. The direct method, involving pore structure characterization, is relevant to both osmotic membranes and membranes for pressure-driven separations as well and is outlined in Section 5. We hope the readers will be able to navigate this review accordingly without much effort.

2.2. Importance of support layer structure in asymmetric membrane fabrication

The importance of support layer structures in the fabrication of asymmetric membranes is well known to membrane scientists and manufacturers although detailed investigations on this topic have been few and far. As mentioned in Section 2.1.2, in the case of membranes for pressure-driven applications, research has almost always focused on the selective layer with considerations on the support layer being typically limited to its thermal and chemical stability

and mechanical properties [1]. Petersen [9] provides a good review of TFC RO membranes, for instance, that highlights the importance of chemistry and composition of membrane polymers on performance. The influence of support *structure* on membrane fabrication was in fact first acknowledged back in 1971 by Lonsdale et al. [11] who put forth ideas of the influence of pore spacing on diffusive film transport. A schematic from their publication is shown in Fig. 2.2 where it is seen that farther from the pore, the diffusing solvent needs to travel longer distances to reach the mouth of the pore, effectively increasing the "thickness", and hence decreasing the permeability, of the thin-film.

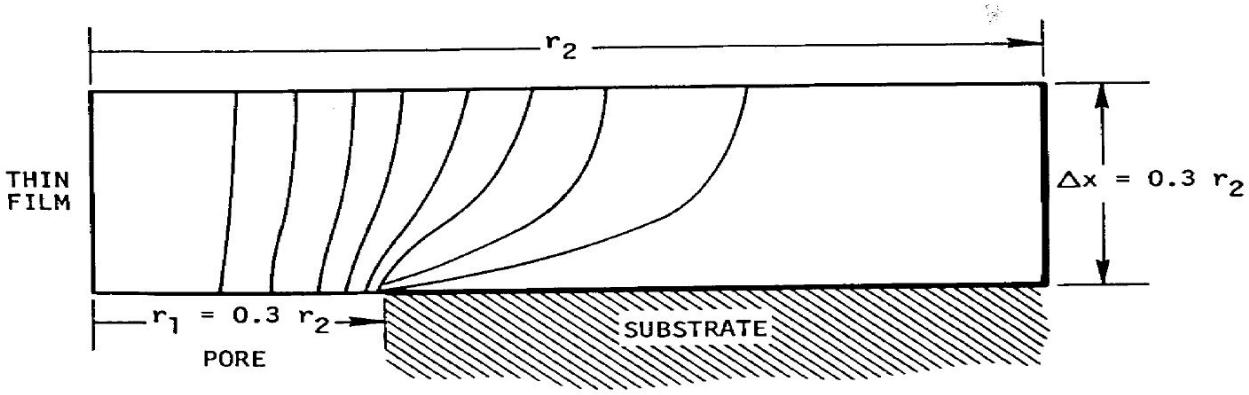

Fig. 2.2. Impact of support layer pore spacing on film transport – cross section of a thin-film over one-half of a pore (cylindrical symmetry exists), with flow contour lines depicting diffusive transport. Farther from the pore, the diffusing solvent needs to travel longer distances to reach the mouth of the pore, effectively increasing the "thickness", and hence decreasing the permeability, of the thin-film. Figure taken from [11].

This theory clearly depicted the importance of support pore morphology on transport but there were no significant, thorough analyses on these ideas until perhaps 2006 when Singh et al. [51] probed the structural variations of thin-film composite RO membranes obtained by coating polyamide over polysulfone membranes of different pore dimensions. They found that between the two pore sizes they studied (0.07 and 0.15 μm) the smaller pore sizes produced two-fold thicker skin layers due to reduced penetration of polyamide into the pores of polysulfone

support. The bigger pores produced thinner films however, that led to the possibility of higher degree of defects and consequently, lower salt rejection efficiency. In 2009, Ghosh and Hoek [8] studied the effect of support membrane structure, along with chemistry, on polyamide–polysulfone interfacial composite membranes. They found that support layer pore morphology and chemistry together affected the properties of the polyamide selective layer formed by interfacial polymerization. More permeable, hydrophilic supports were seen to produce low permeability composite membranes, whereas highly porous, relatively hydrophobic supports were observed to produce more permeable composites. A conceptual model was proposed to explain the effect of polysulfone support properties on the kinetics of the polycondensation reaction and how that affected the characteristics of the resulting film. Ramon et al. [10] later extended this study track to NF, brackish water RO and seawater RO using numerical simulations of a membrane transport model. Among their other results summarized in Section 1.2, they also found that diffusivity of the permeating species, influenced by the morphology of the microporous phase of the support material, may contribute to the overall permeability of the composite membrane. Their numerical study suggested, for the first time, that the local permeate water flux through composite membranes was dictated by support membrane pore morphology, creating localized high flux "hot spots" with potentially high fouling and scaling propensity.

Similar studies on FO membranes have also been done with phase inversion cast support layers. Tiraferri et al. [18] related the role that solvent quality, dope polymer concentration, fabric (backing) layer wetting, and casting blade gate height played in the support layer structure formation to the flux and solute performance of TFC membranes. They used cross-sectional SEM images to characterize the support layer pore morphology and concluded that the optimal FO membrane should consist of a mixed-structure support layer, where a thin sponge-like layer

sits on top of highly porous macrovoids. Shi et al. [50] performed a study on UF-type phase inversion cast supports for hollow fiber FO membranes and summarized that substrates with <300 kDa molecular weight cut-off (MWCO) should be preferred to obtain a "good" semipermeable skin. They further state that would be wiser to use the MWCO value rather than the mean pore size to check the suitability of a substrate for interfacial polymerization. Recently, Manickam et al. [ref] used a numerical simulation approach to solve an FO transport model describing transport processes in the film and pore and studied the effect of various support metrics (viz. pore diameter, porosity and thickness) on the severity of ICP. They found that of the parameters varied, changing support layer thickness had the most prominent effect on transport, with a reduction in its value causing a significant enhancement in performance. It is to be noted that this was experimentally observed by Bui et al. [52] on work with nanofiber-based TFC FO membranes. Furthermore, support pore diameter, that was thus far typically considered to have an effect on only formation of the selective layer, was shown to influence ICP effects as well. This is interesting in light of the fact that this parameter does not actually feature in the intrinsic structural parameter formula (Equation 1) and thus is not a metric that would be thought of as explicitly influencing pore transport behavior.

2.4. Use of numerical models to calculate effective structural parameter

Section 2.1.4 outlined the basic equations that serve as the template for building any model describing transport in osmotic processes. There have been several iterations and variations of this template since the first model was developed in 1976 by Loeb [42]. This section summarizes the significant stages of model development, in FO and PRO, from 1976 – 2013.

Basic model describing transport in a PRO process, Loeb, 1976 [42]

Loeb is credited with developing the first model describing transport in a PRO process in his publication detailing work on evaluating technical and economic correlations of producing energy from concentrated brines. He studied the PRO process using an aromatic polyamide-based hollow fiber module and presents his transport model as below (Equation 9 in the reference article):

$$J_1 = A[\pi_{sh} - (P_{sh} - P_{bo}) - \pi_{bo} \exp(J_1 \Delta X / D_{2ps})] \qquad (2.6)$$

where J_1 is the water flux, P is the hydraulic pressure, ΔX is the thickness of the membrane, D_{2ps} is the solute diffusivity in the porous substructure (support layer) and subscripts *sh* and *bo* refer to the streams in the shell (draw) and bore (feed) side of the hollow fibers, respectively. It is to be noted that this seminal work did not include the effects of reverse solute flux and ECP. These are not grave concerns in membranes with low fluxes that are typical of early osmotic membranes, however it is to be remembered that PRO processes typically have relatively high fluxes.

Extension of Loeb's model by Lee et al., 1981 [34]

Perhaps the most cited early work on osmotic transport models is the publication of Lee et al. where the model developed by Loeb in 1976 (Eqn. 6) was extended to include the effects of reverse solute flux. However, here too the effects of ECP were not considered assuming efficient stirring conditions. The equation for predicting water flux in a PRO process was given as (Equation 10 in the reference article)

$$J_w = A\left[\pi_2 \frac{1-\frac{C_4}{C_2}\exp(J_w K)}{1+\frac{B}{J_w}[\exp(J_w K)-1]} - \Delta P\right] \qquad (2.7)$$

where π_2 is the osmotic pressure of the bulk draw solution, C_4 and C_2 are the concentrations of the bulk feed and draw, respectively. The constant K is a measure of the resistance to solute transport in the porous substrate (support layer), given as

$$K = \frac{t\tau}{D_s \varepsilon} \qquad (2.8)$$

Here D_s is the diffusion coefficient of solute in the membrane substrate. The K term introduced by Lee et al. went on to become the metric by which researchers in the field denoted the resistance of their membranes to solute transport until the introduction of the structural parameter term in 2010 by Yip et al. [21].

Extension of Lee et al.'s model to FO by Loeb et al., 1997 [35]

Loeb et al. extended the model developed by Lee et al. to derive transport equations for FO. No assumptions of the original model were changed so this model too did not account for ECP. The equations for K in PRO and FO mode orientations were given as (Equation A2 and A4 in the reference article)

$$PRO\ mode \qquad K = \left(\frac{1}{J_1}\right)\left(\ln\frac{B + A\pi_{Hi} - J_1}{B + A\pi_{Low}}\right) \qquad (2.9)$$

$$FO\ mode \qquad K = \left(\frac{1}{J_1}\right)\left(\ln\frac{B + A\pi_{Hi}}{B + J_1 + A\pi_{Low}}\right) \qquad (2.10)$$

where π_{Hi} is the osmotic pressure of the bulk draw solution and π_{Low} is the osmotic pressure of the bulk feed solution.

Incorporation of ECP in both membrane orientations by McCutcheon et al., 2006 [49]

ECP, a very well-studied phenomenon in RO, was shown to play only a minor role in osmotically driven membrane processes [53] and thus was always ignored while developing transport models. McCutcheon et al. were the first group of researchers to develop a model incorporating the effect of ECP on the selective layer side of the membrane. It was assumed that no ECP occurred on the support side of the membrane since solute was considered to freely permeate this layer. Further, the osmotic reflection coefficient of the membrane was considered to be unity meaning that the membranes were assumed to reject solute to a high degree and exhibit high water fluxes so that reverse solute flux could be considered negligible. This simplified the water flux equations in the PRO and FO mode to (Equations 2.12 and 2.16 in the reference article)

$$\textit{PRO mode} \qquad J_w = A\left[\pi_{D,b}\exp\left(-\frac{J_w}{k}\right) - \pi_{F,b}\exp(J_w K)\right] \tag{2.11}$$

$$\textit{FO mode} \qquad J_w = A\left[\pi_{D,b}\exp(-J_w K) - \pi_{F,b}\exp\left(\frac{J_w}{k}\right)\right] \tag{2.12}$$

Here the subscript *b* refers to the bulk solution and *k* is the mass transfer coefficient in the membrane channel.

Incorporation of ECP and reverse salt flux in a PRO process by Achilli et al., 2009 [54]

Achilli et al. extended the model derived by Lee et al. to incorporate the effects of dilutive ECP on the draw side of the membrane. Their equation for predicting water flux in a PRO process is (Equation 11 in the reference article)

$$J_w = A\left[\pi_{D,b}\exp(-\frac{J_w}{k})\frac{1-\frac{\pi_{F,b}}{\pi_{D,b}}\exp(J_wK)\exp(\frac{J_w}{k})}{1+\frac{B}{J_w}[\exp(J_wK)-1]}-\Delta P\right] \quad (2.13)$$

K was proposed to be calculated from FO experiments (ΔP=0) with DI water as the feed using the following equation (Equation 12 in the reference article)

$$K = \frac{1}{J_w}\ln\left(\frac{A\pi_{D,b}\exp\left(-\frac{J_w}{k}\right)-J_w}{B}+1\right) \quad (2.14)$$

Yip et al. [55] derived a transport model for PRO similar to that of Achilli et al.'s, incorporating reverse solute flux and dilutive ECP, however their equation (Equation 9 in the reference article) is different from that of Eqn. 14 in that it contains the dilutive ECP modulus in the denominator that was found to be missing in Achilli et al.'s model

$$J_w = A\left\{\frac{\pi_{D,b}\exp(-\frac{J_w}{k})-\pi_{F,b}\exp\left(\frac{J_wS}{D}\right)}{1+\frac{B}{J_w}\left[\exp\left(\frac{J_wS}{D}\right)-\exp(-\frac{J_w}{k})\right]}-\Delta P\right\} \quad (2.15)$$

Reverse draw solute permeation in an FO process by Phillip et al., 2010 [56] and Yong et al., 2012 [57]

Phillip et al. derived a transport model describing reverse draw solute permeation in an FO process ignoring ECP effects (DI water feed). Their model is as below (Equation 10 in the reference article)

$$J_s = \frac{J_w c_D}{1 - \left(1 + \frac{J_w}{B}\right)\exp\left(\frac{J_w S}{D}\right)} \qquad (2.16)$$

Here *c* refers to concentration and *S* is the intrinsic structural parameter given by Eqn. 2.1. S was first defined by Yip et al. [21] and nearly replaced the use of K in describing resistance of the membrane to transport. In order to use Eqn. 2.16 to calculate J_s S should be calculated as a fitted parameter from equations for water flux, J_w.

The authors later, in 2012, modified their model above to account for concentrative ECP as shown below (Equation 9 in the reference article)

$$J_s = \frac{J_w B(c_F \exp(Pe^s + Pe^\delta) - c_D)}{(B\exp(Pe^\delta) + J_w)\exp(Pe^s) - B} \qquad (2.17)$$

where the Peclet numbers are $Pe^s = J_w(S/D)$ and $Pe^\delta = J_w/k$.

Modeling reverse draw solute flux incorporating effects of ICP and ECP by Suh et al., 2012 [58]

Suh et al. extended the work by Phillip et al. to develop a model that accounts for ECP on both sides of the membrane. Their equation for reverse solute flux is given as (Equation 18 in the reference article)

$$J_s = B\left(\frac{C_{D,b} + J_{sw}}{\exp\left(J_s \frac{K}{J_{sw}}\right)\exp\left(\frac{J_s}{J_{sw}k_D}\right)} - (C_{F,b} + J_{sw})\exp\left(\frac{J_s}{J_{sw}k_F}\right)\right) \quad (2.18)$$

The term J_{sw} is defined as a constant coefficient equal to J_s/J_w, originally defined by Hancock et al. [59] as the *specific reverse solute flux*, a measure of the water-salt selectivity of the membrane. This quantity is directly related to process efficiency and sustainability and represents the unit loss of draw solute per unit of water flux.

Table 2.1 summarizes these major milestones in development of transport models for FO and PRO, highlighting the key additions and major assumptions of each.

Table 2.1: Timeline of development of major transport models for FO and PRO from 1976-2013.

Reference	FO/PRO	Significant contribution	Key assumptions
Loeb, 1976 [42]	PRO	First transport model developed	J_s=0, no ECP
Lee et al., 1981 [34]	PRO	Included reverse draw solute permeation	No ECP
Loeb et al., 1997 [35]	Both modes$^+$	Extended existing transport model to FO	No ECP
McCutcheon et al., 2006 [49]]	Both modes$^+$	First to include effects of ECP on selective layer side for FO	J_s=0, no ECP on support side
Achilli et al., 2009	PRO	First to include effects of ECP on	No ECP on

[54] Yip et al., 2011 [55]		selective layer side for PRO	support side
Phillip et al., 2010 [56] Yong et al., 2012 [57]	FO	Derived an equation for reverse solute flux	No ECP [56] No ECP on support side [57]
Suh et al., 2012 [58]	FO	Derived an equation for reverse solute flux considering both ECP	*

Note: all models, when necessary, uniformly assume the applicability of van't Hoff's equation for dilute solutions (osmotic pressure is proportional to concentration).

[+]Indicates both FO and PRO modes. PRO *mode* is not the same as the PRO *process*.

* Indicates absence of assumptions similar to that used by other models (such as J_s=0 and no ECP effects)

2.5. Use of pore structure characterization to determine intrinsic structural properties

2.5.1 Imaging characterization techniques

2.5.1.1 Scanning electron microscopy

SEM is the most ubiquitous technique used to characterize soft materials in general and is the most commonly used tool to characterize asymmetric membranes as well. Since the use of SEM in morphological studies of materials is very well known its operating principles are not described here. This technique is invaluable in the sense that it is a relatively simple tool that can be used to study membrane morphology in both top-down and cross-sectional views. The former

is used often to evaluate selective layer properties, to verify its integrity and to qualitatively determine surface roughness. Cross-sectional SEM images are used most often to characterize support pore geometries and sizes and sometimes, at high resolution, to estimate selective layer thickness as well. The former use provides cursory estimates of structural metrics like porosity and to a rougher extent, tortuosity but it should be remembered that SEM is a 2D characterization tool and almost all asymmetric membranes today have complex pore structures with a large degree of anisotropy. This means that 2D views can sometimes be misleading. This was demonstrated in a publication by Manickam et al. [37] where they fractured two TFC RO membranes, BW30 and SW30-XLE from Dow Water and Process Solutions, along orthogonal directions and found that views along the two axes differed significantly from each other. When a membrane, BW30 for instance, was freeze-fractured perpendicular to the direction in which the cast polysulfone membrane was introduced into the precipitation bath, the resulting structure showed the presence of a few oval "macrovoids" indicating modest support layer porosity. However when the exact membrane was freeze-fractured along a direction orthogonal to that of the first sample, the "macrovoids" were seen to be many more in number and also elliptical in shape, stretching nearly throughout the entire support structure. These images are shown here in Fig. 2.3. A single 2D SEM image cannot provide a comprehensive representation of structures anisotropic in 3D. Also, bulk structural metrics like porosity, tortuosity, distribution of porosity etc. cannot be determined from 2D data. Another commonly noted drawback of SEM is the sample preparation involved, with polymeric samples needing to be sputter-coated with a contrast agent due to the lack of natural material contrast. This could lead to some features being masked by particles of the contrast agent, however, this is usually not considered as a deal-breaker since the issue isn't significantly prominent.

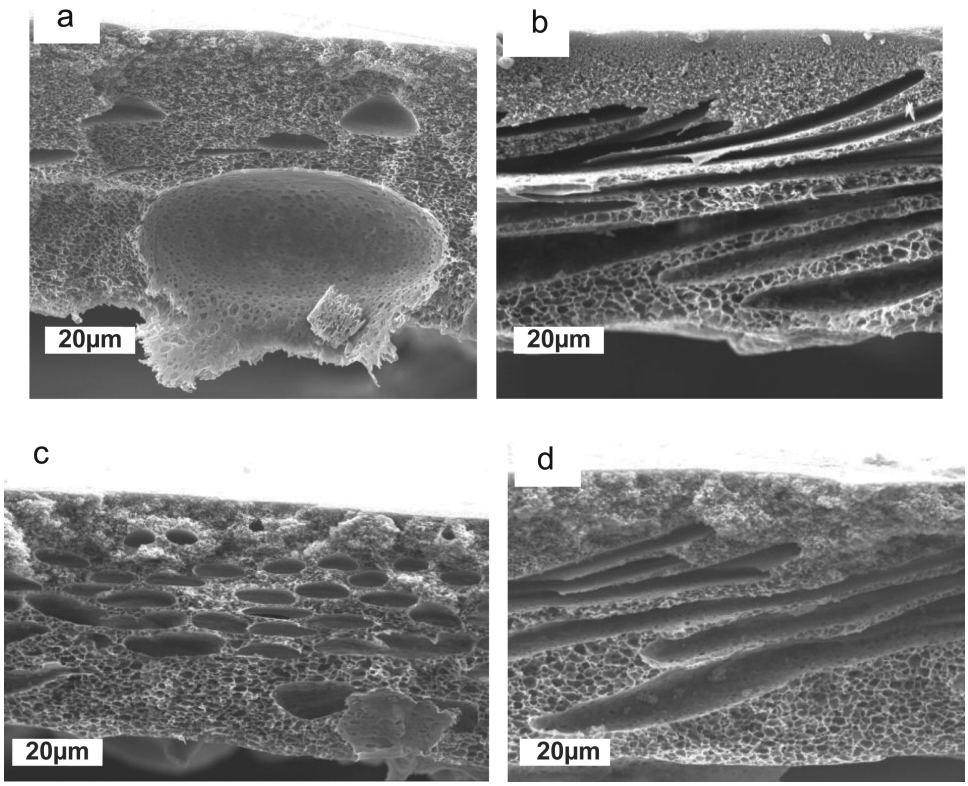

Fig. 2.3. Limitations of SEM in reliably characterizing anisotropic structures – FE-SEM images of the cross-sections of (a and b) BW30 and (c and d) SW30-XLE TFC RO membranes. These samples had been prepared for imaging by freeze-fracturing in liquid nitrogen along two different axial directions. (a and c) Samples freeze-fractured perpendicular to the direction in which the cast polysulfone membrane was introduced into the precipitation bath. (b and d) Samples freeze-fractured in the direction orthogonal to that of a and c. Figure taken from [80].

On the sidelines of SEM characterization, transmission electron microscopy (TEM) is also used to study asymmetric membrane morphology however; the study is usually only limited to the selective layer. One exception is a study by Wang et al. [60] where they extended the use of TEM to measure pore diameters and porosity as a function of sample depth. TEM images, of a cellulose tri-acetate (CTA) membrane from Hydration Technology Innovations (HTI) Scottsdale, Arizona, USA (the membrane is designated as HTI-CTA hereafter), from their study are shown in Fig. 4. In measuring porosity it was found that the TEM data had significantly large error bars and this was attributed to the small sampling volume (i.e., sampling area × sampling thickness (<100 nm for TEM)) thus making the data collected poorly representative of the larger

inhomogeneous volume. This in fact is the principal limitation of imaging techniques, i.e. the samples are typically small and thus not wholly representative of the entire membrane structure. It is also to be noted that TEM is relatively more invasive than SEM thus necessitating additional caution in interpreting the information gathered. In summary, while SEM images are a quick and easy tool to capture membrane surface morphology and to an extent, pore structure, the user should exercise caution in extrapolating that information to the whole membrane.

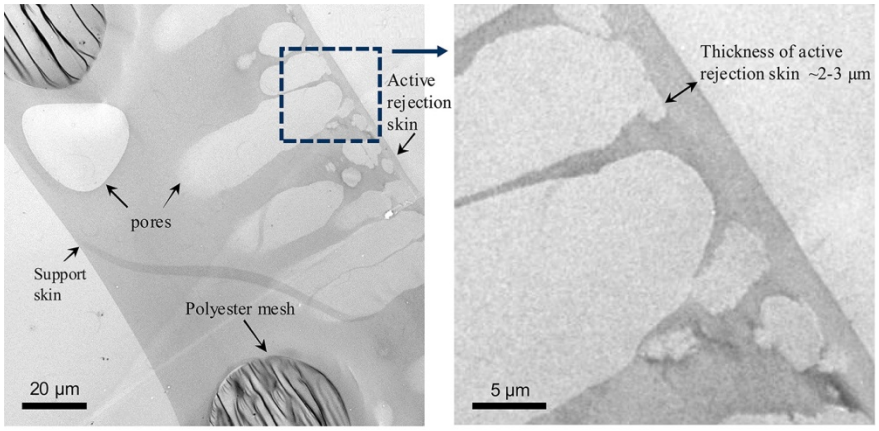

Fig. 2.4. Extension of the use of TEM in imaging asymmetric membranes –cross sections of the HTI-CTA membrane where the entire thickness can be viewed. These images, however, do not resolve the smaller pores in the membrane. Figure taken from [60].

2.5.1.2 Confocal laser scanning microscopy

Confocal laser scanning microscopy (CLSM) is an optics-based technique that can be used to obtain virtual sections of samples. The principle of CLSM was first disclosed in a patent by Marvin Minsky in 1961 [61] but its use gained interest only about two decades after, in the 1980's, with the development of lasers [62]. The technique, an improvement over conventional wide-field fluorescence microscopy, uses an additional pin-hole ahead of its detector optics in order to remove out-of-focus signal coming from the focal plane. In this way, the detector lens and the objective lens "share" the same foci, hence the name confocal. This feature allows the technique to effectively capture information from a single plane at a time and, combining this

with projections from the other focal planes in the sample (the focal planes are usually referred to as z-stacks), allows one to "reconstruct" 3D information. Conchello and Lichtman [63] provide a nice synopsis of the core principles of CLSM and the important variables that adversely affect confocal images. Presently, much of the usage of CLSM is in the life sciences arena with a few reported uses in the semiconductor industry as well. There have been a few publications on using CLSM to characterize MF and UF membranes [64-75] and several more that used the tool to study biofouling on NF and RO membrane surfaces [76]. Biological specimens can be comfortably stained using a variety of dyes and this enables their study using the fluorescence mode on CLSM instruments. In studies on membrane absorbers for viruses and proteins, the cellular organisms were stained with dyes that enabled them to be visualized clearly in the resulting images [66, 67, 69, 70, 72-75]. CLSM is a very useful tool in such studies to study the effect of membrane pore structure on adsorbate retention and migration behaviors and to understand resulting internal polarization phenomena [64, 67, 75]. However, in some of these studies [65] it has been observed that image quality depleted fast beyond scan depths of 10 μm. This indeed, is one of the limitations of CLSM where the capability of depth profiling is limited to small thicknesses. Another obvious disadvantage is the lower resolutions characteristic of optical microscopes. A concern can also arise with the immersion oils that are used to improve resolution at high magnifications since these may affect some polymeric membrane materials [65]. The first disadvantage was nicely addressed in work by Marroquin et al. [68] where they used "cross-sectional views" as opposed to a "top-down view" in order to avoid losing resolution as the laser penetrated deeper into the membrane bulk. They prepared various cross-sectional samples of both isotropic and asymmetric membranes by cryosectioning. A cross-sectional CLSM image of an asymmetric polyethersulfone membrane from their publication, taken at a

cross-sectional depth of 4 µm, is shown in Fig. 2.5. They stained the membrane with 5-DTAF [5-(4,6-dichlorotriazinyl) aminofluorescein] to improve contrast. Their publication also provides a tabular literature review of other work where CLSM was used specifically to characterize membrane structures and can serve as a nice reference.

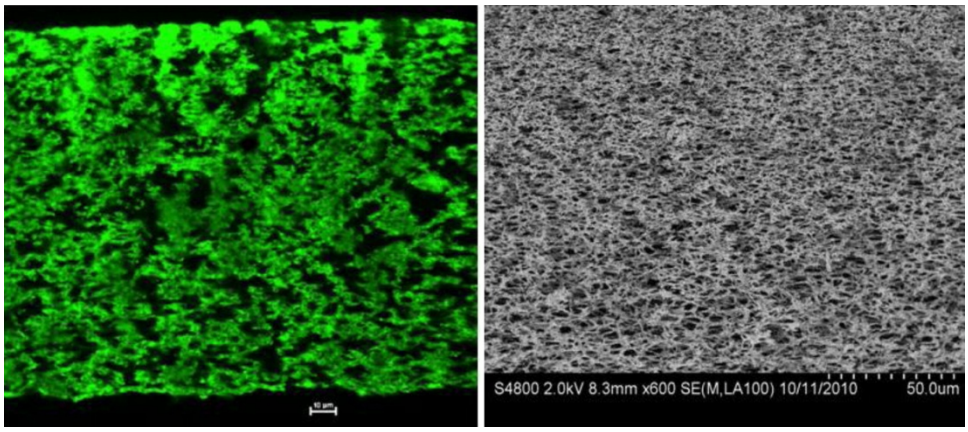

Fig. 2.5. Imaging asymmetric structures with CLSM – cross-sectional CLSM image of an asymmetric MF membrane (a polyethersulfone membrane with an effective pore diameter of 0.65 µm) at a depth of 4 µm (left). The membrane was stained with 5-DTAF (5-(4,6-dichlorotriazinyl) aminofluorescein). The dense surface is at the top. Image scale is 210 µm × 210 µm. Scale bar is 10 µm. A cross-sectional SEM image of this membrane is shown for comparison (right). Figure taken from [68].

The use of CLSM to characterize asymmetric membranes was also demonstrated by Wang et al. [60] where they studied the morphologies of the HTI-CTA membrane and gathered pore diameter and porosity information from image analysis software. The membrane was first dyed with fluorescein isothiocyanate (FITC) to enable visualization in the fluorescent mode and then imaged while wet with ultrapure water. In the CLSM images, the membrane material was seen to be yellow due to the dye and the pores and woven mesh were seen to be grey and black, respectively. Interestingly, the data gathered from imaging the wet membrane was compared to that of the dry membrane (imaged using SEM and TEM). CTA is a moderately hydrophilic polymer that can possibly undergo swelling in the presence of water resulting in different structural characteristics in the hydrated state, a point noted by the authors themselves. The

addition of stains helps to improve the contrast in polymeric materials; however the choice of dyes should be made after careful consideration of any possible interactions or effects on the membrane polymer. Smith and Bryg [77] list the common stains used for polymers in microscopical examination and their paper can serve as a nice reference for those interested in staining membranes prior to imaging with fluorescence. The authors have explored the idea of using CLSM to image membranes in their native, unstained state with some success. We tried to image phase inversion cast supports as well as electrospun supports. In case of the former, a TFC RO membrane from Dow Water and Process Solutions, the SW30-XLE, was imaged using a confocal microscope from Leica Microsystems, the xx. The sample was wet with isopropyl alcohol and immersion oil was used to obtain satisfactory resolutions while imaging using a 100X objective. The recombined z-stacks can be seen in Fig. 6 where voids in the polysulfone (PSu) support layer can be seen. These voids can be correlated to those observed in SEM and XCT images [37]. Overall however, it was observed that the dense polyamide layer in these composite membranes seemed to be impermeable to the laser and thus resolution and contrast were limited in comparison to other techniques.

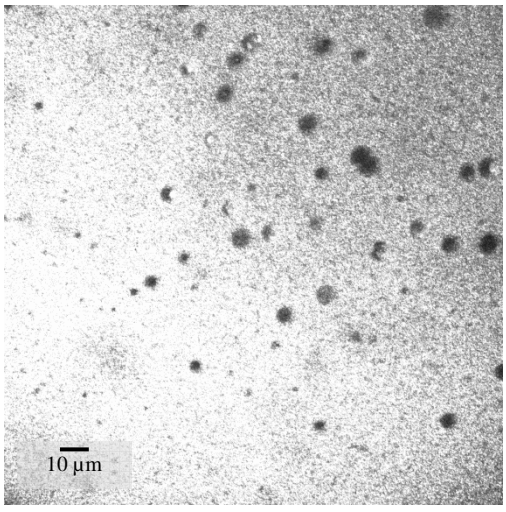

Fig. 2.6. CLSM imaging of asymmetric membranes with top-down penetration – recombined z-stack images of the SW30-XLE TFC RO membrane. The voids in the polysulfone support layer seen here can be correlated to the voids seen in SEM [37] and XCT images (see Fig. 8). The sample was wet with isopropyl alcohol and imaged using a 100X objective.

In the case of the nanofibers, an electrospun mat made from a 9 wt.% polyacrylonitrile (PAN) solution was imaged, again use the 100X objective along with immersion oil. This time, the sample was degassed in a vacuum oven before sealing it in between the glass slide and cover slip. The recombined z-stacks along with a single 2D projection (showing the cross-sections along the x and y directions) can be seen in Fig. 2.7. While the technique was capable of resolving the fine nanofibers it remained that the resolution became poor as the lasers penetrated deeper into the mat. This cannot be avoided since lasers belonging to the visible light spectrum are quite limited in terms of their incident energies and thus for depth profiling and 3D characterization studies higher energy optics, such as those offered by x-rays, would be a better choice.

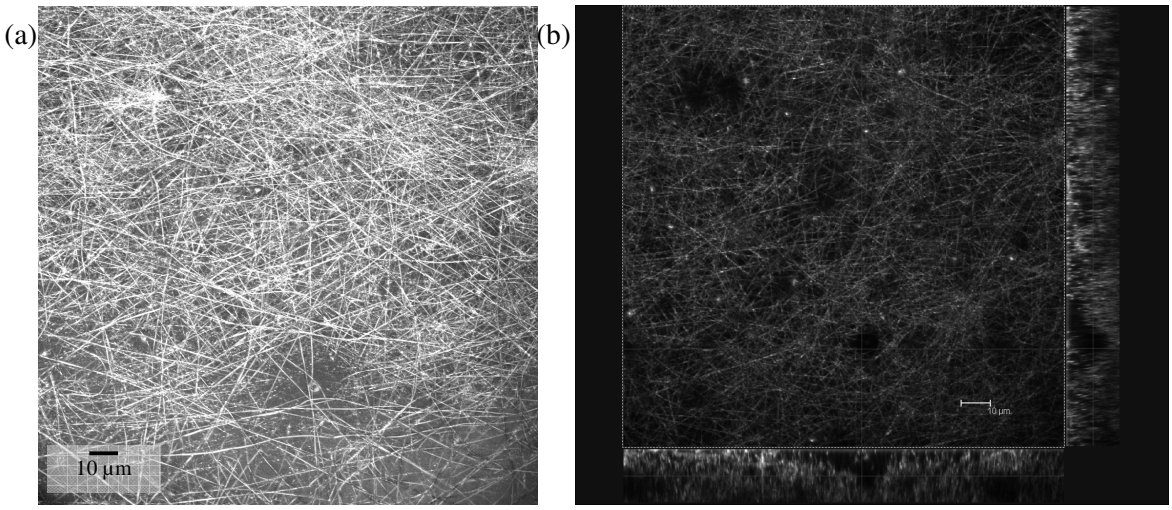

Fig. 2.7. Imaging electrospun nanofibers using CLSM – (a) Recombined z-stack images and (b) a single 2D projection (showing the cross-sections along the x and y directions) of a 9% PAN electrospun nanofibers nonwoven. The sample was imaged using a 100X objective.

2.5.1.3 X-ray computed tomography

X-ray computed tomography (XCT) is a non-destructive technique used for 3D characterization of the internal structure of materials. It is widely used in biomedical imaging and analyses of geological samples but with improved phase contrast optics it has been shown to image low density composite materials and polymers with excellent contrast [78]. The technique uses the penetrating power of high-energy x-rays that lose part of their incident intensity as they penetrate the sample. The loss in intensity is a function of the material's density and atomic composition, given by the linear attenuation coefficient, μ. This behavior is governed by the Beer-Lambert's law given as,

$$I = I_o e^{-\mu x} \qquad (2.19)$$

where I is the intensity of the transmitted x-rays, I_o is the intensity of the incident x-rays and x is the linear position in the sample. 2D XCT projections are collected as the sample is rotated through 180° and a reconstruction algorithm is used to obtain the final 3D volume. Post-processing using image analysis software allows the user to calculate a myriad of structural metrics like pore diameter, porosity, tortuosity, distributions of pore diameters, porosity etc. and pore interconnectivity to name a few. The authors are of the opinion that, pending the collection of high quality images, image analysis software are quite limitless in the amount of valuable information that can be extracted with user knowledge being the only constraint. Figure 8 demonstrates the use of MicroXCT to comprehensively characterize 3D asymmetric structures. The top images show cross-sections of the SW30-XLE TFC RO membrane with the polyester backing layer (lower layer) and polysulfone support layer (upper layer). The thin white horizontal lines indicate top down virtual sectioning of the membrane, shown in the lower images.

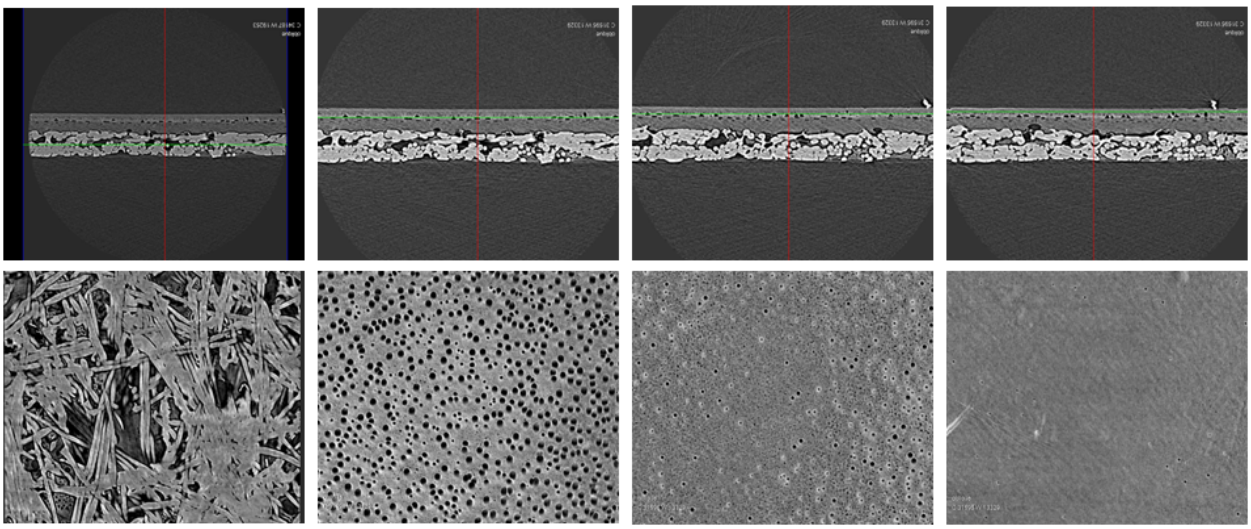

Fig. 2.8. Comprehensive analysis of asymmetric structures using MicroXCT – virtual sectioning of the SW30-XLE TFC RO membrane. Upper images show the membrane cross section with the polyester backing layer (lower layer) and polysulfone support layer (upper layer). The thin white horizontal lines indicate top down virtual sectioning of the membrane, shown in the lower images. Instrument settings: 20X objective, 20kV source, 4.6 hour imaging time, 1 µm pixel resolution. The white bars indicate approximately 200 µm.

XCT being a optics-based method, has limitations in the maximum resolution obtainable although there are two tiers available in commercial XCT instruments, offering different resolutions and fields-of-view (FOV). MicroXCT provides resolutions in the micrometer range whereas nanoXCT can go down to the nano level. Higher resolutions however automatically imply smaller FOVs. Resolution needs in characterization of asymmetric membranes can be subjective with really small pores typically not considered as being significant to transport phenomena. It is possible to "stitch", for instance, two or more nanoXCT (or even microXCT) volumes of high resolution (taken at different positions in the membrane) together to finally construct a large FOV dataset [79], this however, would be a relatively complex operation. An initial study exploring the use of MicroXCT to characterize asymmetric membranes was published by the authors [80] where, for the first time, intrinsic structural parameters of TFC membranes were calculated and compared to the effective S values from experimental flux

measurements. The study published data on the distribution of porosity as a function of membrane thickness and this is a neat tool that is particularly useful in determining the importance of surface porosity on severity of ICP and flux performance. NanoXCT can be used to analyze the support structures in finer detail, as seen in Fig. 2.9 where a section of the polysulfone support layer in the SW30-XLE RO membrane is examined. Fig. 2.9a shows the complete 3D image with the polymer phase (red or light grey in B/W) and pore void phase (blue or dark grey in B/W), 2.9b shows polymer phase only and 2.9c shows image reconstruction of only the pore void phase with a close-up of some of the interconnected pore structure. Such information provides a detailed understanding of pore structure networks and can also perhaps be used to relate structure to membrane fabrication methods. A similar study has been done by Guillen et al. [81] where they used microscopic observations to understand membrane formation by non-solvent induced phase separation. Complementing such studies with the use of 3D characterization will greatly enhance our knowledge of membrane fabrication-structure relationship and will pave the way for developing improved fabrication methods.

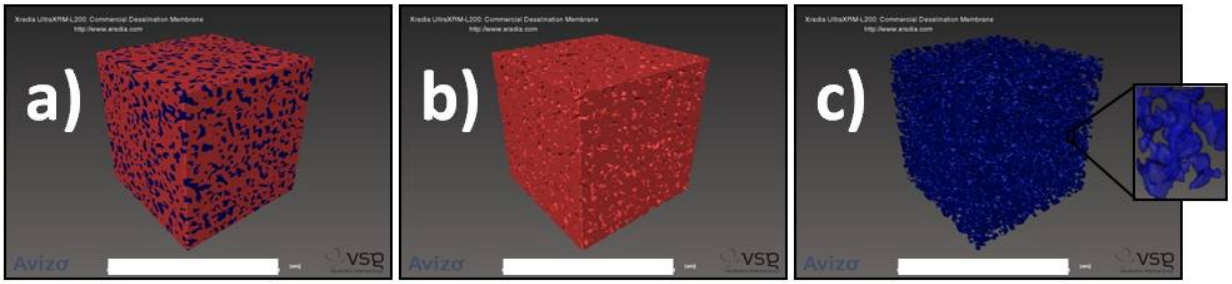

Fig. 2.9. Use of NanoXCT to image microstructures – 3D renderings of the polysulfone support layer in the SW30-XLE TFC RO membrane. Images were reconstructed using the Avizo Fire® software package. a) Complete image including the polymer phase (red or light grey in B/W) and pore void phase (blue or dark grey in B/W); b) image reconstruction of only the polymer phase; c) image reconstruction of only the pore void phase (with a closeup of some of the interconnected pore structure). White bars indicate 20 µm. Pixel resolution is 65 nm.

The main advantages of this technique are that it can provide 3D representations of samples without the need for invasive sample preparations. In fact, sample preparation for XCT

is minimal – the membrane should be cut to the required dimension (ideally, volume of FOV:sample volume should not be greater than 1:10) and simply mounted on the sample stage. Further, in post-processing, image analysis software are capable of yielding a wide gamut of information and the user only needs to seek out the best possible way to extract this information in a reliable manner. Few of the commercially available 3D image analysis software are ImageJ from the National Institutes of Health (NIH), Bethesda, Maryland, USA (available as freeware from the NIH website), Avizo® packages from FEI Company, packages from Media Cybernetics, Inc., Rockville, Maryland, USA. XCT manufacturers also provide their own image analysis tools along with the reconstruction software; however such packages are often limited to simpler analyses. Some of the commercial XCT instrument manufacturers are Carl Zeiss X-ray Microscopy, Pleasanton, California, USA and GE Measurement and Control, USA. Some of the limitations of the technique with respect to asymmetric membrane characterization are the limited resolution of the x-ray optics and the cost associated with both instrument and image analysis software purchases. Data collection time is also sometimes considered a limiting factor with experiment runs ranging from a few hours to overnight depending on the experimental recipe and the number of images needed to be collected. This factor is however a consideration for any 3D imaging technique (for e.g. focused ion beam-SEM) since the data is collected over the entire sample volume, as opposed to from a single surface say, in SEM or TEM.

2.5.2 Analytical characterization techniques

2.5.2.1 Intrusion and extrusion porosimetry

Perhaps the most commonly used analytical tool for 3D characterization of porous materials is porosimetry. Porometry and bubble point measurements are frequently used to

estimate mean and largest pore sizes, respectively [80] but such information are mostly useful only in filter media, microfiltration and ultrafiltration membranes [82]. Porosimetry provides comprehensive pore diameter and pore volume distributions, tortuosities can be calculated from the former with the use of empirical formulae and porosities can be estimated from the latter. It is to be noted that such analytical characterization techniques all assume cylindrical pore geometries in calculating pore diameters. This is a rough approximation that could possibly be severely flawed in case of complex or unusual pore geometries. It is best to assume that the estimates refer to "effective" pore diameters. There are two kinds of porosimetry, intrusion and extrusion porosimetry. Both are governed by similar principles: the pressures needed to either intrude or extrude a test liquid from the pores in the sample are correlated to the respective pore diameters using "wettability" properties of the test liquid (viz. surface tension and contact angle between sample and liquid). The governing equation is

$$d = P\gamma\cos\theta \qquad (2.20)$$

Here d is the pore diameter, P is extrusion (or intrusion) pressure, γ is the surface tension of the test liquid and θ is the contact angle between the sample and test liquid. Eqn. 20 is referred to as the Young-Laplace equation in case of extrusion porosimetry and as the Washburn equation in case of intrusion porosimetry. For the latter a negative sign is added to the right-hand side of the equation to account for θ values greater than 90°. Specifically this is the case in mercury intrusion porosimetry (MIP) which is the traditional approach to porosimetry. Giesche [83] offers a good review on this technique. In MIP, the test liquid used is mercury; first a vacuum is gently applied to the sample tube to remove air present in the pores of the sample following which the differential pressure over the sample tube is incrementally increased causing mercury

to intrude the pores and respective pore diameters are calculated from the intrusion pressures using Eqn. 20. The intruded volume is used to calculate porosity as

$$\%\text{porosity} = \frac{\text{Cumulative volume of test liquid intruded (cc/g)}}{\text{Specific volume of sample (cc/g)}} * 100 \tag{2.21}$$

The specific volume of the sample is best calculated using either gravimetric or sensitive pycnometric measurements. Tortuosities can be calculated using available empirical correlations [84, 85]. Here again, assumptions are made with respect to the "pore shape". MIP has advantages of being an established technique that is well-studied for porous materials characterization. However, on the downside it uses high intrusion pressures that can compress and distort the pore structures of soft materials [37, 80, 83] thus biasing the data. In this way, the technique is semi-destructive and it also uses toxic mercury which can pose a health hazard if not properly handled. MIP is capable of detecting through and blind pores, but not closed pores. Through pores have both an entrance and an exit, blind pores have an entrance but no exit and closed pores have neither. In the context of membranes transporting solutes and solvent, only through pores can contribute meaningfully. During analysis, if pores with hour-glass or ink bottle shape are detected MIP could be biased towards smaller pore sizes if the smaller region of the pore is detected ahead of the larger regions [80, 83]. This is another possible measurement artifact (usually termed as the hysteresis effect) that should be considered while interpreting data. An alternative to the use of toxic, high surface tension mercury is the use of water as the test liquid, though only for hydrophobic samples. This water intrusion porosimetry is the operating principle of the Aquapore made by Porous Materials Inc., Ithaca, NY, USA. The use of this technique in the asymmetric membranes community has not been documented so far.

Another tool available from the same manufacturer is liquid extrusion porosimetry (LEP). In LEP, the sample is completely wetted out using a liquid surfactant and upon application of an external pressure the pores are progressively emptied of the liquid and Eqns. 2.20 and 2.21 are used to calculate pore diameters and bulk porosity, respectively. The surfactant used is non-toxic, unlike mercury, and its low surface tension (approximately 30 times lower than that of mercury) allows for much lower operating pressures and it has been observed that the difference in surface tension exhibits a significant effect on the porosity value obtained [80], effectively circumnavigating compression issues. Also, use of a surfactant as the wetting liquid allows for almost the entire pore volume to be wetted out and hence detected in the analysis; this can be an issue in MIP since mercury tends to intrude pores in the shape of a capillary with a well-defined meniscus at both ends [83]. Also with LEP, smaller pores can be captured using pressures lower than in MIP. The extrusion pressure needed to detect a pore of any given size is about 23 times lower than the corresponding pressure needed for mercury intrusion. There was however a caveat observed with the use of LEP, in a previous publication by the authors, when evaluating nonwovens – the instrument exhibited stabilization issues near the beginning of the experiment rendering the low pressure data unusable. Further, sample preparation is somewhat tedious with ensuring that excess test liquid is drained off before the start of the experiment so that it doesn't cause spikes in the initial measurements. The former is an instrumentation issue that could perhaps be fixed while the latter requires user care and caution. Use of LEP has also not been demonstrated for asymmetric membranes so far; however MIP has been used to characterize electrospun supports [52] as well as phase inversion cast membranes [37, 86]. Arena et al. used porosities and pore diameter distributions obtained from MIP to see if polydopamine

modification of TFC supports blocked off pore spaces [86]. It was interesting to note that the technique could yield the resolution required for such a study.

2.5.2.2 Electrochemical impedance spectroscopy

EIS is a non-invasive method that can be used to analyze the microstructures of materials based on their energy storage and dissipation properties. The electrochemical interaction of ionic solutions with membrane structures is exploited in this technique in order to derive information on structural properties. Interestingly, it was impedance measurements that had provided initial evidence of the idea that living cells were contained by membranes that had low permeability to ions [87-89] and this technique had also been used to gather the first estimates of the thicknesses of cell membranes in the early part of the last century [90]. The use of EIS to resolve structural information in asymmetric membranes is schematically shown in Fig. 2.10 (taken from [91]) where the structural layers in a composite membrane are depicted as equivalent electrical circuits. The skin layer and support layer (sub-layer in the figure) are each represented as a parallel combination of conductance, G and capacitance, C. The layers of electrolyte between the membrane surface and the plane containing the respective electrode, on each side, are represented by conductance elements, G_e^a and G_e^b.

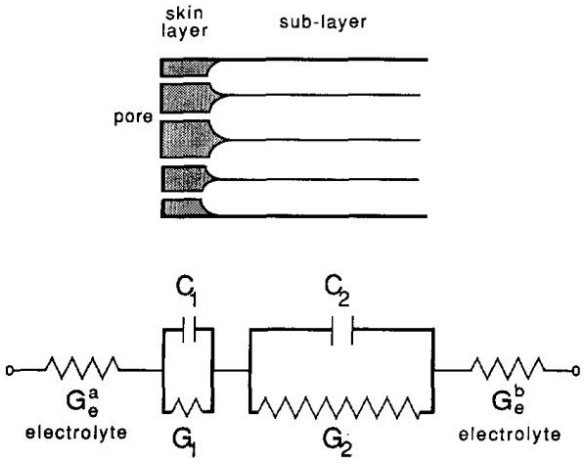

Fig. 2.10. Use of EIS to resolve structural information in asymmetric membranes – depiction of the structural layers in a composite membrane as equivalent electrical circuits. The skin layer and support layer (sub-layer in the figure) are each represented as a parallel combination of conductance, G and capacitance, C. The layers of electrolyte between the membrane surface and the plane containing the respective electrode, on each side, are represented by conductance elements, G_e^a and G_e^b. Figure taken from [91].

EIS works by studying the electrochemical response of the membrane system under a range of alternating current (a.c.) frequencies. At a given frequency, two distinct mechanisms can cause dispersions in the impedance of the membrane [91]. The first is a polarization in ion diffusion in the overall system (membrane + electrolyte) due to differences in the ion transport behaviors between the two media. The second one is a similar phenomenon, except that here it is the difference in ion diffusion between the different layers in a composite membrane (the system here is the interfacial regions in the membrane). This difference arises due to the differences in dielectric and/or conductive properties of the composite layers. The second type of dispersion is commonly referred to as the Maxwell-Wagner dispersion. EIS has been used quite extensively to study membrane structures and particularly, membrane interfacial phenomena and a review by Coster et al. [92] describes these well. Specifically, in asymmetric membranes, this technique has been used to analyze the different layers in composite structures [92-95], determine fouling mechanisms [96-98] and to understand membrane behaviors in aqueous ionic solutions [93, 99, 100]. Apart from these uses, EIS has also been employed in general understanding of membrane micro- and nanostructures [91, 101-103]. It is also, quite obviously, extensively used to study ion-exchange membranes – their structures, fouling mechanisms and behaviors in membrane systems. A general criticism of this tool has been its inability, thus far, to interpret interactions between stationary ion layers and adjacent ions present in a membrane's porous regions. This hinders its ability to distinguish coupled transport effects, say for instance to identify regions of internal and external concentration polarization in an EO membrane [102]. In its present form

EIS can be used to characterize membrane structures and thicknesses but further improvements of the signal to noise ratio at higher ion concentrations and perhaps, improved detection capabilities in EIS systems are needed to advance its use to a higher level [102].

2.5.2.3 Gravimetric analysis of porosity

Arguably the use of gravimetric measurements has been the most popular method of calculating porosity in the community. Several researchers use this simplified approach to obtain rough estimates of porosity [7, 104-117]. Also sometimes referred to as the dry-wet method, it involves measuring the weight of the dry and wet (using either water or iso-propyl alcohol (IPA) as the wetting agent) membrane and using the formula below [117] to calculate porosity as

$$\varepsilon = \frac{(m_{wet} - m_{dry}) / \rho_w}{((m_{wet} - m_{dry}) / \rho_w) + (m_{dry} / \rho_m)} * 100 \qquad (2.22)$$

Here m_{wet} and m_{dry} are the weight of the wet and dry membrane, respectively and ρ_w and ρ_m are the densities of wetting agent and membrane, respectively. Water can be used as the wetting agent for hydrophobic samples and IPA, for hydrophilic samples to avoid swelling issues. Two main challenges exist in the use of this approach. Firstly, for the wet membrane weight measurements to accurately reflect the weight of wetting agent present in pore spaces only care should be taken to ensure that *no* excess liquid is present in the membrane. For this, some researchers blot the excess liquid off using paper wipes; however this is *not* a foolproof method, also there is a possibility that some of the liquid in the pores might also be blotted off in this attempt. The second caveat is that the weight measurements should be sensitive enough to reliably calculate porosity from them. This is especially valid when using this method to compare membranes that are expected to have porosities close to one another or when evaluating

samples with small porosities. In these two cases if adequate care is not taken, the resulting values can be highly erroneous. Perhaps a systematic study of using this method to evaluate a sample, whose porosity is established, and comparing the values could be a good way to "standardize" the method. One suggestion would be to use a track-etched membrane – these membranes have uniform cylindrical pores whose porosity can be easily calculated using simple top-down SEM images [ref, this dissertation]. Since gravimetry is, to a fair extent, influenced by user bias it would be worth the effort to test these standards as a quick validation every time the technique is employed.

For the interested reader, a complete review of the existing and emerging methods used in soft materials characterization is provided by Hutten [82]; those which can be extrapolated to asymmetric membranes have been summarized here. A textbook by Mulder [1] also summarizes traditional approaches of characterizing membranes for gas and liquid separations. Additionally, the reader is also referred to an article on membrane characterization in the Encyclopedia of Membrane Science and Technology by Bernstein et al. [118] for a synopsis on methods for chemical, physical, transport, bulk and surface characterization of membranes.

2.6. Concluding remarks and future directions

2.6.1 Concluding remarks

A review of the approaches for characterizing asymmetric membrane structures, with special focus on EO membranes, has been presented in this article. Numerical models derived from the flux governing equation present a semi-empirical method of quantifying resistance caused by the membrane structure to transport. This is an overarching approach that does not clearly distinguish the resistances caused by the different layers in the composite structure and

thus is best used on a case-by-case basis when comparing membrane performance in a stand-alone study where the only parameter varied is the membrane tested. The benefit of such models is that they effectively include the response of the membrane to test conditions in real time, for example, swelling and de-swelling behaviors in the presence of water and ionic solutions. Changes, if any, to membrane structure and behavior while in its native, working state is captured and thus the true resistance to transport can be estimated. However, the field of engineered osmosis is rapidly evolving and many new membrane platforms are being explored and studied in great detail so as to advance the technology towards commercialization. In the midst of all this activity there exists a need to reliably compare and contrast the different membrane structures developed to see which ones would best benefit this field. Pore structure characterization offers a way of doing this; although work in this area has just begun and is in the process of starting what would hopefully be a long and sustained run. While such techniques do not offer the simplicity associated with the empirical formulae approach, their validity has been convincingly proven, especially in light of the limitations of the latter method. As a summary to this review, two areas of future work, one in each category (numerical models and pore structure characterization) are suggested here.

2.6.2 Future directions

2.6.2.1 Developing improved empirical models for predicting flux behavior

The development of semi-empirical mass transfer models predicting flux behavior has been a constantly evolving field ever since Loeb [42] developed one of the first mathematical models describing transport resistances in a PRO process. Improved understanding of osmotic processes contributed to the development of models encapsulating more parameters with each

new model as described in the timeline shown in Table 2.1. As shown in Fig. 2.1 there are several resistances to transport across the membrane that need to be decoupled from one another in order to improve understanding on how the different layers influence transport behavior and thus to see how they can be best optimized. The structural parameter concept is meant to only describe support layer performance but the models to calculate effective S values also incorporate selective layer properties. In the current methods of fabrication, the formation of the selective layer is indeed influenced by the properties of the support layer as numerous studies have shown and thus these two are inextricably linked. In order to distinguish the effects of the two layers, transport models describing partitioning, sorption and diffusion of water through the selective film are needed. There already exist a few such studies that describe water and solute transport through polyamide and nylon 6,6 films [119-123]; however these are stand-alone studies and their appropriate incorporation into the existing semi-empirical models is needed in order to paint a meaningful picture. It would also be beneficial if the models developed can shed light on transport at the selective-support layer interface and how this is influenced by support porosity as this is a key aspect in osmotic membrane processes.

A significant drawback of the fitted-parameter approach is the assumption of van't Hoff behavior for dilute solutions. This point is debatable especially when high draw solution concentrations are used or there exists improved mixing as a result of high cross-flow velocities. The latter is important in light of the recent observation by Bui et al. where the severity of ICP were found to decrease with increased cross-flow velocity due to the change of slip conditions at the porous surface [52]. The incorporation of a non-ideal solution assumption would be complex but a worthwhile effort, it is expected.

Another uphill task awaiting model developers and users is making models tunable so that they can be used with a number of different draw solutions. Draw solution design is an active research area in the EO community and a number of novel draw solutes are being developed, as outlined in the introduction. Since the empirical method calculates S values as a function of membrane testing conditions it is necessary to account for changes in draw solution properties as well.

2.6.2.2 Improvements to pore structure characterization of asymmetric membranes

As mentioned previously, structural characterization of asymmetric membranes using analytical and imaging techniques is a budding field waiting to prove its utility. A lot of work can be done with respect to both improving on the current techniques to "standardize" them as well as developing newer approaches that are simple and feasible. The principal advantage of the empirical model approach, other than their simplicity, is that the data reflects membrane transport behavior in real time – when the membrane is in its native, working state. This is also one of the biggest challenges for characterization techniques – to ensure that the method can represent the membrane in its native state as best as possible. Since these membranes are all used in the presence of water, characterizing them in their hydrated state reflects a more "real" picture. This can be done using both analytical and imaging tools. For analytical measurements, a suggestion would be to use water intrusion porosimetry, detailed previously in Section 2.5.2.1. Three imaging choices are available: environmental SEM (ESEM), CLSM and XCT. Some initial work by the authors' revealed that the use of ESEM in imaging hydrated membranes is limited by low signal-to-noise ratio and hence, poor contrast in the images. Unlike conventional SEM (which operates in a vacuum), ESEM needs to be operated in a low pressure atmosphere in order to prevent the water used for hydration from freezing. This tends to cause scattering of the

electron beam, thus reducing the signal-to-noise ratio in the images. For three-phase (air-water-polymer) image analysis obtaining good contrasts is extremely important, otherwise the entire exercise can be rendered meaningless. CLSM being optics-based offers limited resolution and it is yet to be explored if contrasts required for a three-phase study can be obtained. In the study by Wang et al. [60] the HTI-CTA membrane was first dyed with fluorescein isothiocyanate (FITC) to enable visualization in the fluorescent mode and then imaged while wet with ultrapure water. In the CLSM images, the membrane material was seen to be yellow due to the dye and the pores and woven mesh were seen to be grey and black, respectively. It was not distinguished if the pores were filled with air or water. It thus remains to be seen if such a study is possible using this technique.

2.6.2.2.1 Imaging hydrated membranes using MicroXCT

The authors have performed some initial studies on using XCT which is the third option available to image hydrated membranes. This too, is a challenging task with the contrast obtained being pretty poor and sample handling and mounting being factors that need to be aptly manipulated. A suggested method of sample mounting is to place the membrane vertically in a polyimide (this polymer is nearly transparent to x-rays) tube taking care to ensure that the sample stays as flat as possible thus avoiding shifts in the center of the FOV during imaging. The tube can then be filled with water and capped off at both ends. The tube needs to be of sufficiently small dimensions so that excess water does not cause undesirable x-ray attenuation. As mentioned earlier, volume of FOV:sample volume should ideally be not greater than 1:10. It is also possible to mount the sample horizontally to avoid excessive x-ray attenuation. Most importantly, x-ray parameters (source power and voltage) and exposure times (to obtain 2D projections) need to be optimized to obtain images with low noise and optimal pixel counts,

respectively. Initial studies were performed with a hydrated nylon 6,6 microfiltration membrane from 3M®, the BLA080, which is an asymmetric membrane consisting of three zones: an upstream large-pores region (average pore size of 2.5 μm), a nonwoven reinforcement layer and a downstream small-pores region (average pore size of 0.8 μm) [3M spec sheets]. This membrane platform has been previously evaluated as an FO membrane support by Huang et al. [16] and was an apt choice for our study since nylon 6,6 is hydrophilic and should wet out reasonably well in the presence of water. The results are shown in Fig. 2.11, the image on the left is that of the dry membrane showing the three zones and on the right is a screenshot of the segmented image where the presence of the three phases can be seen. The image analysis was performed using Avizo®Fire (specifically, the filtered images were analyzed using the 2DHistogram Segmentation module). The orange pixels correspond to the water phase, light blue pixels indicate air and dark blue indicates polymer matrix. The water was seen to permeate deeper into the large pores region, clearly as a result of more favorable capillary interactions and ease of accessibility and it is barely seen in the small pores zone. While these initial results are encouraging a lot more effort is needed in order to standardize this technique and ensure reproducibility. The success of this technique will open up new avenues for enabling study of swelling behaviors of hydrophilic polymers and wettability of moderately-hydrophobic and hydrophobic membrane supports.

(a)

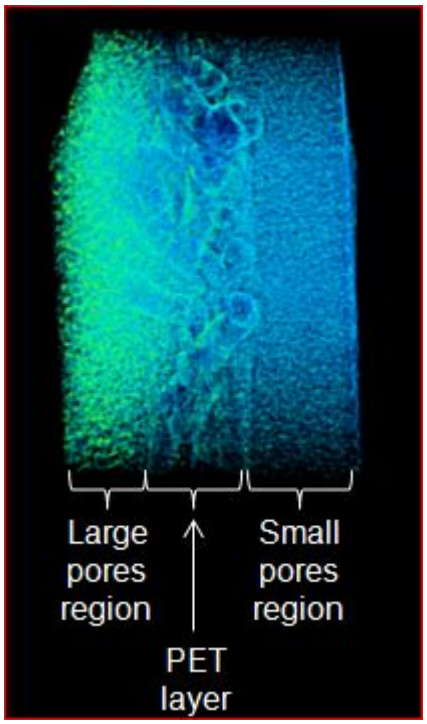
Large
pores
region
Small
pores
region
PET
layer

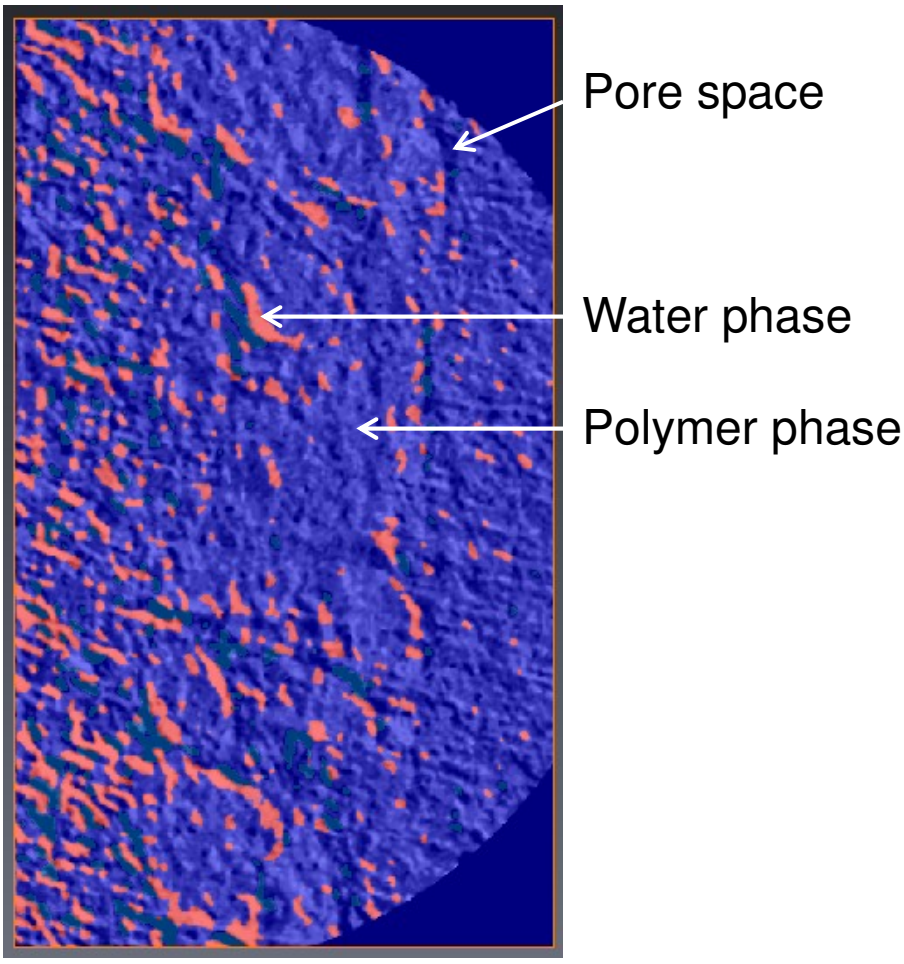
Pore space
Water phase
Polymer phase

Fig. 2.11. Imaging hydrated membranes with XCT – (a) Screenshot of the 3D view of BLA080, an MF membrane from 3M®, in the dry state. The membrane consists of three zones as indicated by the labels. (b) 2D screenshot of the segmentation analysis showing the results of a three-phase (air-water-polymer) study on the hydrated BLA080 membrane. The image analysis was performed using Avizo®Fire (specifically, the filtered images were analyzed using the 2DHistogram Segmentation module). The orange pixels correspond to the water phase, light blue pixels indicate air and dark blue indicates polymer (nylon/PET) matrix.

References

1. Mulder, M., *Basic Principles of Membrane Technology*. Second ed. 1996, Norwell, MA, USA: Kluwer Academic Publishers.

2. Lonsdale, H.K., U. Merten, and R.L. Riley, *Transport properties of cellulose acetate osmotic membranes.* Journal of Applied Polymer Science, 1965. **9**(4): p. 1341-1362.
3. Merten, U., *Desalination by Reverse Osmosis*. 1966, Cambridge: The M.I.T Press.
4. Liu, X., S. Qi, Y. Li, L. Yang, B. Cao, and C.Y. Tang, *Synthesis and characterization of novel antibacterial silver nanocomposite nanofiltration and forward osmosis membranes based on layer-by-layer assembly.* Water research, 2013. **47**(9): p. 3081-3092.
5. Qi, S., W. Li, Y. Zhao, N. Ma, J. Wei, T.W. Chin, and C.Y. Tang, *Influence of the properties of layer-by-layer active layers on forward osmosis performance.* Journal of Membrane Science, 2012. **423**: p. 536-542.
6. Qi, S., C.Q. Qiu, Y. Zhao, and C.Y. Tang, *Double-skinned forward osmosis membranes based on layer-by-layer assembly - FO performance and fouling behavior.* Journal of Membrane Science, 2012. **405**: p. 20-29.
7. Qiu, C., S. Qi, and C.Y. Tang, *Synthesis of high flux forward osmosis membranes by chemically crosslinked layer-by-layer polyelectrolytes.* Journal of Membrane Science, 2011. **381**(1): p. 74-80.
8. Ghosh, A.K. and E. Hoek, *Impacts of support membrane structure and chemistry on polyamide-polysulfone interfacial composite membranes.* Journal of Membrane Science, 2009. **336**(1): p. 140-148.
9. Petersen, R.J., *Composite reverse osmosis and nanofiltration membranes.* Journal of Membrane Science, 1993. **83**(1): p. 81-150.
10. Ramon, G.Z., M.C.Y. Wong, and E. Hoek, *Transport through composite membrane, part 1: Is there an optimal support membrane?* Journal of Membrane Science. **415**: p. 298-305.
11. Lonsdale, H.K., R.L. Riley, C.R. Lyons, and D.P. Carosella Jr, *Transport in composite reverse osmosis membranes*, in *Membrane Processes in Industry and Biomedicine*. 1971, Springer. p. 101-122.
12. Lee, K.P., T.C. Arnot, and D. Mattia, *A review of reverse osmosis membrane materials for desalination - development to date and future potential.* Journal of Membrane Science, 2011. **370**(1): p. 1-22.
13. Arena, J.T., B. McCloskey, B.D. Freeman, and J.R. McCutcheon, *Surface modification of thin film composite membrane support layers with polydopamine: enabling use of reverse osmosis membranes in pressure retarded osmosis.* Journal of Membrane Science, 2011. **375**(1): p. 55-62.
14. Bui, N.-N., M.L. Lind, E. Hoek, and J.R. McCutcheon, *Electrospun nanofiber supported thin film composite membranes for engineered osmosis.* Journal of Membrane Science, 2011. **385**: p. 10-19.

15. Bui, N.-N. and J.R. McCutcheon, *Hydrophilic nanofibers as new supports for thin film composite membranes for engineered osmosis.* Environmental science & technology, 2013. **47**(3): p. 1761-1769.
16. Huang, L., N.-N. Bui, M.T. Meyering, T.J. Hamlin, and J.R. McCutcheon, *Novel hydrophilic nylon 6, 6 microfiltration membrane supported thin film composite membranes for engineered osmosis.* Journal of Membrane Science, 2013. **437**: p. 141-149.
17. Song, X., Z. Liu, and D.D. Sun, *Energy recovery from concentrated seawater brine by thin-film nanofiber composite pressure retarded osmosis membranes with high power density.* Energy & Environmental Science, 2013. **6**(4): p. 1199-1210.
18. Tiraferri, A., N.Y. Yip, W.A. Phillip, J.D. Schiffman, and M. Elimelech, *Relating performance of thin-film composite forward osmosis membranes to support layer formation and structure.* Journal of Membrane Science, 2011. **367**(1): p. 340-352.
19. Wang, R., L. Shi, C.Y. Tang, S. Chou, C. Qiu, and A.G. Fane, *Characterization of novel forward osmosis hollow fiber membranes.* Journal of Membrane Science, 2010. **355**(1): p. 158-167.
20. Widjojo, N., T.-S. Chung, M. Weber, C. Maletzko, and V. Warzelhan, *The role of sulphonated polymer and macrovoid-free structure in the support layer for thin-film composite (TFC) forward osmosis (FO) membranes.* Journal of Membrane Science, 2011. **383**(1): p. 214-223.
21. Yip, N.Y., A. Tiraferri, W.A. Phillip, J.D. Schiffman, and M. Elimelech, *High performance thin-film composite forward osmosis membrane.* Environmental science & technology, 2010. **44**(10): p. 3812-3818.
22. Achilli, A., T.Y. Cath, and A.E. Childress, *Selection of inorganic-based draw solutions for forward osmosis applications.* Journal of Membrane Science, 2010. **364**(1): p. 233-241.
23. Ge, Q., J. Su, G.L. Amy, and T.-S. Chung, *Exploration of polyelectrolytes as draw solutes in forward osmosis processes.* Water research, 2012. **46**(4): p. 1318-1326.
24. Ling, M.M. and T.-S. Chung, *Desalination process using super hydrophilic nanoparticles via forward osmosis integrated with ultrafiltration regeneration.* Desalination, 2011. **278**(1): p. 194-202.
25. Stone, M.L., C. Rae, F.F. Stewart, and A.D. Wilson, *Switchable polarity solvents as draw solutes for forward osmosis.* Desalination, 2013. **312**: p. 124-129.
26. Stone, M.L., A.D. Wilson, M.K. Harrup, and F.F. Stewart, *An initial study of hexavalent phosphazene salts as draw solutes in forward osmosis.* Desalination, 2013. **312**: p. 130-136.
27. Beaudry, E.G. and J.R. Herron. *Direct osmosis for concentrating wastewater*. in *Proceedings of the 27th International Conference on Environmental Systems*. 1997. Lake Tahoe, NV: SAE Technical Paper.
28. Cath, T.Y., S. Gormly, E.G. Beaudry, M.T. Flynn, V.D. Adams, and A.E. Childress, *Membrane contactor processes for wastewater reclamation in space: Part I. Direct osmotic concentration as pretreatment for reverse osmosis.* Journal of Membrane Science, 2005. **257**(1): p. 85-98.
29. Sagiv, A. and R. Semiat, *Backwash of RO spiral wound membranes.* Desalination, 2005. **179**(1): p. 1-9.
30. York, R.J., R.S. Thiel, and E.G. Beaudry. *Full-scale experience of direct osmosis concentration applied to leachate management*. in *Proceedings of the Seventh International Waste Management and Landfill Symposium (Sardinia '99), S. Margherita di Pula, Cagliari, Sardinia, Italy*. 1999.
31. Loeb, S. and S. Sourirajan, *Advances in Chemistry Series No. 38.* Saline Water Conversion IIAmerican Chemical Society, Washington, DC, 1963: p. 117.
32. Mehta, G.D. and S. Loeb, *Performance of Permasep B-9 and B-10 membranes in various osmotic regions and at high osmotic pressures.* Journal of Membrane Science, 1979. **4**: p. 335-349.

33. Wong, M.C.Y., K. Martinez, G.Z. Ramon, and E. Hoek, *Impacts of operating conditions and solution chemistry on osmotic membrane structure and performance.* Desalination, 2012. **287**: p. 340-349.
34. Lee, K.L., R.W. Baker, and H.K. Lonsdale, *Membranes for power generation by pressure-retarded osmosis.* Journal of Membrane Science, 1981. **8**(2): p. 141-171.
35. Loeb, S., L. Titelman, E. Korngold, and J. Freiman, *Effect of porous support fabric on osmosis through a Loeb-Sourirajan type asymmetric membrane.* Journal of Membrane Science, 1997. **129**(2): p. 243-249.
36. Mehta, G.D. and S. Loeb, *Internal polarization in the porous substructure of a semipermeable membrane under pressure-retarded osmosis.* Journal of Membrane Science, 1979. **4**: p. 261-265.
37. Manickam, S.S., J. Gelb, and J.R. McCutcheon, *Pore structure characterization of asymmetric membranes: Non-destructive characterization of porosity and tortuosity.* Journal of Membrane Science, 2014. **454**: p. 549-554.
38. Cath, T.Y., A.E. Childress, and M. Elimelech, *Forward osmosis: principles, applications, and recent developments.* Journal of Membrane Science, 2006. **281**(1): p. 70-87.
39. Hildebrand, J.H., *Osmotic pressure.* Science, 1955. **121**(3135): p. 116-119.
40. Lewis, G.N., *THE OSMOTIC PRESSURE OF CONCENTRATED SOLUTIONS, AND THE LAWS OF THE PERFECT SOLUTION.* Journal of the American Chemical Society, 1908. **30**(5): p. 668-683.
41. Park, M., J.J. Lee, S. Lee, and J.H. Kim, *Determination of a constant membrane structure parameter in forward osmosis processes.* Journal of Membrane Science, 2011. **375**(1): p. 241-248.
42. Loeb, S., *Production of energy from concentrated brines by pressure-retarded osmosis: I. Preliminary technical and economic correlations.* Journal of Membrane Science, 1976. **1**: p. 49-63.
43. Coday, B.D., D.M. Heil, P. Xu, and T.Y. Cath, *Effects of transmembrane hydraulic pressure on performance of forward osmosis membranes.* Environmental science & technology, 2013. **47**(5): p. 2386-2393.
44. Loeb, S., F. Van Hessen, and D. Shahaf, *Production of energy from concentrated brines by pressure-retarded osmosis: II. Experimental results and projected energy costs.* Journal of Membrane Science, 1976. **1**: p. 249-269.
45. Tiraferri, A., N. Yin Yip, A.P. Straub, S. Romero-Vargas Castrillon, and M. Elimelech, *A Method for the Simultaneous Determination of Transport and Structural Parameters of Forward Osmosis Membranes.* Journal of Membrane Science, 2013. **444**: p. 523-538.
46. Huang, L. and J.R. McCutcheon, *Hydrophilic nylon 6, 6 nanofibers supported thin film composite membranes for engineered osmosis.* Journal of Membrane Science, 2014. **457**: p. 162-169.
47. Cath, T.Y., M. Elimelech, J.R. McCutcheon, R.L. McGinnis, A. Achilli, D. Anastasio, A.R. Brady, A.E. Childress, I.V. Farr, and N.T. Hancock, *Standard methodology for evaluating membrane performance in osmotically driven membrane processes.* Desalination, 2012. **312**: p. 31-38.
48. Gray, G.T., J.R. McCutcheon, and M. Elimelech, *Internal concentration polarization in forward osmosis: role of membrane orientation.* Desalination, 2006. **197**(1): p. 1-8.
49. McCutcheon, J.R. and M. Elimelech, *Influence of concentrative and dilutive internal concentration polarization on flux behavior in forward osmosis.* Journal of Membrane Science, 2006. **284**(1): p. 237-247.
50. Shi, L., S.R. Chou, R. Wang, W.X. Fang, C.Y. Tang, and A.G. Fane, *Effect of substrate structure on the performance of thin-film composite forward osmosis hollow fiber membranes.* Journal of Membrane Science, 2011. **382**(1): p. 116-123.
51. Singh, P.S., S.V. Joshi, J.J. Trivedi, C.V. Devmurari, A.P. Rao, and P.K. Ghosh, *Probing the structural variations of thin film composite RO membranes obtained by coating polyamide over*

polysulfone membranes of different pore dimensions. Journal of Membrane Science, 2006. **278**(1): p. 19-25.
52. Bui, N.-N., *Engineered Osmosis for Sustainable Water and Energy: Novel Nanofiber-supported Thin-film Composite Membrane Design & Updated Flux Model Proposal*. 2013, University of Connecticut: Storrs.
53. McCutcheon, J.R., R.L. McGinnis, and M. Elimelech, *Desalination by ammonia-carbon dioxide forward osmosis: influence of draw and feed solution concentrations on process performance.* Journal of Membrane Science, 2006. **278**(1): p. 114-123.
54. Achilli, A., T.Y. Cath, and A.E. Childress, *Power generation with pressure retarded osmosis: An experimental and theoretical investigation.* Journal of Membrane Science, 2009. **343**(1): p. 42-52.
55. Yip, N.Y., A. Tiraferri, W.A. Phillip, J.D. Schiffman, L.A. Hoover, Y.C. Kim, and M. Elimelech, *Thin-film composite pressure retarded osmosis membranes for sustainable power generation from salinity gradients.* Environmental science & technology, 2011. **45**(10): p. 4360-4369.
56. Phillip, W.A., J.S. Yong, and M. Elimelech, *Reverse draw solute permeation in forward osmosis: modeling and experiments.* Environmental science & technology, 2010. **44**(13): p. 5170-5176.
57. Yong, J.S., W.A. Phillip, and M. Elimelech, *Coupled reverse draw solute permeation and water flux in forward osmosis with neutral draw solutes.* Journal of Membrane Science, 2012. **392**: p. 9-17.
58. Suh, C. and S. Lee, *Modeling reverse draw solute flux in forward osmosis with external concentration polarization in both sides of the draw and feed solution.* Journal of Membrane Science, 2012. **427**: p. 365-374.
59. Hancock, N.T. and T.Y. Cath, *Solute coupled diffusion in osmotically driven membrane processes.* Environmental science & technology, 2009. **43**(17): p. 6769-6775.
60. Wang, Y.-N., J. Wei, Q. She, F. Pacheco, and C.Y. Tang, *Microscopic characterization of FO/PRO membranes - a comparative study of CLSM, TEM and SEM.* Environmental science & technology, 2012. **46**(18): p. 9995-10003.
61. Minsky, M., *Microscopy apparatus*. 1961.
62. *Handbook of Biological Confocal Microscopy*. Third ed, ed. P. JB. 2006, Berlin: Springer.
63. Conchello, J.-A. and J.W. Lichtman, *Optical sectioning microscopy.* Nature methods, 2005. **2**(12): p. 920-931.
64. Bakhshayeshi, M., N. Jackson, R. Kuriyel, A. Mehta, R. van Reis, and A.L. Zydney, *Use of confocal scanning laser microscopy to study virus retention during virus filtration.* Journal of Membrane Science, 2011. **379**(1): p. 260-267.
65. Charcosset, C. and J.-C. Bernengo, *Comparison of microporous membrane morphologies using confocal scanning laser microscopy.* Journal of Membrane Science, 2000. **168**(1): p. 53-62.
66. Chenette, H., J.R. Robinson, E. Hobley, and S.M. Husson, *Development of high-productivity, strong cation-exchange adsorbers for protein capture by graft polymerization from membranes with different pore sizes.* Journal of Membrane Science, 2012. **423**: p. 43-52.
67. Jackson, N.B., M. Bakhshayeshi, A.L. Zydney, A. Mehta, R. Reis, and R. Kuriyel, *Internal virus polarization model for virus retention by the Ultipor® VF Grade DV20 membrane.* Biotechnology progress, 2014. **30**(4): p. 856-863.
68. Marroquin, M., T. Bruce, J. Pellegrino, S.R. Wickramasinghe, and S.M. Husson, *Characterization of asymmetry in microporous membranes by cross-sectional confocal laser scanning microscopy.* Journal of Membrane Science, 2011. **379**(1): p. 504-515.
69. Marroquin, M., A. Vu, T. Bruce, R. Powell, S.R. Wickramasinghe, and S.M. Husson, *Location and quantification of biological foulants in a wet membrane structure by cross-sectional confocal laser scanning microscopy.* Journal of Membrane Science, 2014. **453**: p. 282-291.

70. Marroquin, M., A. Vu, T. Bruce, S. Ranil Wickramasinghe, L. Zhao, and S.M. Husson, *Evaluation of fouling mechanisms in asymmetric microfiltration membranes using advanced imaging.* Journal of Membrane Science, 2014. **465**: p. 1-13.
71. Singh, N., J. Wang, M. Ulbricht, S.R. Wickramasinghe, and S.M. Husson, *Surface-initiated atom transfer radical polymerization: a new method for preparation of polymeric membrane adsorbers.* Journal of Membrane Science, 2008. **309**(1): p. 64-72.
72. Wandera, D., H.H. Himstedt, M. Marroquin, S.R. Wickramasinghe, and S.M. Husson, *Modification of ultrafiltration membranes with block copolymer nanolayers for produced water treatment: The roles of polymer chain density and polymerization time on performance.* Journal of Membrane Science, 2012. **403**: p. 250-260.
73. Wang, J., F. Dismer, J.r. Hubbuch, and M. Ulbricht, *Detailed analysis of membrane adsorber pore structure and protein binding by advanced microscopy.* Journal of Membrane Science, 2008. **320**(1): p. 456-467.
74. Wickramasinghe, S.R., J.O. Carlson, C. Teske, J. Hubbuch, and M. Ulbricht, *Characterizing solute binding to macroporous ion exchange membrane adsorbers using confocal laser scanning microscopy.* Journal of Membrane Science, 2006. **281**(1): p. 609-618.
75. Woods, M.A. and A.L. Zydney, *Effects of a pressure release on virus retention with the Ultipor DV20 membrane.* Biotechnology and bioengineering, 2014. **111**(3): p. 545-551.
76. Herzberg, M. and M. Elimelech, *Biofouling of reverse osmosis membranes: role of biofilm-enhanced osmotic pressure.* Journal of Membrane Science, 2007. **295**(1): p. 11-20.
77. Smith, R.W. and V. Bryg, *Staining polymers for microscopical examination.* Rubber chemistry and technology, 2006. **79**(3): p. 520-540.
78. S.H. Lau, W.K.S.C.F.G., Hauyee Chang, Andrei, M.F. Tkachuk, Wenbing Yun, *Non invasive, multiscale 3D X-Ray characterization of porous functional composites and membranes, with resolution from mm to sub 50 nm.* Journal of Physics: Conference Series, 2009. **152**(1): p. 012059.
79. www.xradia.com. [cited.
80. S Manickam, S. and J.R. McCutcheon, *Characterization of polymeric nonwovens using porosimetry, porometry and X-ray computed tomography.* Journal of Membrane Science, 2012. **407**: p. 108-115.
81. Guillen, G.R., G.Z. Ramon, H.P. Kavehpour, R.B. Kaner, and E. Hoek, *Direct microscopic observation of membrane formation by nonsolvent induced phase separation.* Journal of Membrane Science, 2013. **431**: p. 212-220.
82. Hutten, I.M., *Handbook of Non-Woven Filter Media*. First ed. 2007: Butterworth-Heinemann.
83. Giesche, H., *Mercury porosimetry: a general (practical) overview.* Particle & particle systems characterization, 2006. **23**(1): p. 9-19.
84. Carniglia, S.C., *Construction of the tortuosity factor from porosimetry.* Journal of Catalysis, 1986. **102**(2): p. 401-418.
85. Micromeritics, *AutoPore Manual*. 2013.
86. Arena, J.T., S.S. Manickam, K.K. Reimund, B.D. Freeman, and J.R. McCutcheon, *Solute and water transport in forward osmosis using polydopamine modified thin film composite membranes.* Desalination, 2014. **343**: p. 8-16.
87. Bernstein, J., *Uber den zeitlichen Verlauf der negativen Schwankung des Nervenstroms.* Arch. Ges. Physiol., 1868. **1**: p. 173-207.
88. Höber, R., *Eine Methode, die elektrische Leitfahigkeit im Innern von Zellen zu messen.* Arch. Ges. Physiol., 1910. **133**: p. 237-259.

89. Overton, E., *Ueber die allgemeinen osmotischen Eigenschaften der Zelle, ihre vermutlichen Ursachen und ihre Bedeutung fur die Physiologie.* Vjschr. Naturf. Ges. Zurich, 1899. **44**: p. 88-113.
90. Fricke, H. and S. Morse, *The electric resistance and capacity of blood for frequencies between 800 and 4½ million cycles.* The Journal of general physiology, 1925. **9**(2): p. 153.
91. Coster, H.G.L., K.J. Kim, K. Dahlan, J.R. Smith, and C.J.D. Fell, *Characterisation of ultrafiltration membranes by impedance spectroscopy. I. Determination of the separate electrical parameters and porosity of the skin and sublayers.* Journal of Membrane Science, 1992. **66**(1): p. 19-26.
92. Coster, H.G.L., T.C. Chilcott, and A.C.F. Coster, *Impedance spectroscopy of interfaces, membranes and ultrastructures.* Bioelectrochemistry and Bioenergetics, 1996. **40**(2): p. 79-98.
93. Asaka, K., *Dielectric properties of cellulose acetate reverse osmosis membranes in aqueous salt solutions.* Journal of Membrane Science, 1990. **50**(1): p. 71-84.
94. Benavente, J., *Electrochemical impedance spectroscopy as a tool for electrical and structural characterizations of membranes in contact with electrolyte solutions*, in *Recent Advances in Multidisciplinary Applied Physics*. 2005. p. 463-471.
95. Cañas, A., M.J. Ariza, and J. Benavente, *Characterization of active and porous sublayers of a composite reverse osmosis membrane by impedance spectroscopy, streaming and membrane potentials, salt diffusion and X-ray photoelectron spectroscopy measurements.* Journal of Membrane Science, 2001. **183**(1): p. 135-146.
96. Cen, J., J. Kavanagh, H. Coster, and G. Barton, *Fouling of reverse osmosis membranes by cane molasses fermentation wastewater: detection by electrical impedance spectroscopy techniques.* Desalination and Water Treatment, 2013. **51**(4-6): p. 969-975.
97. De Lara, R. and J. Benavente, *Use of hydrodynamic and electrical measurements to determine protein fouling mechanisms for microfiltration membranes with different structures and materials.* Separation and Purification Technology, 2009. **66**(3): p. 517-524.
98. Kavanagh, J.M., S. Hussain, T.C. Chilcott, and H.G.L. Coster, *Fouling of reverse osmosis membranes using electrical impedance spectroscopy: Measurements and simulations.* Desalination, 2009. **236**(1): p. 187-193.
99. Fontananova, E., W. Zhang, I. Nicotera, C. Simari, W. van Baak, G. Di Profio, E. Curcio, and E. Drioli, *Probing membrane and interface properties in concentrated electrolyte solutions.* Journal of Membrane Science, 2014. **459**: p. 177-189.
100. Li, Y.H. and K.S. Zhao, *Dielectric analysis of nanofiltration membrane in electrolyte solutions: influences of electrolyte concentration and species on membrane permeation.* Journal of colloid and interface science, 2004. **276**(1): p. 68-76.
101. Antony, A., T. Chilcott, H. Coster, and G. Leslie, *In situ structural and functional characterization of reverse osmosis membranes using electrical impedance spectroscopy.* Journal of Membrane Science, 2013. **425**: p. 89-97.
102. Yeo, S.Y., Y. Wang, T. Chilcott, A. Antony, H. Coster, and G. Leslie, *Characterising nanostructure functionality of a cellulose triacetate forward osmosis membrane using electrical impedance spectroscopy.* Journal of Membrane Science, 2014. **467**: p. 292-302.
103. Gao, Y., W. Li, W.C.L. Lay, H.G.L. Coster, A.G. Fane, and C.Y. Tang, *Characterization of forward osmosis membranes by electrochemical impedance spectroscopy.* Desalination, 2013. **312**: p. 45-51.
104. Amini, M., M. Jahanshahi, and A. Rahimpour, *Synthesis of novel thin film nanocomposite (TFN) forward osmosis membranes using functionalized multi-walled carbon nanotubes.* Journal of Membrane Science, 2013. **435**: p. 233-241.
105. Fang, W., R. Wang, S. Chou, L. Setiawan, and A.G. Fane, *Composite forward osmosis hollow fiber membranes: Integration of RO-and NF-like selective layers to enhance membrane properties of*

anti-scaling and anti-internal concentration polarization. Journal of Membrane Science, 2012. **394**: p. 140-150.
106. Lee, J.-Y., S. Qi, X. Liu, Y. Li, F. Huo, and C.Y. Tang, *Synthesis and characterization of silica gel-polyacrylonitrile mixed matrix forward osmosis membranes based on layer-by-layer assembly.* Separation and Purification Technology, 2014. **124**: p. 207-216.
107. Liu, C., W. Fang, S. Chou, L. Shi, A.G. Fane, and R. Wang, *Fabrication of layer-by-layer assembled FO hollow fiber membranes and their performances using low concentration draw solutions.* Desalination, 2013. **308**: p. 147-153.
108. Liu, H., C. Xiao, Q. Huang, and X. Hu, *Structure design and performance study on homogeneous-reinforced polyvinyl chloride hollow fiber membranes.* Desalination, 2013. **331**(0): p. 35-45.
109. Pardeshi, P. and A.A. Mungray, *Synthesis, characterization and application of novel high flux FO membrane by layer-by-layer self-assembled polyelectrolyte.* Journal of Membrane Science, 2014. **453**: p. 202-211.
110. Puguan, J.M.C., H.-S. Kim, K.-J. Lee, and H. Kim, *Low internal concentration polarization in forward osmosis membranes with hydrophilic crosslinked PVA nanofibers as porous support layer.* Desalination, 2014. **336**(0): p. 24-31.
111. Saren, Q., C.Q. Qiu, and C.Y. Tang, *Synthesis and characterization of novel forward osmosis membranes based on layer-by-layer assembly.* Environmental science & technology, 2011. **45**(12): p. 5201-5208.
112. Setiawan, L., R. Wang, K. Li, and A.G. Fane, *Fabrication of novel poly (amide-imide) forward osmosis hollow fiber membranes with a positively charged nanofiltration-like selective layer.* Journal of Membrane Science, 2011. **369**(1): p. 196-205.
113. Song, X., Z. Liu, and D.D. Sun, *Nano gives the answer: breaking the bottleneck of internal concentration polarization with a nanofiber composite forward osmosis membrane for a high water production rate.* Advanced Materials, 2011. **23**(29): p. 3256-3260.
114. Tian, M., C. Qiu, Y. Liao, S. Chou, and R. Wang, *Preparation of polyamide thin film composite forward osmosis membranes using electrospun polyvinylidene fluoride (PVDF) nanofibers as substrates.* Separation and Purification Technology, 2013. **118**: p. 727-736.
115. Wang, R., L. Setiawan, and A.G. Fane, *Forward osmosis hollow fiber membrane*. 2011.
116. Wang, Y., R. Ou, Q. Ge, H. Wang, and T. Xu, *Preparation of polyethersulfone/carbon nanotube substrate for high-performance forward osmosis membrane.* Desalination, 2013. **330**: p. 70-78.
117. Wei, J., C. Qiu, C.Y. Tang, R. Wang, and A.G. Fane, *Synthesis and characterization of flat-sheet thin film composite forward osmosis membranes.* Journal of Membrane Science, 2011. **372**(1): p. 292-302.
118. Bernstein, R., Y. Kaufman, and V. Freger, *Membrane Characterization*, in *Encyclopedia of Membrane Science and Technology*. 2013, John Wiley and Sons, Inc.
119. Frommer, M.A., J.S. Murday, and R.M. Messalem, *Solubility and diffusivity of water and of salts in an aromatic polyamide film.* European Polymer Journal, 1973. **9**(4): p. 367-373.
120. Hernandez, R.J. and R. Gavara, *Sorption and transport of water in nylon-6 films.* Journal of Polymer Science Part B: Polymer Physics, 1994. **32**(14): p. 2367-2374.
121. Lim, L.T., I.J. Britt, and M.A. Tung, *Sorption and transport of water vapor in nylon 6, 6 film.* Journal of Applied Polymer Science, 1999. **71**(2): p. 197-206.
122. Zhang, X., D.G. Cahill, O. Coronell, and B.J. MariÃ±as, *Partitioning of salt ions in FT30 reverse osmosis membranes.* Applied Physics Letters, 2007. **91**(18): p. 181904.
123. Zhang, X., D.G. Cahill, O. Coronell, and B.J. MariÃ±as, *Absorption of water in the active layer of reverse osmosis membranes.* Journal of Membrane Science, 2009. **331**(1): p. 143-151.

Chapter 3

Activated Carbon Nanofiber Anodes For Microbial Fuel Cells

3.1. Introduction

Microbial fuel cell (MFC) technologies are an emerging approach to wastewater treatment. MFCs are capable of recovering the potential energy present in wastewater and converting it directly into electricity. Using MFCs may help offset wastewater treatment plant operating costs and make advanced wastewater treatment more affordable for both developing and industrialized nations [1]. In spite of the promise of MFCs, their use is limited by low power generation efficiency and high cost. Torres et al. conclude that the biggest challenge for MFC power output lies in reactor design combining high surface area anodes with low ohmic resistances and low cathode potential losses [2]. Power density limitations are typically addressed by the use of better-suited anodes, use of mediators, modification to solution chemistry or changes to the overall system design. Employing a suitable anode, however, is critical since it is the site of electron generation. An appropriately-designed anode is characterized by good conductivity, high specific surface area, biocompatibility and chemical stability.

Anodes currently in use are often made of carbon and/or graphite. Some of these anodes include but are not limited to: graphite plates/rods/felt, carbon fiber/cloth/foam/paper and reticulated vitreous carbon (RVC). Carbon paper, cloth and foams are among the most commonly used anodes and their use in MFCs has been widely reported [3]. Graphite plates or rods are among the simplest materials used as they are relatively inexpensive, easy to handle, and have a defined surface area. Graphite felt electrodes are also available, though the largest surface area achieved for this material is only 0.47 m^2/g and even among that, some of the area is not accessible by the bacteria [3]. When used in granular form, carbon anodes are limited by their final porosity in the

packed bed orientation. High porosity of the bed is important to prevent clogging and minimize pressure drop [3] but at the same time, electrical contact between the individual granules is necessary to maintain sufficient conductivity [4]. Random graphite fibers have been considered as an alternative but fiber clumping was shown to be a factor in the performance of the system [5] thus necessitating better arrangement of the fibers in the anode. Among these conventional materials, no anode design has exhibited all of the necessary characteristics of high porosity, superior interconnectivity, and high conductivity.

Anode materials need to have an open porous structure that has a large bioaccessible surface area. This will allow for extensive biofilm formation throughout the material while enabling efficient transport of nutrients and wastes at the same time. The material also needs to possess a networked structure that can provide a stable support for biofilm attachment. The importance of surface area for power generation has been previously demonstrated [6]. However, for the surface area to play a role in performance, it must be accessible by the bacteria (typical size is $\sim 1-3\ \mu$ m) and thus all of the surface area, usually measured by nitrogen sorption analysis, may not be bioaccessible [4]. Submicron sized pores and their surface may be assessable to bacterial surface structures, such as pili, if the pore is very close to the free surface where bacteria can attach. With increased distances from the surface to the interior of the anode, the bioaccessible surface area will be greatly reduced. Ultra-low thicknesses will also help in reducing overall resistances to electron transport from the biofilm to the anode. Work by He et al. [7] highlights the importance of reducing the internal resistance, R_{in} in an upflow microbial fuel cell and further illustrates the relationship between R_{in} and anode thickness. Transport limitations due to insufficient substrate diffusion were concluded to also contribute to a high R_{in} value. The same diffusion limitations also hinder proton transport. Protons, produced during the oxidation

reaction, locally reduce the pH in the biofilm and can adversely affect bacterial kinetics. This limitation is discussed in detail in the work by Torres et al. [2] where high concentrations of a buffer were added to minimize the build-up of H^+ ions near the biofilm. It has been observed that even a slight reduction in R_{in} can dramatically improve a fuel cell's power generation capabilities [8].

There have thus been many efforts to make new and modified anodes for MFCs to address major limitations such as resistance to mass transport and "bioaccessible" surface area. Some of these involve using carbon nanotubes (CNTs) to greatly increase the surface area and conductivity of a porous matrix, such as polyurethane sponges [9], polyester nonwovens [10] and chitosan scaffolds [11]. All of these studies used two-tiered structures to maximize the anolyte−biofilm−anode interfacial area. Composites incorporating nanomaterials have also been used − polyaniline (PANI)/multiwall carbon nanotubes (MWCNT) [12] and PANI/mesoporous titania (TiO_2) [13] composites are some examples. For MFCs treating wastewater, the highest current density obtained so far, using these new materials, has been 2500 A/m^3 of anode volume [9]. The investigation also reports that using a glucose medium a maximum current density of 21.3 A/m^2 (10,630 A/m^3) was achieved which is close to the highest maximum obtained so far (30 A/m^2) [14] for a microbial bioanode. This highest maximum was obtained using an acetate medium with wastewater-derived biofilms, however the value reported was obtained over the study's time period of only 8 days.

In this study, the use of activated carbon nanofibers nonwoven (ACNFN) as an anode in MFCs was explored. ACNFN has been investigated for use in several applications including supercapacitors, high-temperature filters and nanoelectronics [15]. Nanofibers themselves have

been extensively researched in tissue engineering studies [16] and it has been found that they are uniquely suited for cell growth by virtue of their feature size and high porosity. Their high surface area-to-volume ratio is believed to enhance cell adhesion [17] and [18]. Cell migration, proliferation, and differentiated function are dependent on adhesion and thus, should be enhanced on nanofibers [18]. The ACNFN fabrication procedure, involving pyrolysis and steam activation of an electrospun polyacrylonitrile (PAN) precursor, is simple and scalable. PAN has been extensively studied for making carbon nanofibers [15] and has the advantages of having a high carbon yield, compared to other polymers, and being inexpensive. ACNFN combines nano-sized features and a macroporous structure into one material. The high porosity (porosity of the PAN precursor, calculated from porosimetry measurements, is ~70%), along with the short distances between the free surface and the bulk, enables better nutrient access to the deep interiors facilitating efficient use of the available surface area. The high bioaccessible surface area allows extensive colonization, thereby addressing power density limitations. In this study, batch-mode MFC tests were performed but increasing nutrient solution flow in a flow-through mode will allow for more efficient transport of macromolecules thus mitigating mass transport limitations. ACNFN also has low thicknesses (~130 μ m) that further aid in efficient mass and electron transport throughout the anode. This dimension can be compared to that of other anodes such as the commonly-used carbon cloth (~265 μ m) and granular activated carbon (few mm) or the more novel microchanelled electrodes (4.5 mm) [11] and CNT or graphene-sponge composites (2 mm for both) [9] and [19].

Extensive characterization, including surface morphology, material chemistry, surface area and mechanical strength was performed to validate the use of ACNFN as an anode for MFCs. Preliminary results obtained from testing in a single chamber MFC are reported. The

performance of ACNFN has been compared to that of two commonly-used anodes, granular activated carbon (GAC) and carbon cloth (CC) and found to outperform both by a significant margin.

3.2. Materials and methods

3.2.1. Electrospinning of precursor

Polyacrylonitrile (PAN) from Scientific Polymer Products Inc. (MWavg. 150,000) and dimethylformamide (DMF) from Acros Organics were used to make a 10 wt.% PAN in DMF solution by constant stirring at 60 °C for 24 h. A multi-jet syringe pump (KD Scientific) was used to dispense the charged PAN solution (three syringes with 6 cc each) at a constant rate of 1–1.5 cc/h onto a grounded collector drum rotating at 70 rpm. The applied voltage was 28–30 kV and the tip to collector distance was 18 cm. The precursor mats were all spun at room temperature under a relative humidity of 10–20%.

3.2.2. Fabrication of ACNFN

The electrospun mats were then stabilized in air at 280 °C for 1 h in a muffle furnace (Carbolite) and carbonized in a tube furnace (Lindberg Blue M, Thermo Scientific) at 1000 °C for 1 h in an inert nitrogen atmosphere. The ramp rate for stabilization was 1 °C/min and for carbonization was 5 °C/min. A color change of white to brown was observed after stabilization and to black after carbonization. It was found, that allowing the stabilized sample to cool overnight before carbonization resulted in stronger nonwovens. The carbonized nanofibers (CNF) were activated in the same furnace using steam in an inert nitrogen atmosphere at 800 °C for 1 h using a steam flow rate of 1 g/min.

3.2.3. Scanning electron microscope images

The precursor, stabilized, carbonized and activated samples were sputter coated with platinum and imaged using an E-SEM (FEI Quanta) to obtain the fiber size distribution and analyze possible changes in fiber structure/morphology. Individual fiber sizes were obtained using ImageJ software (National Institutes of Health).

3.2.4. Fourier transform-infra red (FT-IR) analysis

A Nicolet iS10 FT-IR (Thermo Scientific) was used to analyze the surface chemistry of the precursor, stabilized, carbonized and activated samples. Infrared spectra were recorded in the wavenumber range of 500–4000 cm−1 with a resolution of ±4 cm−1 and 16 scans per sample. The attenuated total reflection mode with a diamond crystal was used to scan the samples.

3.2.5. Contact angle analysis

The contact angles of the carbonized and activated samples were measured on a CAM 101 series contact angle goniometer. The values were taken as an average of twenty points with a water droplet volume of 5 ± 0.5 μL.

3.2.6. Mechanical strength analysis

The tensile strength and elasticity of the samples were used as parameters to quantify the mechanical strength of the precursor, stabilized, carbonized and activated samples. A Dynamic Mechanical Analyzer (DMA) from TA instruments was used for this analysis. Sample sizes of 3 cm × 6 mm were used for the tests which were all performed at 25 °C and ambient humidity. All results presented were the average of three individual tests.

3.2.7. Anode surface area and pore size measurements

Specific surface areas and pore size distributions were measured using an ASAP 2020 Physisorption Analyzer (Micromeritics Instrument Corporation). Two commonly used MFC anodes, granular activated carbon (GAC) (General Carbon Corp.) and carbon cloth (CC) (Fuel Cell Earth), were analyzed for comparison to the ACNFN. The samples were first degassed at 300 °C for 1 h (GAC and CC) and 150 °C for 2 h (CNF and ACNFN) and then analyzed for nitrogen sorption at 77 K. Adsorption isotherms were used to calculate the specific surface area through application of the BET model [20] and the total pore volume and pore size distributions were calculated using the BJH method [21]. All results presented were the average of three individual tests.

3.2.8. Biofilm growth on anode materials

Biofilm growth was demonstrated by inoculating CNF and ACNFN with pure cultures of Pseudomonas aeruginosa and Shewanella oniedensis MR-1. P.aeruginosa is a commonly used bacterial strain in biofilm studies and has been well-described previously [4]. S.oniedensis has previously been shown to produce nanowires that facilitate electron transfer to carbon electrodes [22]. GAC and CC were also included as part of this study. The samples were inoculated with the strains and incubated in a SHEL LAB benchtop shaking incubator (Model 1575, Cornelius, OR, USA) at 35 °C for 72 h.

FE-SEM images (JEOL JSM 6335F) were obtained to analyze surface biomass attachment. Quantitative measurements of biomass attachment were conducted by assessed by dry-weight gravimetric measurements. The dry weight of the anode was obtained prior to and after bacterial inoculation. After incubation for 48 h, the samples were dried in a fume hood for 24 h and then in a drying oven for 48 h at 35 °C before measuring the sample weight.

3.2.9. Testing in a single chamber microbial fuel cell (SCMFC)

ACNFN was tested in an air-cathode single chamber microbial fuel cell (SCMFC) as described in other investigations [3]. SCMFCs made of glass bottles (Wheaton Scientific, NJ, USA) with an effective working volume of 100 ml were used in this study. The anode was placed inside the bottle, and the cathode (carbon cloth – 30% wet proofing, Fuel Cell Earth; geometric area: 3 cm2) was placed in the extension arm of the bottle. The cathode face that was in contact with the solution in the SCMFCs was doped with platinum (a mixture of 10 wt.% platinum in carbon black) (0.5 mg/cm2 of mixture applied), while the other cathode side, facing air, was coated with three layers of polytetrafluoroethylene (PTFE) to slow oxygen flux that could result in oxidation at the anode. The anode-cathode distance was maintained at 4 cm. The influent wastewater to the University of Connecticut Wastewater Treatment Plant that contained diverse anaerobic bacteria was used as inocula in the anode chamber. The voltage over an external resistance (Rext) of 100 Ω was recorded by a data log system (Keithley 2700) at intervals of 2 h. The SCMFCs were operated in an incubator maintained at 30 °C. Polarization and power density curves were used to compare the performances of ACNFN, GAC and CC.

3.3. Results and discussion

3.3.1. Scanning electron microscope images

Fig. 3.1 shows the E-SEM images of the precursor, stabilized, carbonized and activated samples and Fig. 3.2 shows the corresponding average fiber distributions. The average fiber size was seen to decrease with each pyrolysis step which was consistent with previous work [23]. The decrease in fiber size can be attributed to weight loss and densification of the fiber. The fibers also changed from a rigid to a spaghetti-like morphology as a result of the heat treatment. This

was possibly due to 'reaction shrinkage' that occurs during stabilization. The cyclization reaction causes the linear polyacrylonitrile chains to form a 'ladder polymer' structure [24] and may be the cause for the loss of rigidity of the individual fibers. The carbon yield from this method of fabrication was 44%.

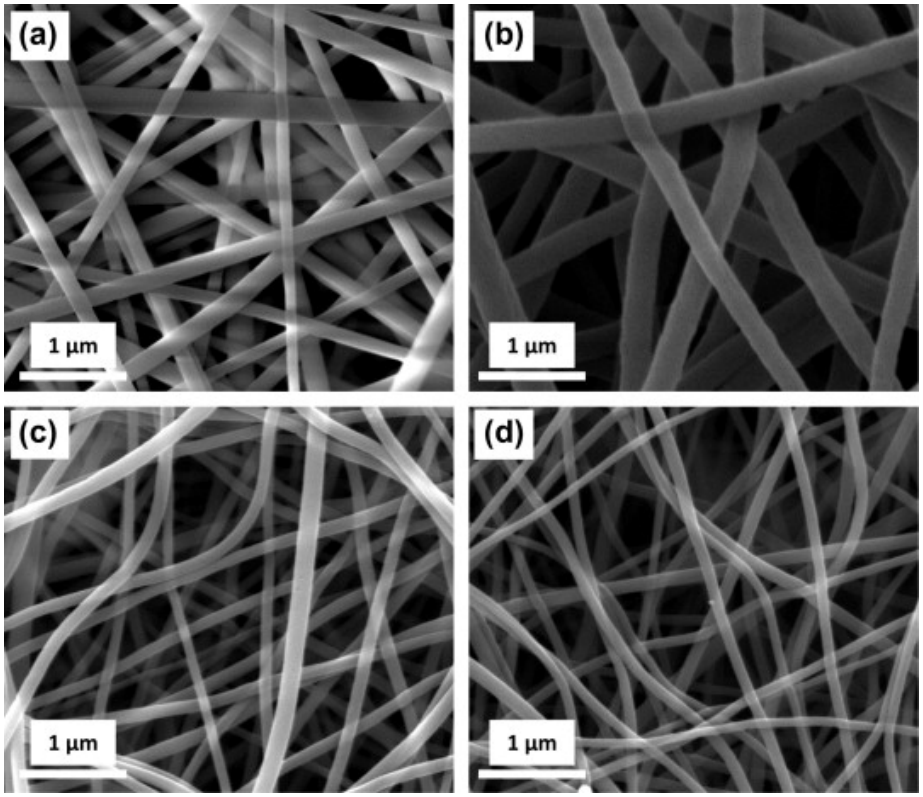

Figure 3.1 - ESEM images of (a) PAN precursor (b) stabilized PAN (c) carbon nanofibers (CNF) (d) activated carbon nanofibers nonwoven (ACNFN). Fiber orientation changes from taut (a) to loose for the heat-treated fibers (b, c, d).

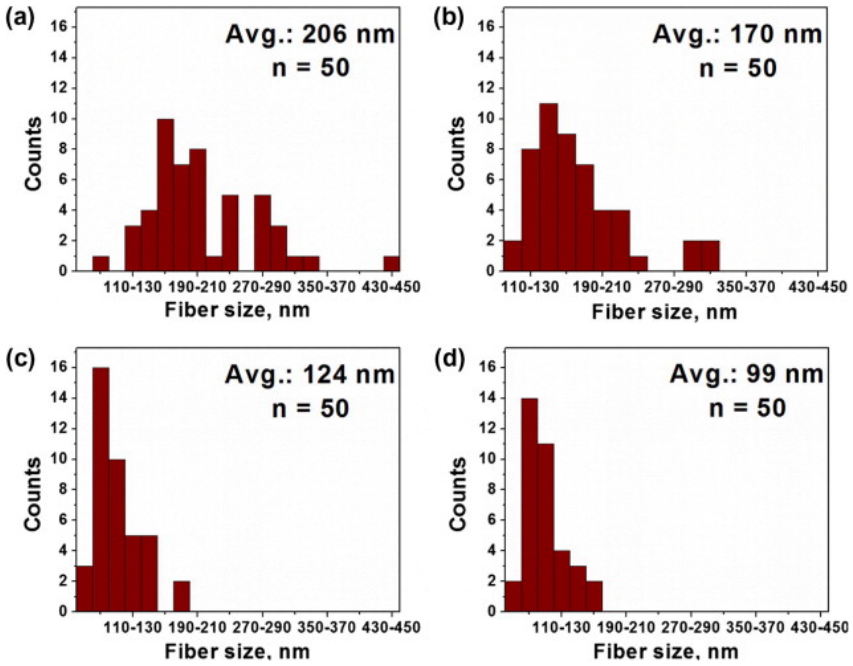

Fig. 3.2. Fiber size distributions for (a) PAN precursor (b) stabilized PAN (c) carbonized nanofibers (CNF) (d) activated carbon nanofibers nonwoven (ACNFN).

3.3.2. Fourier transform-infra red (FT-IR) analysis

Fig. 3.3 shows the FT-IR spectra for the precursor (Fig. 3.3a), stabilized (Fig. 3.3b) and carbonized and activated species (Fig. 3.3c). Post-stabilization a decrease in the intensities at 2900 and 1450 cm^{-1}, corresponding to aliphatic C−H bonds, was observed. Between Fig. 3.3a and b a distinct increase in absorbance was observed in the peaks between 1580 and 1700 cm^{-1}, which correspond to the C=N, C=C and C=O bonds present in the stabilized mat. The large peak at 1590 cm^{-1} confirmed completion of the cyclization and dehydrogenation reactions during stabilization forming C=N and C=C bonds, respectively. The reaction of the nitrile group in PAN forms conjugated C=N containing structures which result from intramolecular cyclization or intermolecular crosslinking [25]. The generation of conjugated C=C bonds results from dehydrogenation or from imine−enamine tautomerization and subsequent isomerization [25]. The shoulder-like peak at 1700 cm^{-1} corresponding to C=O bonds indicated successful oxidation of

the material. The peak observed at 810 cm^{-1} in 3.3b corresponds to the C=C−H group that is present in the final stabilized structure [26] and [27]. The spectroscopic analysis thus confirmed the occurrence of cyclization, dehydrogenation and oxidation reactions during stabilization. No distinct peaks were found in the spectrum for CNF or ACNFN suggesting that the samples were mostly carbon [24]. The section below does, however, identify some small differences between the two spectrums as a result of steam activation that may explain a change in hydrophilicity after activation.

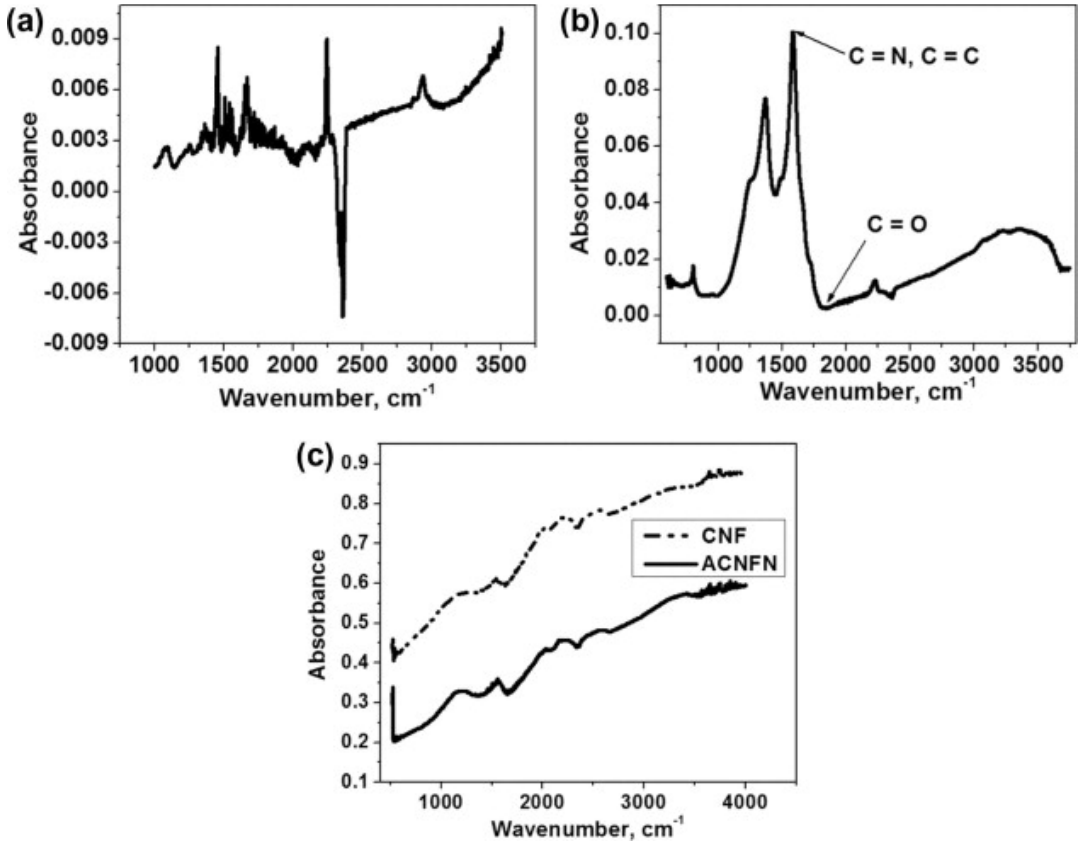

Figure 3.3 - FT-IR spectrums for (a) PAN precursor (b) stabilized PAN (c) carbon nanofibers (CNF) and activated carbon nanofibers nonwoven (ACNFN).

3.3.3. Contact angle analysis

Fig. 3.4 shows the contact angles of CNF and ACNFN. There is a marked decrease in the hydrophobicity of CNF after activation. This is not surprising since activation oxidizes the surface of the material. While water is believed to be adsorbed in its molecular state during the steam activation process [28] exposure to oxygen at room or higher temperatures is believed to result in the formation of acidic surface groups [29]. The acidic, hydrophilic nature of several activated carbons has been studied by many investigators and a significant body of literature exists on the characterization of these materials [30], [31], [32] and [33]. The FT-IR results indicate a slight increase in the intensity of the broad peak from 1160−1200 cm^{-1} after steam activation (Fig. 3.3c). This peak corresponds to the O−H bond in the phenolic groups [31]. In the same figure, an increase in the intensity of the peak at 1580 cm^{-1} after steam activation was observed; this has been previously assigned to aromatic ring stretching coupled to highly conjugated carbonyl groups (C=O) [33]. The presence of these functional groups likely contributes to the increased hydrophilicity of the steam activated samples. It was found, from electrochemical impedance spectroscopy (EIS) measurements, that steam activation decreased the conductivity from 3.05 S/cm (CNF) to 0.19 S/cm (ACNFN). There are surface modifications that could be employed to increase the surface charge on the electrode [34]. Also, current collectors such as stainless steel could be used to increase the conductivity [19].

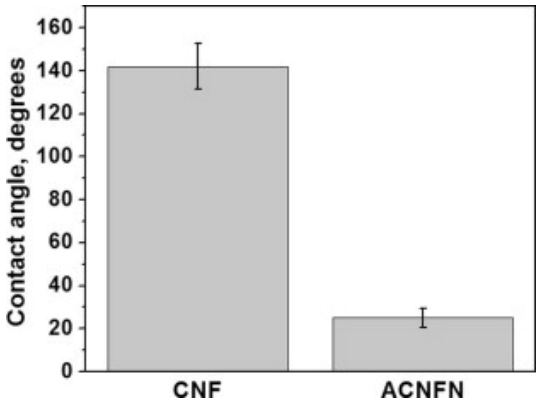

Figure 3.4 - Contact angles of CNF and ACNFN samples showing a marked decrease in hydrophobicity post-activation.

3.3.4. Mechanical strength analysis

Fig. 3.5a shows a representative stress–strain curve for the precursor, stabilized, carbonized and activated samples. It is to be noted that in Fig. 3.5a the precursor data was only shown up to 3.0% strain (actual data goes to ~ 80% strain) in order to allow for ease of comparison between the four species. The break strength is denoted by the last data point in the stress-strain curve at which the sample breaks under the applied stress. It was found to decrease with each heat treatment step as depicted in Fig. 3.5b. The slope of the curve gives the Young's modulus which is a measure of the elasticity of the sample. This value was also shown to decrease with heat treatment as seen in Fig. 3.5b. Since the anode must support a biofilm, reduced strength could be problematic. Breakage or fragmentation of the anode could contaminate the treated wastewater and reduce power output. Increasing the strength and flexibility will be essential for application of these carbon materials to MFCs.

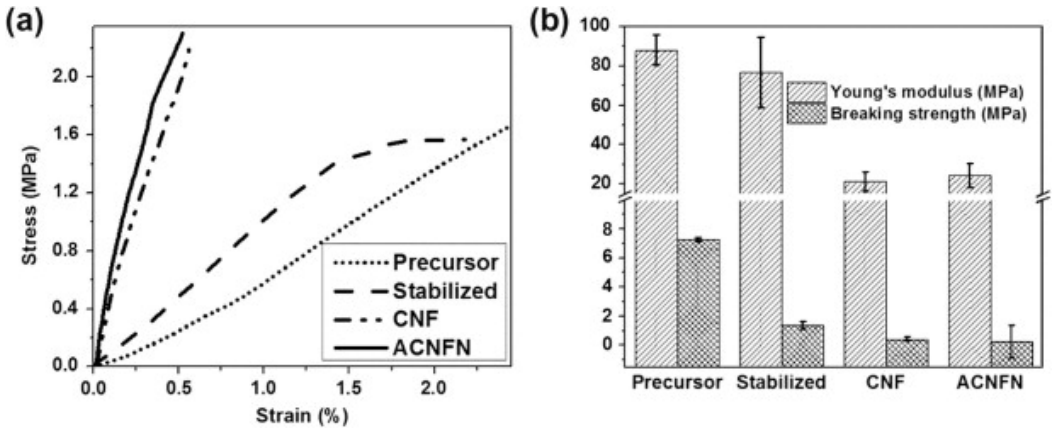

Figure 3.5 – Mechanical strength analysis of the precursor, stabilized, CNF and ACNFN samples. 3.5a shows the stress-strain curves and 3.5b shows the Young's modulus and breaking strength values. The breaking strength is obtained from the last point in the stress-strain curve and the Young's modulus is obtained from the slope of the curve. All results are from dynamic

mechanical analysis performed at 25°C. n=3 for the precursor, stabilized and CNF samples and n=1 for ACNFN.

3.3.5. Anode surface area and pore size measurements

Fig. 3.6 shows the adsorption isotherms of granular activated carbon (GAC), ACNFN and carbon cloth (CC). The GAC isotherm is mostly type I albeit the curve inflects a little upward as the relative pressure over the system (P/Po) is increased and appears to be type II [1]. The isotherm indicates the presence of some micropores in GAC. The isotherm for CC is strictly type II whereas that of ACNFN is both type I and II [1]. The specific surface area (SSA) of the three anode materials are summarized in Table 3.1.

Table 3.1 - Specific surface area characterization by BET analysis (n=3).

Sample	BET SSA[a] (m^2/g)	BJH SSA[b] (m^2/g)	b/a[c] (%)
GAC	842.63	536.084	64
CC	0.11	0.013	12
Precursor	9.16	-	-
CNF	25.31	13.502	-
ACNFN	1158.75	404.033	35

The requirement of high anode surface area to achieve high power densities has been stressed in previous investigations on MFCs [35] and [36]. As was previously noted in the introduction, not all of the available surface area in a material may be accessible by the bacteria during biofilm growth [37] and [38]. However, the effective or bioaccessible surface area of ACNFN is much higher than other activated carbons like GAC due to a smaller average distance between the fiber “free surface” and the internal porosity, thus also facilitating efficient electron transfer to the anode. Further, this inherent macroporosity of ACNFN enhances nutrient access to

the interiors of the anode thus making more biomass viable for a given volume of anode. In essence, the biofilm is not simply growing on a surface. It is growing within a network of conductive fibers and thus can grow more biomass and achieve a higher power output. It can be seen from Table 3.1 that the specific surface area of ACNFN is much higher than that of GAC. Of this surface area 65% comes from pores larger than 0.3 μm (typical size of bacteria is ~1–3 μm) compared with 36% of the surface area on GAC. Evidently, ACNFN has a greater amount of SSA accessible by bacteria for biofilm formation and growth.

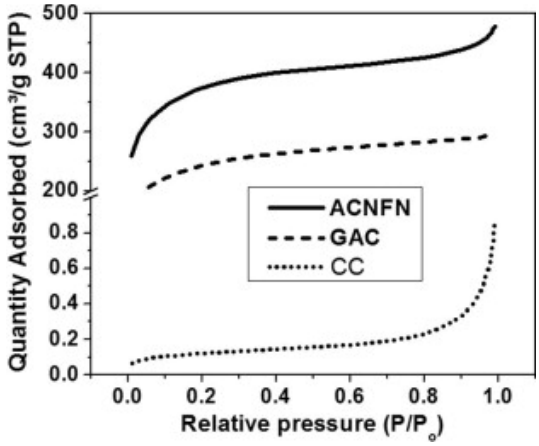

Figure 3.6 - Nitrogen adsorption isotherms of granular activated carbon (GAC), ACNFN and carbon cloth (CC) from BET analysis. The GAC isotherm is mostly type I indicating the presence of some micropores. The CC isotherm is strictly type II whereas that of ACNFN is both type I and II.

3.3.6. Growth of bacterial biofilm on anode materials

Fig. 3.7 demonstrates biofilm growth on the different anode materials. Fig. 3.7a and b show biofilm growth on ACNFN using pure culture strains of P.aeruginosa and S.oniedensis MR-1. 3.7c and e are SEM images of native GAC and CC and 3.7d and f correspond to biofilm growth, using S.oniedensis MR-1, on these materials. In Fig. 3.7a and b, a well-developed biofilm can be seen on the surface of the material. This also seems to be the case for GAC (Fig.

3.7d) whereas the low surface area of CC led to poor biofilm formation as seen in Fig. 3.7f. Thus the effect of surface area on biofilm formation can be clearly seen. In order to quantify biofilm growth, the amount of biofilm per gram of material was measured for each anode and the results are summarized in Fig. 3.8. It can be seen that the amount of biofilm growth on ACNFN was about 3.2–4.2 times that on CC and 6.4–8.4 times the amount on GAC. This occurred in spite of the increased hydrophilicity of the ACNFN. It has been found that the presence of EPS and lipopolysaccharides aids in biofilm attachment to hydrophilic substances [39]. It is interesting to note that even though the SEM images in Fig. 3.7 showed that both ACNFN and GAC had extensive biofilm growth on the surface, the overall biofilm growth on ACNFN was much higher than that of GAC. This proves that the internal macroporosity of ACNFN plays a crucial role in efficient exploitation of the available surface area. Further, it can be seen that the adhesion onto CC is greater than that for GAC (1.52–2.67 times higher) in spite of the fact that CC was non-activated and GAC had relatively high surface area. It can thus be concluded that the combination of material interconnectivity and bioaccessible surface area is vital for an efficient anode material.

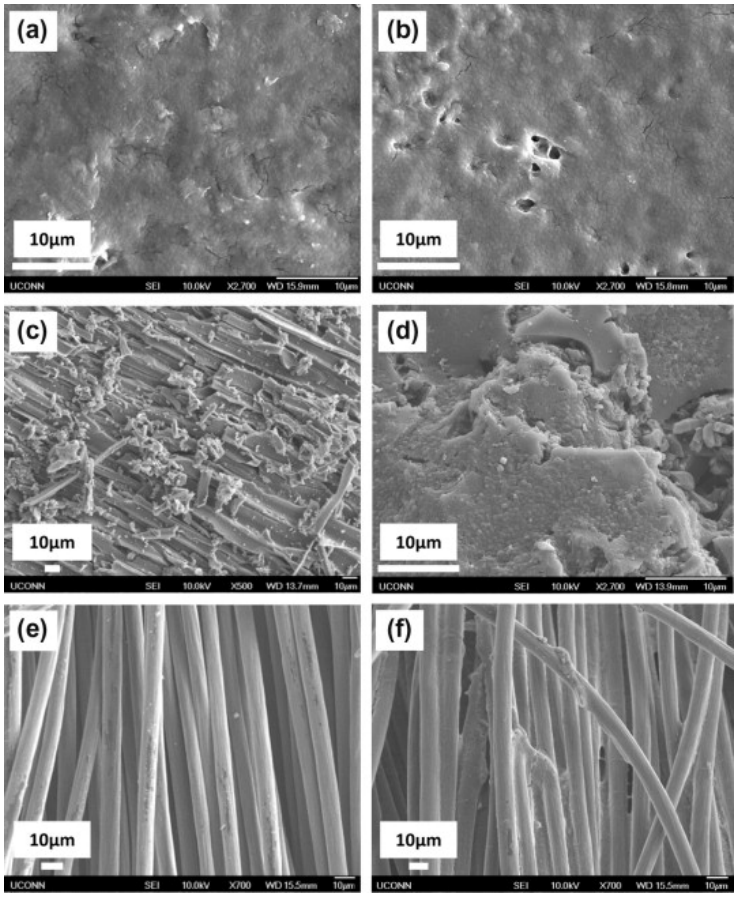

Figure 3.7 - FE-SEM images showing biomass attachment on (a and b) ACNFN using pure culture strains of *Pseudomonas aeruginosa* and *Shewanella oniedensis* MR-1. 3.7c and 3.7e show images of native GAC and CC and 5d and 5f are the corresponding images with biofilm grown using *Shewanella oniedensis* MR-1. All biofilms were grown by incubating the materials for 72 hours in a shaker.

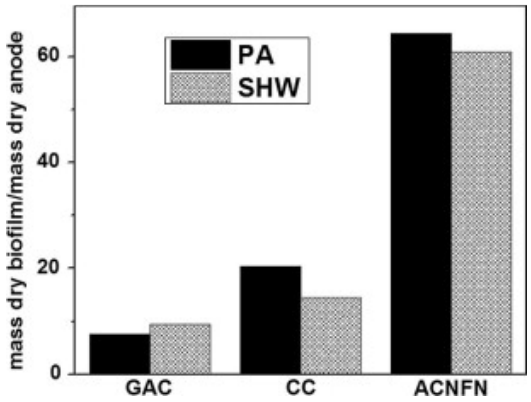

Figure 3.8 – Percent increase in anode mass post-biofilm adhesion. It can be seen that the increase is highest for ACNFN. Bacterial strains used were *Pseudomonas aeruginosa* (PA) and *Shewanella oniedensis* MR-1 (SHW).

3.3.7. Testing in a single chamber microbial fuel cell (SCMFC)

The polarization and power density curves obtained from preliminary tests in a SCMFC are shown in Fig. 3.9(a and b). The polarization curve indicates how well the MFC maintains a voltage as a function of current generation as the external resistance is increased from 15 to 2940 Ω. Fig. 3.9a shows that the open circuit voltage (OCV) obtained from ACNFN (0.46 V) is higher than that obtained from CC and GAC (0.4 and 0.41 V, respectively). ACNFN was also able to sustain increased current generation better than CC and GAC. Fig. 3.9b shows representative power and current densities, normalized to anode volume, obtained over a period of 10 weeks. The normalization to anode volume was chosen, over the conventional anode area, in order to more completely depict the effect of the material tested. The maximum current density obtained was 2714.646 A/m3 which is about 10% higher than the highest maximum obtained so far in the literature (2500 A/m3 using a CNT-sponge composite anode [9]). This was achieved in spite of the lower conductivity of the ACNFN (0.19 S/cm when compared to 1 S/m for the composite). These results only represent the first generation material and no optimization for activation, fiber size, mat thickness, surface charge, or conductivity has been evaluated. The power density obtained from ACNFN (758 W/m3) was dramatically higher than that obtained from CC and GAC (161 and 3.4 W/m3, respectively). The open porous structure of ACNFN had promoted active colonization of the substrate in the 10 week period studied leading to a high sustained power generation. The fact that the power density generated in the GAC system was much lower than that of CC and ACNFN further reiterates the importance of an open interconnected structure and “bioaccessible” surface area. It is expected that by operating in a flow-through mode, with mixing in the anode chamber, far higher power densities can be obtained by overcoming mass transfer limitations typical of batch systems.

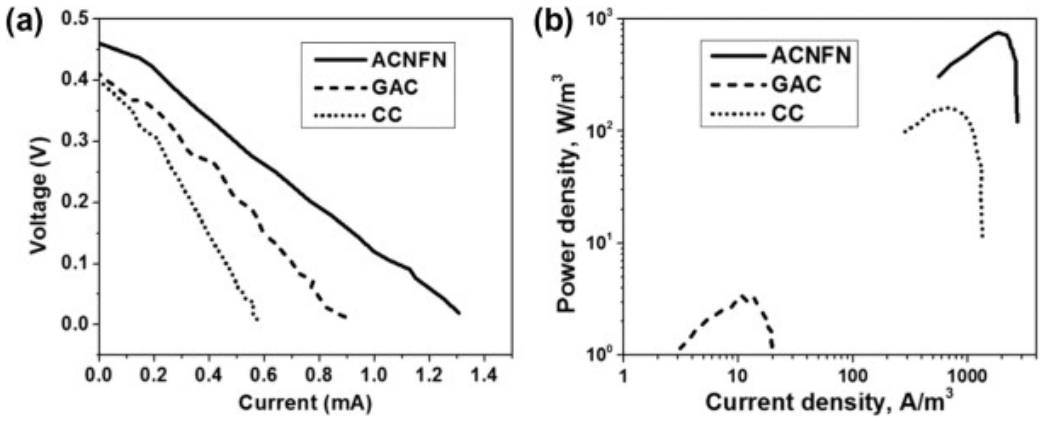

Fig. 3.9. Polarization (a) and power density (b) curves from SCMFC testing. Power densities are normalized to volume of anode material. Carbon cloth was used as the cathode and an external resistance of 100 Ω was used to obtain the power densities, which were obtained over a period of 10 weeks.

3.4. Concluding remarks

Activated carbon nanofibers nonwovens were shown to be a promising anode material for the MFC wastewater treatment platform. They possess a large bioaccessible surface area and have an open porous structure that promotes well-supported biofilm growth. Their viability as an MFC anode was demonstrated by preliminary tests in a single chamber microbial fuel cell in which their bio-electrochemical performance was exponentially better compared to that of commonly-used anodes. The current densities obtained are on par with the highest value reported so far, even with far lower conductivities. It is expected that by increasing the conductivity of the material and by operating in a flow-through mode fashion much greater outputs can be realized. Also, increasing the nutrient solution flow in the flow-through mode will help mitigate reduced transport within the matrix that might occur with establishment of a well-developed biofilm. Use of a buffer solution together with mixing in the anode chamber can help overcome common proton accumulation issues. Relative to other anodes, the mass, or volume, of anode material

needed to achieve a given power density is considerably lower, thus permitting the design of smaller fuel cells with different configurations which could yield even higher power. Also, increasing the hydrophobicity by adopting surface modifications or using alternate methods of activation will lead to a further increase in the power density achievable with this novel material.

References

[1] Liu H, Ramnarayanan R, Logan BE. Production of Electricity during Wastewater Treatment Using a Single Chamber Microbial Fuel Cell. Environmental Science & Technology. 2004;38(7):2281-5.

[2] Torres CI, Kato Marcus A, Rittmann BE. Proton transport inside the biofilm limits electrical current generation by anode-respiring bacteria. Biotechnology and Bioengineering. 2008;100(5):872-81.

[3] Logan BE, Hamelers B, Rozendal R, Schroder U, Keller J, Freguia S, et al. Microbial Fuel Cells: Methodology and Technology. Environmental Science & Technology. 2006;40(17):5181-92.

[4] Logan BE. Microbial fuel cells: John Wiley and Sons Inc. 2007.

[5] Logan B, Cheng S, Watson V, Estadt G. Graphite Fiber Brush Anodes for Increased Power Production in Air-Cathode Microbial Fuel Cells. Environmental Science & Technology. 2007;41(9):3341-6.

[6] Feng Y, Yang Q, Wang X, Logan BE. Treatment of carbon fiber brush anodes for improving power generation in air-cathode microbial fuel cells. Journal of Power Sources. 2010;195(7):1841-4.

[7] He Z, Minteer SD, Angenent LT. Electricity Generation from Artificial Wastewater Using an Upflow Microbial Fuel Cell. Environmental Science & Technology. 2005;39(14):5262-7.

[8] Mench MM, Wang C, Thynell ST. An introduction to fuel cell and related transport phenomena. International Journal of Transport Phenomena. 2001;3.

[9] Xie X, Ye M, Hu L, Liu N, McDonough JR, Chen W, et al. Carbon nanotube-coated macroporous sponge for microbial fuel cell electrodes. Energy & Environmental Science. 2012;5(1):5265-70.

[10] Xie X, Hu L, Pasta M, Wells GF, Kong D, Criddle CS, et al. Three-Dimensional Carbon Nanotube-Textile Anode for High-Performance Microbial Fuel Cells. Nano Letters. 2011;11(1):291-6.

[11] Katuri K, Ferrer ML, Gutierrez MC, Jimenez R, del Monte F, Leech D. Three-dimensional microchanelled electrodes in flow-through configuration for bioanode formation and current generation. Energy & Environmental Science. 2011;4(10):4201-10.

[12] Qiao Y, Li CM, Bao S-J, Bao Q-L. Carbon nanotube/polyaniline composite as anode material for microbial fuel cells. Journal of Power Sources. 2007;170(1):79-84.

[13] Qiao Y, Bao S-J, Li CM, Cui X-Q, Lu Z-S, Guo J. Nanostructured Polyaniline/Titanium Dioxide Composite Anode for Microbial Fuel Cells. ACS Nano. 2007;2(1):113-9.

[14] Chen S, Hou H, Harnisch F, Patil SA, Carmona-Martinez AA, Agarwal S, et al. Electrospun and solution blown three-dimensional carbon fiber nonwovens for application as electrodes in microbial fuel cells. Energy & Environmental Science. 2011;4(4):1417-21.

[15] Liu C-K, Lai K, Liu W, Yao M, Sun R-J. Preparation of carbon nanofibres through electrospinning and thermal treatment. Polymer International. 2009;58(12):1341-9.

[16] Barnes CP, Sell SA, Boland ED, Simpson DG, Bowlin GL. Nanofiber technology: Designing the next generation of tissue engineering scaffolds. Advanced Drug Delivery Reviews. 2007;59(14):1413-33.

[17] Pham QP, Sharma U, Mikos AG. Electrospinning of Polymeric Nanofibers for Tissue Engineering Applications: A Review. Tissue Engineering. 2006;12(5):1197-211.
[18] Smith LA, Ma PX. Nano-fibrous scaffolds for tissue engineering. Colloids and Surfaces B: Biointerfaces. 2004;39(3):125-31.
[19] Xie X, Yu G, Liu N, Bao Z, Criddle CS, Cui Y. Graphene-Sponges as High-Performance Low-Cost Anodes for Microbial Fuel Cells. Energy & Environmental Science. 2012;5:6862–6.
[20] Brunauer S, Emmett PH, Teller E. Adsorption of gases in multimolecular layers. Journal of the American Chemical Society. 1938;60(2):309-19.
[21] Barrett EP, Joyner LG, Halenda PP. The determination of pore volume and area in porous substances. I. Computations from nitrogen isotherms. Journal of the American Chemical Society. 1951;73:373-80.
[22] Gorby YA, Yanina S, McLean JS, Rosso KM, Moyles D, Dohnalkova A, et al. Electrically conductive bacterial nanowires produced by Shewanella oneidensis strain MR-1 and other microorganisms. Proceedings of the National Academy of Sciences. 2006 July 25, 2006;103(30):11358-63.
[23] Rahaman MSA, Ismail AF, Mustafa A. A review of heat treatment on polyacrylonitrile fiber. Polymer Degradation and Stability. 2007;92(8):1421-32.
[24] Chung DDL. Carbon fiber composites: Butterworth-Heinemann 1994.
[25] Dalton S, Heatley F, Budd PM. Thermal stabilization of polyacrylonitrile fibres. Polymer. 1999;40(20):5531-43.
[26] Zhang W-x, Wang Y-z, Sun C-f. Characterization on oxidative stabilization of polyacrylonitrile nanofibers prepared by electrospinning. Journal of Polymer Research. 2007;14(6):467-74.
[27] A. K. Gupta D.K. Paliwal, Pushpa Bajaj. Acrylic Precursors for Carbon Fibers. Journal of Macromolecular Science, Part C: Polymer Reviews. 1991;31(1):1-89.
[28] Gadsby J, Hinshelwood CN, Sykes KW. The Kinetics of the Reactions of the Steam-Carbon System. Proceedings of the Royal Society of London Series A Mathematical and Physical Sciences. 1946 October 22, 1946;187(1009):129-51.
[29] Bismarck A, Wuertz C, Springer J. Basic surface oxides on carbon fibers. Carbon. 1999;37(7):1019-27.
[30] Considine R, Denoyel R, Pendleton P, Schumann R, Wong S-H. The influence of surface chemistry on activated carbon adsorption of 2-methylisoborneol from aqueous solution. Colloids and Surfaces A: Physicochemical and Engineering Aspects. 2001;179(2-3):271-80.
[31] Fanning PE, Vannice MA. A DRIFTS study of the formation of surface groups on carbon by oxidation. Carbon. 1993;31(5):721-30.
[32] Machnikowski J, Grzyb B, Machnikowska H, Weber JV. Surface chemistry of porous carbons from N-polymers and their blends with pitch. Microporous and Mesoporous Materials. 2005;82(1-2):113-20.
[33] Moreno-Castilla C, López-Ramón MV, Carrasco-Marín F. Changes in surface chemistry of activated carbons by wet oxidation. Carbon. 2000;38(14):1995-2001.
[34] Cheng S, Logan BE. Ammonia treatment of carbon cloth anodes to enhance power generation of microbial fuel cells. Electrochemistry Communications. 2007;9(3):492-6.
[35] Zhao F, Rahunen N, Varcoe JR, Roberts AJ, Avignone-Rossa C, Thumser AE, et al. Factors affecting the performance of microbial fuel cells for sulfur pollutants removal. Biosensors and Bioelectronics. 2009;24(7):1931-6.
[36] Logan BE. Peer Reviewed: Extracting Hydrogen and Electricity from Renewable Resources. Environmental Science & Technology. 2004;38(9):160A-7A.

[37] Liu Y, Harnisch F, Fricke K, Schröder U, Climent V, Feliu JM. The study of electrochemically active microbial biofilms on different carbon-based anode materials in microbial fuel cells. Biosensors and Bioelectronics. 2010;25(9):2167-71.

[38] Ramasamy RP, Ren Z, Mench MM, Regan JM. Impact of initial biofilm growth on the anode impedance of microbial fuel cells. Biotechnology and Bioengineering. 2008;101(1):101-8.

[39] Donlan RM. Biofilms: Microbial Life on Surfaces. Emerging Infectious Diseases. 2002;8(9):881-90.

Chapter 4

Evaluation of Characterization Techniques Using Nonwovens as a Platform Material

4.1. Introduction

The previous chapter detailed the work on fabricating and characterizing ACNFN as novel anodes for MFCs. The impressive performance of the anode material was attributed to improved structure-performance relations of the nonwoven. This chapter seeks to explore such structures using comprehensive 3D characterization techniques. The nonwovens evaluated herein are also commonly used as backing layers in EO membranes (commercial polyesters) as well as novel supports for such osmotic membranes (electrospun nanofibers). Basic characteristics such as fiber and pore size were first evaluated using scanning electron microscopy and capillary flow porometry, respectively. Then, the 3D structures were comprehensively characterized using analytical and imaging techniques like liquid extrusion and mercury intrusion porosimetry and x-ray computed tomography. The findings from this characterization work enabled understanding of the applicability of the different techniques and to evaluate their pros and cons for characterizing soft materials.

4.2. Materials and methods

4.2.1 Materials

Commercially available polyester (PET) nonwovens and electrospun polyacrylonitrile (PAN) mats were used as the nonwoven samples for this study. The PET nonwovens were use as received and designated Cooltexx (Freudenberg), FO2425N/30 (Freudenberg) and 16-1 (Sanko). The electrospun nonwovens consisted of PAN nanofibers spun from three concentrations (8%, 10% and 12wt %) of PAN (Scientific Polymer Products) solutions in dimethylformamide (DMF)

(Acros Organics). The solutions were stirred at 60°C for two hours and then cooled to 30°C while stirring for another 22 hours.

4.2.2 Characterization Methods

4.2.2.1. Scanning Electron Microscopy

Scanning electron microscopy (SEM) images of the nonwovens were obtained (Phenom, FEI) to determine fiber size, quality and morphology. ImageJ software (NIH) was used to calculate fiber size from the SEM images.

4.2.2.2 Porosimetry and porometry

Two kinds of porosimeters, a liquid extrusion porosimeter from Porous Materials Inc. (PMI) [18] and a mercury intrusion porosimeter (PoreMaster, Quantachrome), were used to analyze the pore structure of the nonwovens. The test liquids used in the two porosimeters were Galwick™ (Porous Materials Inc.) and mercury, respectively. Galwick and mercury have surface tensions of 15.9 dynes/cm and 480 dynes/cm, respectively. Galwick™ is the proprietary wetting liquid for PMI's porosimeter and is considered a surfactant that can wet almost any sample. It was assumed that Galwick completely wetted out the samples tested and hence a contact angle of 0° was taken for calculations of pore diameter using the Young-Laplace equation [19]:

$$P.d = 4\gamma.cos\theta \qquad (2)$$

P is the extrusion pressure in MPa, d is the pore diameter in µm, γ is the surface tension of Galwick in N/m and θ is the contact angle of Galwick with the sample, in degrees. For intrusion methods, a contact angle of 140° for mercury was assumed to calculate pore diameters according to the Washburn equation [20]. The Washburn equation is similar to the Young-Laplace equation

except that a negative sign is used on the right-hand side to correct for the negative values of cos 140° (or any contact angle above 90°).

The use of these equations also requires the assumption that the "pores" being measured are cylindrical. This assumption is not valid for nonwovens, but the results are indicative of effective cylindrical pore sizes. Each technique also is biased and may result in variation in pore size and pore volume measurements. For example, the intrusion technique can detect through pores and blind pores while extrusion can only detect through pores. Extrusion porosimetry, therefore, may give a more accurate estimate of the porosity contributing to transport through the nonwoven (i.e. for filtration). For this study, all porosimetry results presented are the average of three individual tests.

The data from the porosimetry techniques was used to calculate the porosity using the formula shown below (Equation 3).

$$\%\ Porosity = \frac{\left(Cumulative\ pore\ volume, \frac{cc}{g}\right).(Mass\ of\ sample, g)}{(Mass\ of\ sample, g)/(Density\ of\ sample, \frac{g}{cc})} * 100 \qquad (3)$$

The cumulative pore volume value was obtained from the instrument software. The densities of the commercial PET nonwovens (Cooltexx and FO2425N/30) were obtained from Freudenberg. For 16-1 and electrospun PAN, the densities were calculated by measuring the mass and dimensions of a stack of circular samples punched out using a punch of known diameter. The porosities obtained from the two porosimetry techniques were then compared to those calculated with the use of a formula that is often used in the nonwoven industry (Equation 4).

$$Porosity, \% = \frac{(Volume\ of\ nonwoven, \frac{cc}{g} - Volume\ of\ polymer, \frac{cc}{g})}{Volume\ of\ nonwoven, \frac{cc}{g}} * 100 \qquad (4)$$

The volume of the nonwoven was taken as the inverse of the density of the nonwoven that was used in (4). The volume of the polymer in the nonwoven was obtained from pycnometry measurements. This approach to calculate porosities of nonwovens has been previously used in many investigations [10, 15, 24] but a key limitation has been the need to know the true value of the polymer density in the spun form (for electrospun materials).

A capillary flow porometer (Porous Materials Inc.) was used to calculate the most constricted pore size (pore throat diameter) of the nonwovens to validate their efficacy in filtration applications. The samples were wetted out with Galwick prior to testing and were evaluated for their bubble point diameter and the pore throat diameter with the use of Equation 2.

4.2.2.3 X-ray computed tomography

X-ray computed tomography images of the nonwovens were obtained using a MicroXCT-400 from Xradia Inc. For XCT imaging samples of about 1 cm x 0.5 cm were mounted onto the sample stage and a total of 4000 projections (3000 projections for FO2425N/30) were taken at equal increments as the stage was rotated through 180°, using a 20X objective. The 2-D images that were obtained were then exported for image processing and analysis using Avizo™Fire software (VSG). Section sizes of 800x800x800 were considered for analysis from the original 971x971x4000 (971x971x3000 for FO2425N/30) volume. These sections were filtered to remove background noise and manually thresholded to obtain binarized images in which pixels above a certain intensity were labeled fibers and all pixels below that threshold were designated as pores. The section was then analyzed for its porosity using 'volume3d', a built-in measurement tool used to compute the density of pixels above a certain intensity threshold in the 3-D volume. Three different sections from non-overlapping regions

were examined and analyzed to obtain an average porosity. Only the PET nonwovens were imaged using this technique since the average fiber diameter of the electrospun nanofibers (few hundred nanometers) was below the resolution limit of the XCT instrument (0.5-2 µm) used in this study.

4.3. Results and discussion

4.3.1 Intrusion versus extrusion porosimetry

4.3.1.1 Polyester nonwoven

Figure 4.1 shows the SEM images of the PET nonwovens. Cooltexx and FO2425N/30 were seen to clearly have an open fibrous network while 16-1 seemed to have undergone a calendaring finishing process which caused the nonwovens to melt at some locations.

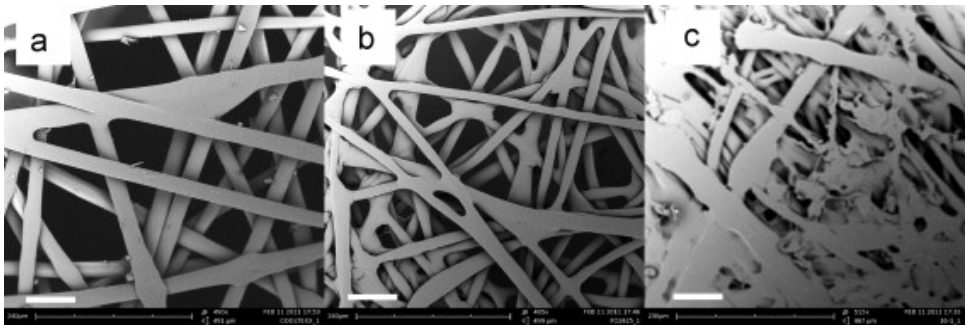

Figure 4.1 - SEM images of PET nonwovens. a) Cooltexx; b) FO2425N/30; and c) 16-1 at 490X, 485X and 515X respectively. Scale bar on image represents a length of 60 µm.

Between the two techniques, the mercury intrusion method generally exhibited a lower porosity for open fibrous structures. Table 4.1 provides a summary of the porosities of the nonwovens calculated using the two techniques.

Figures 4.2a-f present a comparison of the LEP and MIP pore diameter distributions for Cooltexx, FO2425N/30 and 16-1 respectively. Figures 4.2a-c show the LEP histograms and Figures 4.2d-f are those of MIP.

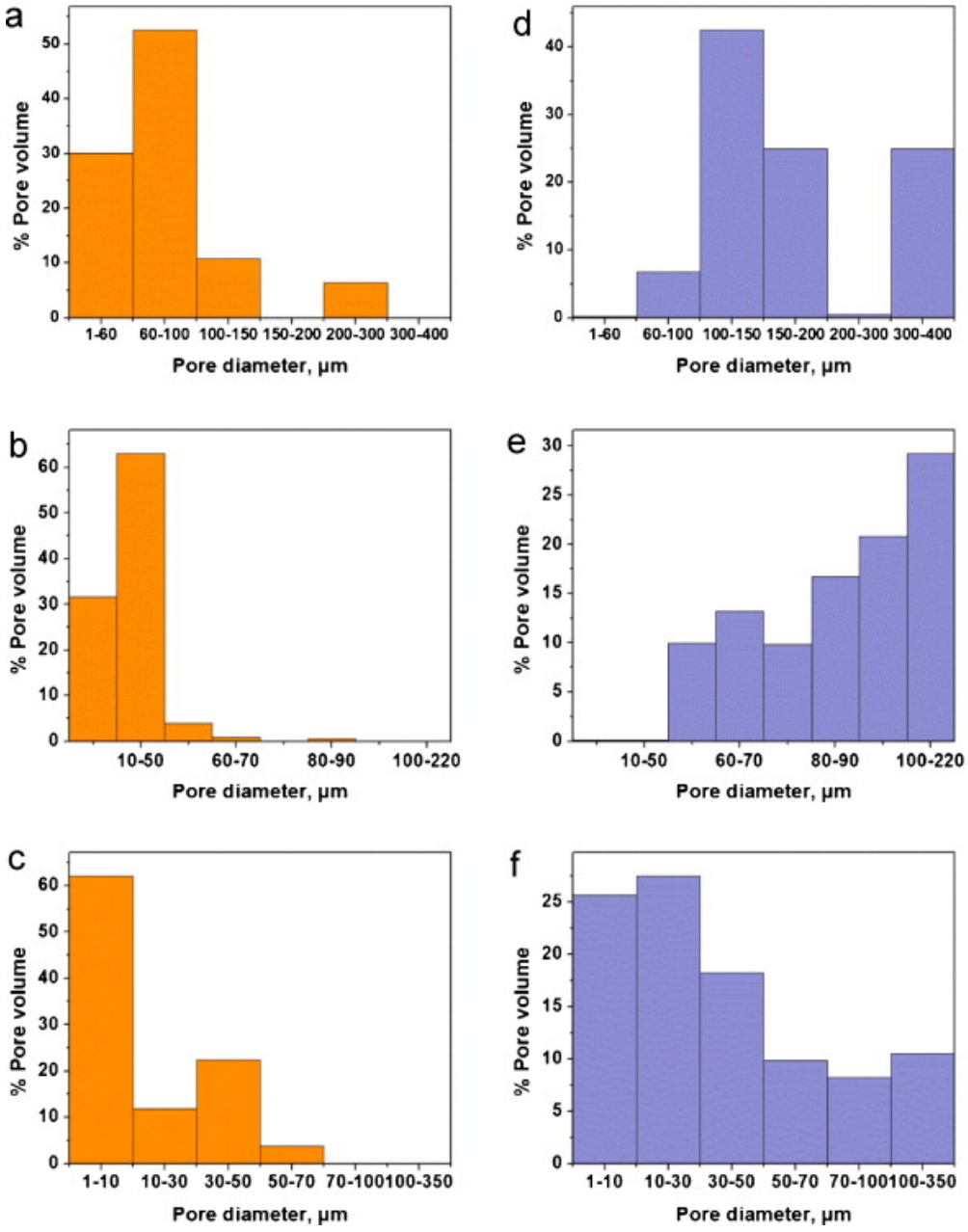

Figure 4.2 - Pore diameter histograms of PET nonwovens. a) Cooltexx; b) FO2425N/30; and c) 16-1 from extrusion porosimetry and d-f are the corresponding histograms from intrusion porosimetry.

Table 4.1 – Summary of porometry, porosimetry and tomography results. Porosimetry, Model, and XCT results indicate porosity as a percentage of total volume.

Sample	SEM images	Porometry		Porosimetry		Model	XCT
	Avg. fiber size (µm)	Bubble point diameter (µm)	Avg. pore size (µm)	LEP	MIP	From eq.(5)	
Cooltexx FO2425N/30	23.92±3.58	149.41	56.34	85±1.01	70±0.56	75.64	63
16-1	16.29±4.09	155.4	26.32	69±6.61	53±0.94	63.79	32
8% PAN	N/A	43.16	10.79	34±2.75	42±2.26	39.57	25
10% PAN	0.1363±0.0279	0.6168	0.3449	62±1.59	38±2.86	98.73	-*
12% PAN	0.1572±0.0214	0.7772	0.4479	67±2.38	54±2.72	98.55	-*
	0.3623±0.0447	2.1646	1.2830	87±2.23	62±2.85	98.19	-*

*Tests were not carried out due to limited resolution of the instrument.

Comparison between the histograms in Figures 4.2a-c and Figures 4.2d-f showed that LEP could detect the finer pores in the nonwoven in addition to some of the bigger pores and this consequently led to the technique reporting higher porosities than MIP. The histograms, and the calculated porosity, seemed to contradict an intuitive understanding that bigger pores contribute more to the pore volume than smaller pores. However, it is possible that there were more small pores than there were large pores and also that the high surface tension of mercury did not allow it to capture all of the pore volume, especially in finer pores. Galwick, with a surface tension $1/30^{th}$ that of mercury, was better able to access these smaller pores. Furthermore, mercury tends to intrude pores in the shape of a capillary with a well-defined meniscus at both ends [21]. Such flow geometry would restrict "wetting out" of the entire pore volume present. These high pressures in MIP likely distort the pore structure and compress the soft nonwoven.

The 16-1, however, exhibited a higher measured porosity with intrusion porosimetry. The material appears to be calendered, possibly rendering it more resistant to compaction. Moreover, the observed "melting" of the fibers together and the general lack of a homogeneous fiber structure may result in blind pores being present. Blind pores are detected by intrusion but not by the extrusion technique resulting in a higher measured porosity for MIP. Furthermore, it was found that MIP was able to detect some large pores that were not detected by LEP. This was due to initial stabilization of the liquid level in the sample chamber of the extrusion porosimeter that caused artificially high extruded volumes to be measured. These experimental artifacts prevented the accurate measurement of pore diameter for the larger pores (over 50-100 μm). The extrusion technique was found to be more accurate in evaluating the pore volume of finer pores in the nonwovens while intrusion detected the larger pores. A combined analysis of the data from the two techniques would give a more complete depiction of the nonwoven by presenting the entire pore size range, but more study would be necessary to deconvolute the results from each technique without "double counting" measured pore volume.

4.3.1.2 Electrospun nanofibers

SEM images of the electrospun nanofibers in Figure 4.3 show that increase in concentration of the polymer solution results in an increased fiber size. Average fiber diameters calculated from measurements using ImageJ are shown in Table 4.1. For any given unit area on the image, it can be seen that the number of fibers in the field of view decreased with fiber size and this corresponded to an increase in the pore volume in that region [22].

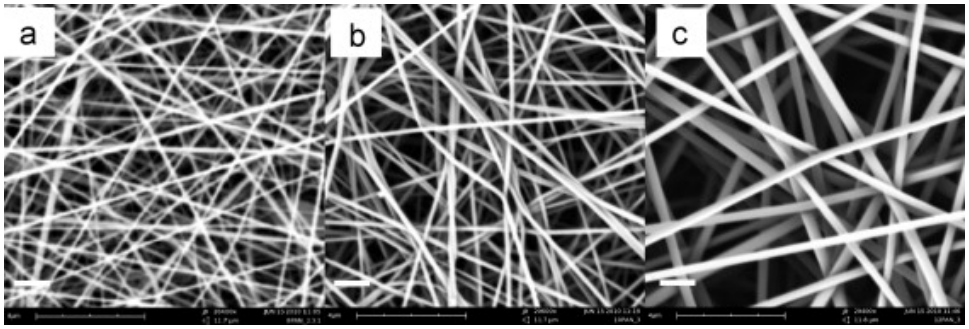

Figure 4.3 - SEM images of a) 8%; b) 10%; and c) 12% PAN at 20400, 20600 and 20400X magnification, respectively, showing the increase in fiber diameter and pore size with increase in concentration of solution spun. Scale bar on image represents a length of 1µm.

As with the PET nonwovens, the porosities of the electrospun materials measured by MIP were lower than those measured by LEP. Figure 4.4(a), (b) and (c) show the pore diameter histograms from LEP for 8, 10 and 12% PAN and 4.4(d), (e) and (f) are the corresponding graphs for MIP. Despite the fact that the porosities obtained from MIP and LEP exhibited a trend of increasing porosity with increase in fiber size, the pore diameter distributions were not found to definitively represent this pattern in Figures 4.4a-f. Slightly larger pore diameters were shown to be detected in the histograms in Figures 4.4b and 4.4c (LEP) and in Figures 4.4e and 4.4f (MIP) for 10% and 12% PAN. It is possible that the shifts in pore diameter were too subtle to be detected by porosimetry.

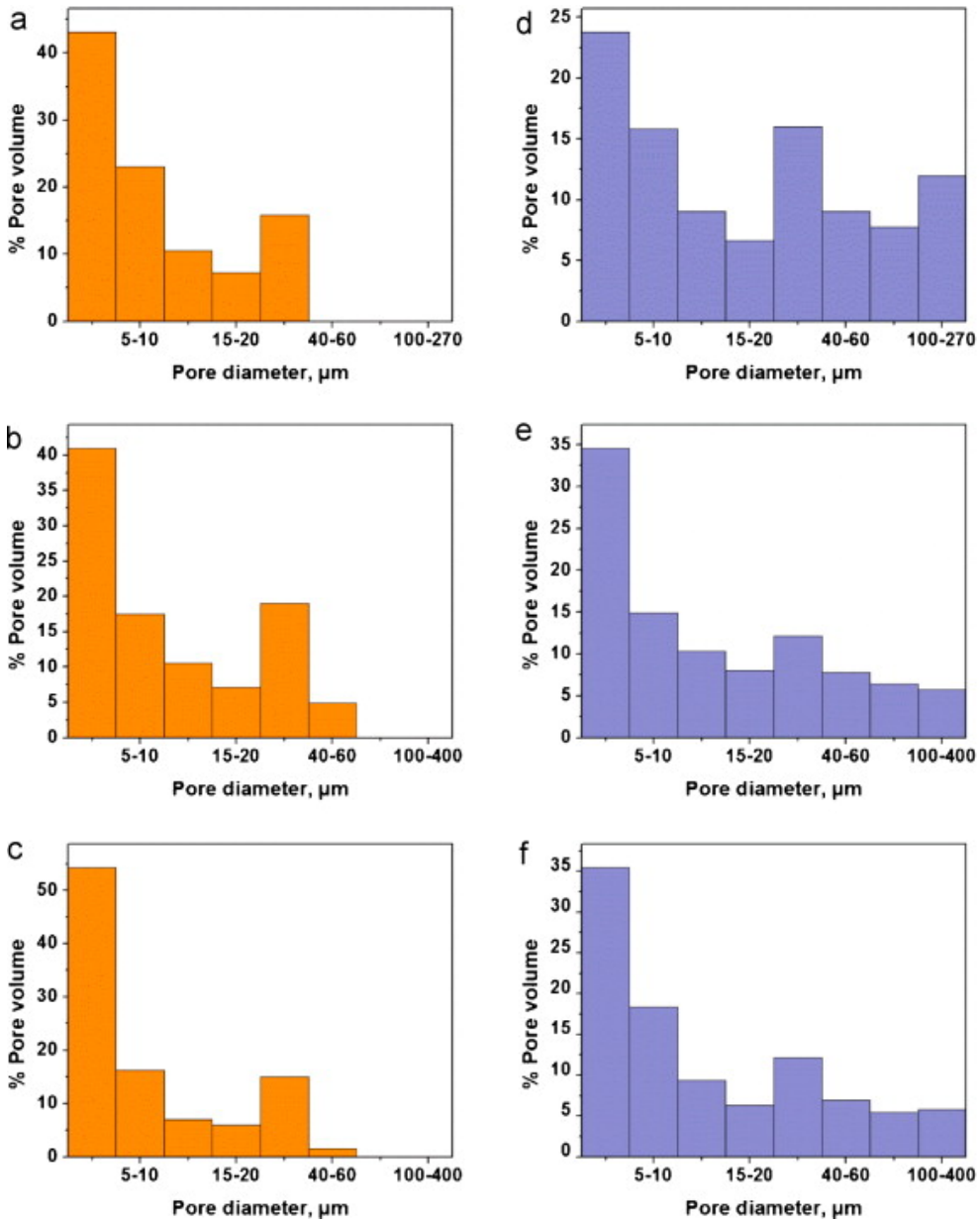

Figure 4.4 - Pore diameter histograms of electrospun PAN nanofibers. a) 8%; b) 10%; and c) 12% PAN from extrusion porosimetry and d-f are the corresponding histograms for the intrusion porosimetry.

Table 4.1 shows the comparison of porosity values obtained from MIP and LEP for the electrospun nonwovens. Also included are the calculated porosities using Equation (4). It can be seen that the two sets of values compare reasonably well for the polyester nonwovens but in the case of electrospun mats, the use of simplified formulae results in unreliably high porosity

values. Earlier investigations have assumed that the spun fiber density is the same as that of the bulk polymer [23, 24] and likewise obtained abnormally high porosity values. It was found that for polyurethane, the polymer density in the electrospun form was a third of that in the bulk form [25]. Such a large decrease in polymer density can lead to high estimated porosities when using eq. (4). It is also worth noting that with the use of Equation (4) no significant change in porosity was observed with a change in fiber size for the electrospun mats.

4.3.2 Capillary flow porometry

Figure 4.5 shows the constricted pore size distributions of the PET nonwovens from the porometry analyses. A decrease in the pore throat diameter was observed for a decrease in the fiber size, Cooltexx exhibited an average pore throat diameter of 56.34 μm whereas the corresponding value for 16-1 was 10.79 μm. The pore size values obtained from porometry measurements of the nonwovens are summarized in Table 4.1 and the fiber sizes are presented for comparison.

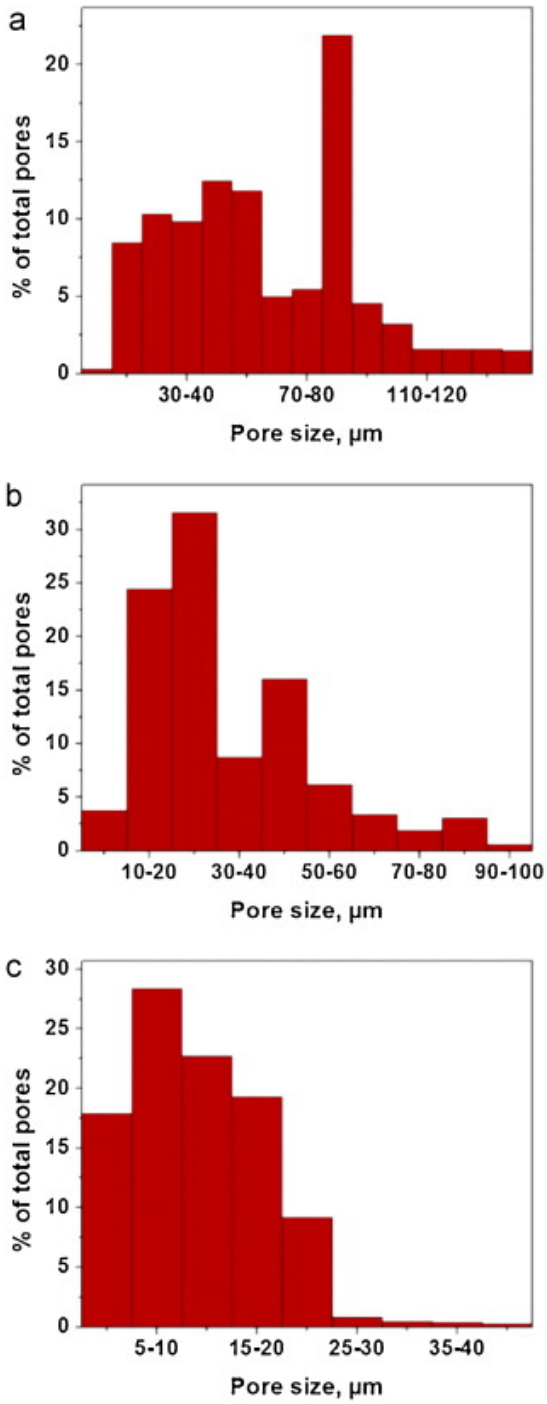

Figure 4.5 - Distribution of pore throat diameters of PET nonwovens from capillary flow porometry. a) Cooltexx; b) F02425N/30; and c) 16-1.

Figure 4.6 shows the pore size distributions of the electrospun nanofibers. The average pore size increased with increase in fiber size and seemed to follow a proportional relationship

with fiber size. Comparing the porosimetry and porometry results we see that both pore diameter and pore size increase with fiber size. These findings are in agreement with a previsions investigation by Tsai [26] who proposed a proportional relationship between fiber size and pore size. Our data also indicate that the combined increase in constricted pore size and pore diameter may contribute to an increase in porosity for these classes of nonwovens.

Furthermore, the narrow distributions from porometry indicate excellent fiber uniformity. If fiber diameters varied, constricted pore size would likewise be broad in their distribution. Narrow constricted pore size distributions coupled with a high permeability (due to high porosity and inherent low tortuosity) make electrospun nonwovens excellent candidates for use in filtration applications for capturing particles of narrow size ranges.

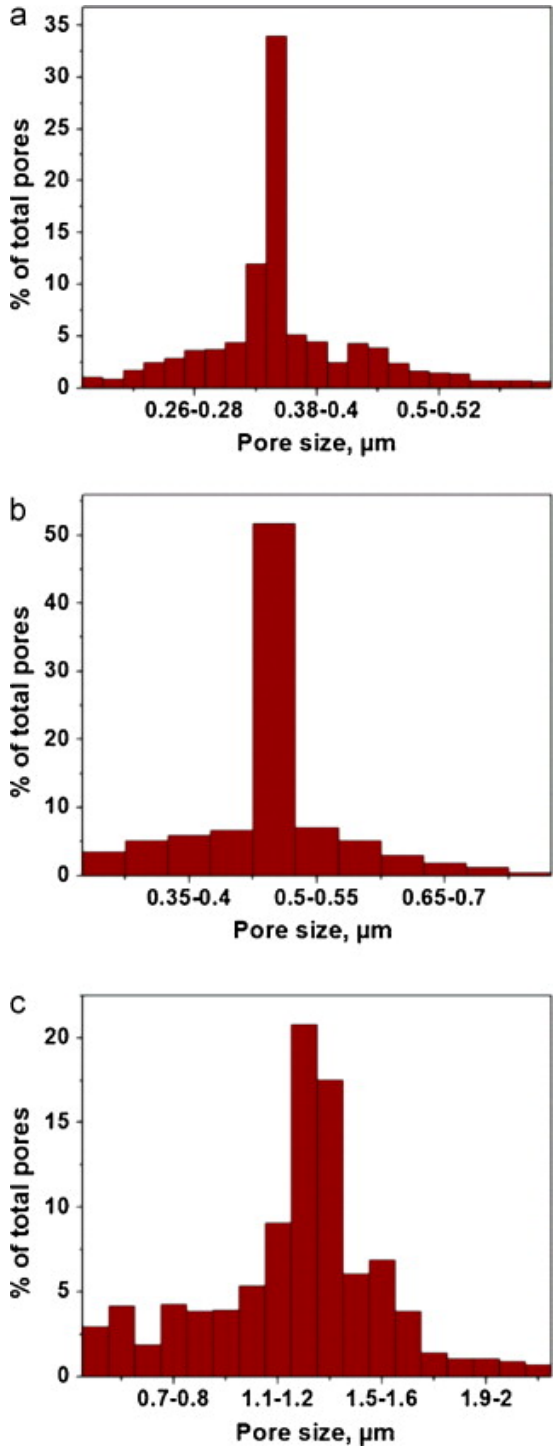

Figure 4.6 - Distribution of pore throat diameters of electrospun PAN nanofibers from capillary flow porometry. a) 8%; b) 10%; and c) 12% PAN.

4.3.3 X-Ray Computed Tomography (XCT)

XCT is an imaging technique that offers a unique, non-destructive option for 3-D characterization of porous materials. However, the instrumentation used for this approach had a resolution of 1-3 μm, which prevented the characterization of the nanofiber nonwovens. As a result, the use of this technique has been limited to the PET nonwovens because of their larger feature sizes. Figure 4.7(a-c) shows the 3-D images of the PET nonwovens obtained from XCT. Average fiber sizes were obtained from the Cooltexx and FO2425N/30 XCT images for comparison to the estimates from SEM images. The values were found to be (corresponding SEM estimates in brackets): 36.5±7.95 μm (23.92±3.58 μm) and 14.39±3.69 μm (16.29±4.09 μm) for Cooltexx and FO2425N/30 respectively. Porosity of each sample was calculated with subsequent image processing. The results are given in Table 4.1. When compared to the intrusion and extrusion techniques, the results were most similar with the Cooltexx. However, XCT produced different porosity measurements for the 16-1 and FO2425N/30. The difference in porosity measurements using the imaging and analytical techniques can be explained in part by the heterogeneity of the nonwoven structure. The 3-D images indicate some regions of high fiber density and other areas of high porosity. Samples for XCT need to be small in order to minimize sample motion during imaging (typical size of the nonwoven used for imaging is about 1 cm x 0.5 cm). A small viewing area may not have been representative of the bulk nonwoven. The 16-1 also has tightly packed fibers which make resolving the pores in between fibers difficult. The lack of definition does not allow for a clear thresholding of the image and likely results in a poor estimation of porosity. A larger field of view might help obtain a fair representation for heterogeneous samples but this comes at the cost of reduced resolution (by using a lower magnification objective). Thus, in the application of XCT as a characterization tool a trade-off must be made between resolution desired and viewing area necessary to obtain a reasonable

representation. Further, by improving the contrast between fibers and pores during imaging, thresholding can be improved leading to more accurate estimations of the porosity. This may be accomplished by adding a contrasting agent, such as potassium iodide or osmium iodide, or by using higher resolution tomography. These approaches are beyond the scope of this study. By addressing the two issues discussed here XCT can be used as a potential tool for easy and convenient evaluations of the pore structure of nonwovens.

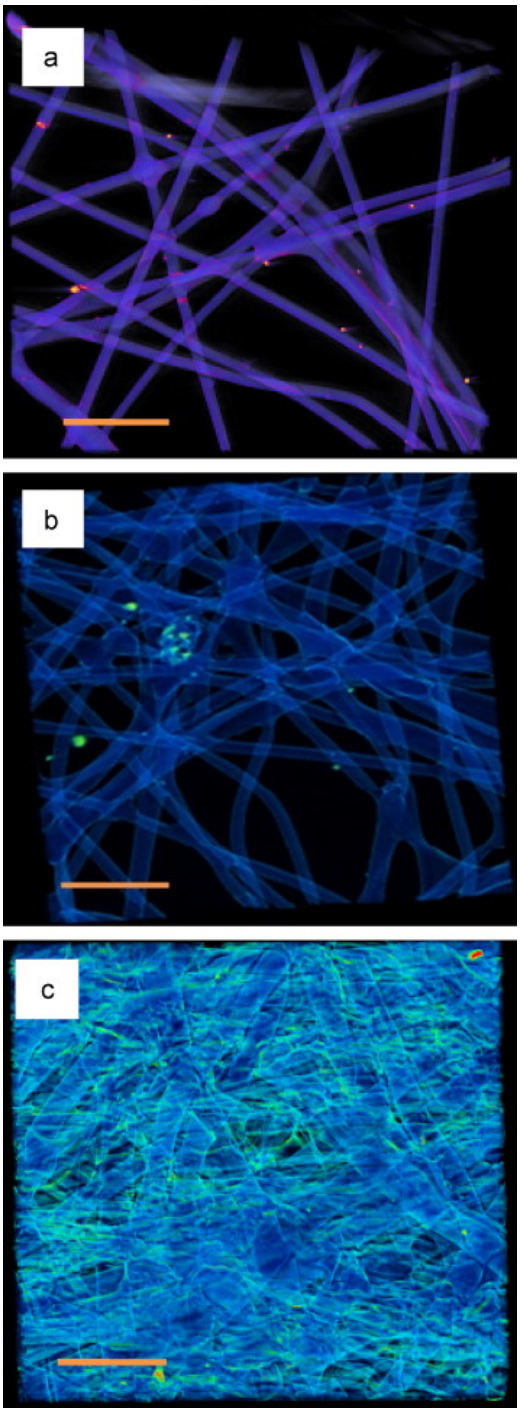

Figure 4.7 - 3-D x-ray computed tomography images of PET nonwovens. Field of view is indicated within brackets. a) Cooltexx (450x465 µm); b) FO2425N/30 (450x465 µm); and c) 16-1 (490x460 µm). The scale bar on the images represents a length of 100 µm.

4.6. Conclusions

Accurate measurements of pore structure properties are essential for properly designing and choosing appropriate filters or membranes for a range of applications. This study has found that for both commercial polyester and electrospun nanofiber nonwovens, different measurement techniques result in a range of calculated porosities. Gravimetric analysis using simple volume and mass measurements can lead to inaccuracies if the actual density of the fiber material is not known. In general, low pressure extrusion techniques resulted in higher measured porosities than mercury intrusion due to the lower operating pressures and lesser compaction of the sample. This trend may not hold, however, for samples that contain blind pores, which are not detected through extrusion techniques. Imaging approaches like XCT could deviate from these analytical techniques due to difficulties in thresholding the images to clearly delineate where a fiber is and is not present. This problem can be exacerbated by low resolution of XCT. However, this work shows that XCT is a promising method for characterizing pore structure in porous soft materials and, for larger feature sizes, can have superior utility when compared to the 2-D images gathered with SEM.

Characterization of electrospun materials yielded very interesting results. While XCT could not image nano-scale fibers due to limitations in resolution, porosimetry and porometry analysis indicated that while electrospun materials exhibited similar or slightly higher porosities than the PET nonwovens evaluated here, the throat diameters of their effective pores were up to an order of magnitude smaller due to a smaller fiber. These results demonstrate the promise of electrospun materials as high permeability yet selective filtration materials. As these and other emerging filtration media become available, accurate characterization methods will be needed to assess their properties.

References

1. Hutten, I.M., Handbook of non-woven filter media. First ed. ed. 2007: Butterworth-Heinemann.

2. Barhate, R.S., C.K. Loong, and S. Ramakrishna, Preparation and characterization of nanofibrous filtering media. Journal of Membrane Science, 2006. 283(1-2): p. 209-218.

3. Barhate, R.S. and S. Ramakrishna, Nanofibrous filtering media: Filtration problems and solutions from tiny materials. Journal of Membrane Science, 2007. 296(1-2): p. 1-8.

4. Qin, X.-H. and S.-Y. Wang, Filtration properties of electrospinning nanofibers. Journal of Applied Polymer Science, 2006. 102(2): p. 1285-1290.

5. Subbiah, T., G.S. Bhat, R.W. Tock, S. Parameswaran, and S.S. Ramkumar, Electrospinning of nanofibers. Journal of Applied Polymer Science, 2005. 96(2): p. 557-569.

6. Yoon, K., B.S. Hsiao, and B. Chu, Functional nanofibers for environmental applications. Journal of Materials Chemistry, 2008. 18(44): p. 5326-5334.

7. Gopal, R., S. Kaur, Z. Ma, C. Chan, S. Ramakrishna, and T. Matsuura, Electrospun nanofibrous filtration membrane. Journal of Membrane Science, 2006. 281(1-2): p. 581-586.

8. Homonoff, E. Characterization And Effect Of Pore Size Distribution On The Filtration Performance Of Nonwoven Fibrous Webs. in Twelfth Technical Symposium. 1984. Washington DC.

9. Norman Lifshutz, U.R. A comparison of liquid filtration performance with mean flow pore diameter. in INTC 2005 International Nonwovens Technical Conference: Joint INDA-TAPPI Conference. 2005.

10. Li, D., M.W. Frey, and Y.L. Joo, Characterization of nanofibrous membranes with capillary flow porometry. Journal of Membrane Science, 2006. 286(1-2): p. 104-114.

11. Andrade, J.S., U.M.S. Costa, M.P. Almeida, H.A. Makse, and H.E. Stanley, Inertial Effects on Fluid Flow through Disordered Porous Media. Physical Review Letters, 1999. 82(26): p. 5249.

12. Han, S.O., W.K. Son, J.H. Youk, T.S. Lee, and W.H. Park, Ultrafine porous fibers electrospun from cellulose triacetate. Materials Letters, 2005. 59(24-25): p. 2998-3001.

13. Akshaya Jena, K.G., Characterization of Pore Structure of Filtration Media. Fluid Particle Separation Journal, 2002. 4(3): p. 227-241.

14. Patanaik, A., V. Jacobs, and R.D. Anandjiwala, Performance evaluation of electrospun nanofibrous membrane. Journal of Membrane Science. 352(1-2): p. 136-142.

15. Meneghello, G., D.J. Parker, B.J. Ainsworth, S.P. Perera, J.B. Chaudhuri, M.J. Ellis, and P.A. De Bank, Fabrication and characterization of poly(lactic-co-glycolic acid)/polyvinyl alcohol

blended hollow fibre membranes for tissue engineering applications. Journal of Membrane Science, 2009. 344(1-2): p. 55-61.

16. S. H. Lau, W.K.S.C., Fernando Garzon, Hauyee Chang, Andrei and M.F. Tkachuk, Wenbing Yun, Non invasive, multiscale 3D X-Ray characterization of porous functional composites and membranes, with resolution from MM to sub 50 NM. Journal of Physics: Conference Series, 2009. 152(1): p. 012059.

17. Available at http://pmiapp.com/products/docs/lep_brochure.pdf.

18. Akshaya Jena, K.G., Liquid Extrusion Techniques For Pore Structure Evaluation Of Nonwovens International Nonwovens Journal, 2003: p. 45-53.

19. PoreMaster brochure, Quantachrome Instruments.

20. Chen, S., H. Hou, F. Harnisch, S.A. Patil, A.A. Carmona-Martinez, S. Agarwal, Y. Zhang, S. Sinha-Ray, A.L. Yarin, A. Greiner, and U. Schroder, Electrospun and solution blown three-dimensional carbon fiber nonwovens for application as electrodes in microbial fuel cells. Energy & Environmental Science. 4(4): p. 1417-1421.

21. Giesche, H., Mercury Porosimetry: A General (Practical) Overview. Particle & Particle Systems Characterization, 2006. 23(1): p. 9-19.

22. Pedicini, A. and R.J. Farris, Mechanical behavior of electrospun polyurethane. Polymer, 2003. 44(22): p. 6857-6862.

23. Tsai, P.P., Characterization of Melt Blown Web Properties Using Air Flow Technique.International Nonwovens Journal, 1999: p. 36-40.

Chapter 5.

Structural Characterization of Thin Film Composite Membranes

5.1. Introduction

Engineered osmosis (EO) is an emerging technology platform comprising of a number of membrane-based technologies. These include forward osmosis (FO), pressure-retarded osmosis (PRO) and direct osmotic concentration, which can be used for desalination, power production and dewatering, respectively. These technologies rely on osmotic gradients between a concentrated draw solution and a relatively dilute feed solution. In EO, water flux performance is critical and is dependent on the osmotic pressure gradient over the selective layer of the membrane. The membrane support layer however, poses a resistance to draw (in FO) and feed (in PRO) solute mass transport that can dramatically reduce this driving force. This phenomenon is known widely as internal concentration polarization (ICP) and is largely responsible for preventing the use of existing commercial reverse osmosis (RO) membranes in EO processes.

Most EO membrane developers have focused on optimizing the support layer characteristics in order to reduce the severity of ICP. The structural parameter, S, has been widely used as a metric to assess the membrane's contribution to ICP. S is defined as

$$S = \frac{t\tau}{\varepsilon} \qquad (1)$$

where t is the thickness, τ is the tortuosity, and ε is the porosity. These individual characteristics can be manipulated in order to minimize the value of S, which is goal of many membrane development teams in the industrial and academic environments. However, when making a new membrane, the exact value of some of these characteristics, and by association the value of S, is unknown. So far, S has only been indirectly calculated using models based on

experimental flux measurements and an assumption of film theory dictating mass transfer. One such model is shown below:

$$S = \frac{D}{J_w}(\ln \frac{B + A\pi_{D,b}}{B + J_w + A\pi_{F,m}}) \qquad (2)$$

Where D is the solute diffusivity, J_w is the water flux, A is the pure water permeability coefficient of the membrane, B is the solute permeability coefficient of the membrane, $\pi_{D,b}$ is the osmotic pressure of the bulk draw solution and $\pi_{F,m}$ is the osmotic pressure of the feed solution at the membrane interface. It is explicitly clear that the above parameters do not define the membrane structure and that changes in these values should not influence the support structure. However, investigators still use this model as a means of calculating S from osmotic flux measurements [16].

Recently, a method was proposed to standardize FO membrane testing. This investigation found that even when the same conditions were used amongst a number of research groups, S values could still vary when using this fitted parameter technique [27]. One must note that the models used to calculate S are constantly evolving in the literature in order to distinguish the different resistances to mass transport in the system and uniquely identify the resistance offered by the membrane structure itself. Many of these studies still rely on assumptions that are likely inaccurate. One such assumption is that *external* concentration polarization on the support layer side of the membrane is negligible. Most models fail to account for this phenomenon, effectively lumping any external CP into the S parameter calculation. For poorly performing membranes, fluxes are low enough that this assumption is a reasonable approximation. However, with the advent of high performance EO membranes at both the laboratory and commercial scale, the resulting high fluxes mean that external CP can no longer be ignored [28].

Existing models that continue to combine external and internal CP will overestimate S values as the fitted parameter of the equation. This results in an unreliable calculation of the structural parameter and an overestimation of the membrane's contribution to mass transfer resistance. If such a parameter could be calculated directly, rather than as a fitted parameter of a model, we would be able to better understand exactly how membrane structure plays a role in osmotic flux performance. However, few techniques are available to accurately characterize the structural characteristics of membranes, such as porosity and tortuosity.

A review of the methods used to calculate porosity and pore diameter distribution in soft nonwovens has been presented in a previous publication by the author and co-workers [29]. Models are available that relate tortuosity to porosity and pore architecture, negating the need to directly measure the tortuosity [30-32]. However, these models are empirical and can only be applied to specific isotropic structures. No models are available for asymmetric or composite structures, which include many of today's TFC membrane supports. Average tortuosity can be measured through conductivity and diffusivity measurements of a dissolved solute through the porous material [33-35], but such efforts are complicated, difficult to reproduce, and have limited value in characterizing asymmetric composite structures. At the time of this writing, the only study on pore structure characterization of EO membranes is on microscopic characterization [36]. The techniques used include scanning electron microscopy (SEM), transmission electron microscopy (TEM) and confocal laser scanning microscopy (CLSM). While this study provides some interesting insights on the structure of the particular membrane studied, the accuracy of using 2D imaging techniques (SEM, TEM) to characterize asymmetric pore structures is debatable. Also, the two electron microscopy techniques were used to image the membrane in the dehydrated state and then comparisons were made to CLSM images of the wetted membrane.

The membrane studied was made of cellulose acetate, a hydrophilic polymer, which likely exhibits swelling when hydrated. In general, techniques should be chosen carefully so that the sample preparation does not significantly alter or damage the structure being analyzed.

The objective of this study is to evaluate tools for characterizing the 3D structure of commercially available TFC reverse osmosis (RO) membrane support layers. These membranes were chosen since they possess a composite and anisotropic structure typical of many TFC membranes today [37, 38]. The membranes tested in this study have also been previously evaluated for their performances in FO [39]. TFC membranes are now finding broader application in EO, with Oasys Water™ and Hydration Technology Innovations™ both releasing their own commercially available versions in 2012 [40, 41]. Two characterization techniques have been used as a part of this study – an analytical method, mercury intrusion porosimetry (MIP) and an imaging technique, x-ray microscopy (XRM). MIP is a widely used tool in the analysis of porous materials [29]. XRM is a non-destructive 3D imaging technique that is widely used in biomedical, geological and archaeological applications. Recently, with the advent of improved phase contrast optics it has been increasingly used to image soft materials [42]. The results from the two approaches were used to evaluate the membrane structures and calculate the intrinsic structural parameters. These values were then compared to values obtained from the conventional method of using an empirical model. The comparison demonstrates the inaccuracy of empirical approaches and the need for better understanding of mass transport occurring during osmosis across anisotropic and composite membranes.

5.2. Materials and methods

5.2.1 Materials

The membranes used in this study were the BW30 and SW30-XLE thin film composite reverse osmosis membranes from Dow Water & Process Solutions™. These membranes were used as-received and characterized in their dry state.

5.2.2 Methods

5.2.2.1 Analytical characterization

Mercury intrusion porosimetry (MIP) was used to characterize porosity and tortuosity of these membranes in their dry state. The porosimeter used was a PoreMaster from Quantachrome Corporation. In addition to pore diameter distribution and porosity, tortuosity of the pore structure was calculated using a generalized correlation [43, 44].

$$\tau = (2.23 - 1.13 V_{tot} \rho_b)(0.92(\frac{4}{S}\sum \frac{\Delta V_i}{d_i})^{1+\varepsilon}) \quad (4)$$

where τ is the tortuosity factor, V_{tot} is total pore volume (cm^3/g), ρ_b is bulk density of sample (g/cm^3), S is the Brunauer-Emmett-Teller (BET) surface area (m^2/g) , ΔV_i is change in pore volume within a pore size interval (cm^3), d_i is average diameter within a pore size interval (cm),and ε is pore shape exponent. A value of ε = 2.1 was assigned for both membranes in accordance with a previous study [43].

Triplicate porosimetry experiments were performed for each membrane to obtain average porosities and tortuosities. The experiment was set up so that the instrument only measured pores down to 1 μm (which is the maximum resolution of the Xradia MicroXRM) in order to enable a fair comparison. The thicknesses of the two membranes were determined using a micrometer. Ten measurements were taken to obtain an average thickness.

5.2.2.2 Imaging characterization

Both scanning electron microscopy (SEM) and x-ray microscopy (XRM) were used to image the two membranes used in this study. A JEOL 6335F field emission SEM was used to obtain cross-sectional images of the two membranes. The membranes were fractured along orthogonal axes. One cross section represents the membrane in the direction in which the cast polysulfone (PSu) support was introduced into the precipitation bath. The second was the direction orthogonal to that of the previous one. In order to allow for ease of freeze-fracturing, the nonwoven backing layer was removed from both membranes and only the PSu support layers were imaged.

Two XRM instruments were used in this study for a multi-length scale approach. The XradiaMicroXRM-400 provided resolution to ~1 μm, while the Xradia UltraXRM-L200 extended this resolution to 50 nm. On the MicroXRM, a 40X objective was used to obtain 4000 projection radiographs at equally-spaced intervals over a 180° sample rotation, exposing each radiograph for 10 seconds. The x-ray power was set at 20 kV and 0.1 mA. In the case of the UltraXRM, 721 projection radiographs were collected over a 180° rotation range using a 64 nm pixel size and Zernike phase contrast imaging mode, exposing each radiograph for 75 seconds [45]. The x-ray power was set at 40 kV and 30 mA. The reconstructed images from both instruments were exported to Avizo™Fire (Visualization Sciences Group) for further image processing and analysis. The images were first filtered to remove background noise and thresholded to binarize the images into pore space and polymer matrix. The porosity was analyzed using 'volume3d', a built-in measurement tool that is used to compute the density of pixels above a certain intensity threshold. Porosity distribution as a function of thickness of the membrane was determined by making this measurement at each slice. Tortuosity was measured

using an algorithm described in a previous study [46]. The algorithm quantifies tortuosity by tracking the center of mass of each pore as it goes from one end of the sample surface to the other end. The total length of this path is then divided by the Euclidian distance of the entire sample. Two membrane samples were imaged in the MicroXRM in order to obtain average porosities and tortuosities. The cross-sections obtained from XRM were exported to ImageJ (National Institutes of Health) to measure their thicknesses. Ten measurements were taken to obtain an average thickness.

5.2.2.3 Calculation of Structural Parameter

The structural parameter was measured in osmotic membranes using experimental osmotic flux measurements. Details of the osmotic flux tests can be found elsewhere [39].

5.3. Results and discussion

5.3.1 Scanning Electron Microscopy (SEM)

Figure 5.1 shows cross-section SEM images of the BW30 (5.1a and b) and SW30-XLE (5.1c and d). Figures 5.1a and c correspond to samples freeze-fractured perpendicular to the direction in which the cast polysulfone (PSu) support was introduced into the precipitation bath and in 5.1b and d, the samples were fractured along the direction orthogonal to that of 5.1a and c. The specific nature of the pore structure (e.g. sponge-like vs. finger-like) depends on the solvent system used [17] which is proprietary to membrane manufacturers. However, the elongation of the macrovoid structures, seen in Figures 5.1b and d, was likely caused by the precipitation of the film as it was introduced to the bath at an angle. A skin layer quickly forms, causing a “no slip” condition and shear within the still liquid but forming a porous support layer. The macrovoids are “stretched” in the direction of the moving film as they form.

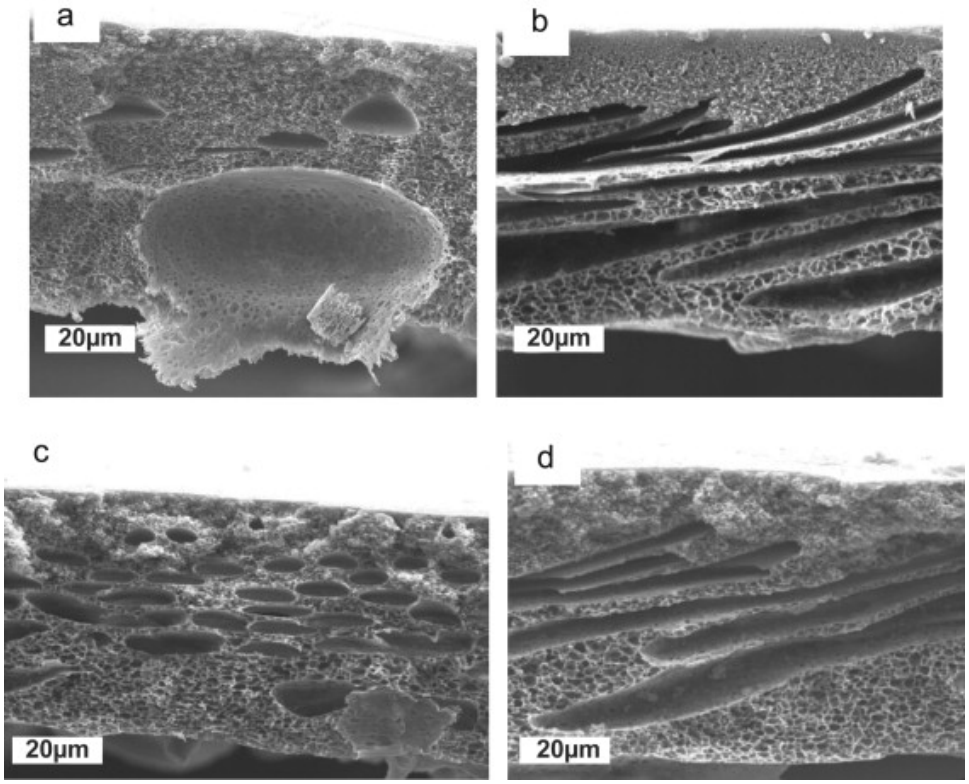

Fig. 5.1. FE-SEM images of the cross-sections of (a and b) BW30 and (c and d) SW30-XLE. Samples were prepared for imaging by freeze-fracturing in liquid nitrogen along two different axial directions. 5.1a and c correspond to samples freeze-fractured perpendicular to the direction in which the cast polysulfone membrane was introduced into the precipitation bath. 5.1b and d correspond to samples freeze-fractured in the direction orthogonal to that of 5.1a and c.

While these SEM images clearly show the anisotropy in the pore structure throughout the depth of the membrane they also point out the shortcomings of such a 2D imaging technique. A single SEM image cannot provide a complete representation of the anisotropic structure. When comparing figures 5.1a and 5.1c (similarly 5.1b and 5.1d) it can be seen that the macrovoid density is higher for SW30-XLE in the former set of images but slightly higher for BW30 in the latter set. Non-uniformity in multiple dimensions makes 2D imaging less useful and necessitates the use of an analytical or imaging technique that captures the 3D structure.

5.3.2 Mercury Intrusion Porosimetry (MIP)

Figure 5.2 shows the pore diameter distributions of the two membranes as gathered from MIP. The percent contribution to porosity from smaller pores (1 – 10 μm) was greater for the BW30 than SW30-XLE. In other words, BW30 has more smaller pores than the SW30-XLE. However, if the entry to a pore is smaller than its bulk size then this technique exhibits a bias towards the smaller pore sizes. This effect is termed as the ink-bottle effect and causes histograms to artificially shift to the left (toward smaller pores). It can also be seen that the large pores contributed greatly to the overall porosity. The effect was more noticeable in the SW30-XLE membrane which, by SEM images, showed some evidence of having more macrovoids. The structural metrics obtained from MIP are given in Table 5.1 and these were used to calculate the structural parameters shown in Table 5.2. The propagated uncertainties based on the individual parameters have not been included in the structural parameters since they were found to be too small (less than 1/100's). The inherent limitations of this technique, such as the ink-bottle effect and possible pore structure compaction can be avoided in a non-destructive 3D characterization method, such as imaging using a MicroXRM.

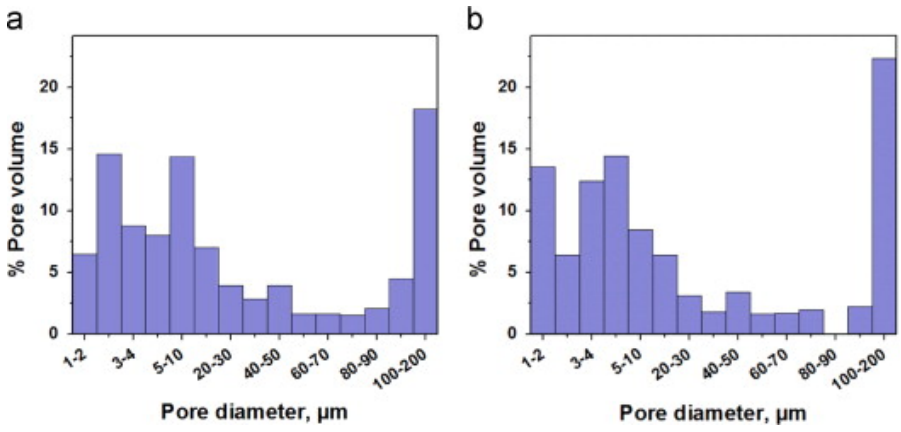

Fig. 5.2. Pore diameter histograms of (a) BW30 and (b) SW30-XLE from mercury intrusion porosimetry. The average porosities are 26.63±4.06 and 36.20±5.51% respectively (n=3).

Table 5.1. Porosity, tortuosity and thickness estimates for BW30 and SW30-XLE from analytical porosimetry and XRM imaging techniques. n=3 and 2 for porosity and tortuosity measurements

obtained from analytical and imaging techniques, respectively. n=10 for both thickness measurements.

	Analytical (MIP)			Imaging (MicroXRM)		
	Porosity, ε %	Tortuosity, τ	Thickness*, t μm	Porosity, ε %	Tortuosity, τ	Thickness, t μm
BW30	26.63±4.06	1.120±0.013	148.3±6.3	34.91±1.94	1.216±0.046	142.0±1.9
SW30-XLE	36.20±5.51	1.634±0.006	151.7±2.5	43.49±1.22	1.315±0.164	148.7±3.0

* This measurement was made using a micrometer.

Table 5.2.Estimates of structural parameter, S (in µm) from analytical, imaging and experimental flux measurements. The S value was obtained as a fitted parameter from experimental osmotic flux measurements.

S, µm	Analytical (MIP)	Imaging (MicroXRM)	From osmotic flux measurements
BW30	624	489	15100
SW30-XLE	685	402	20800

5.3.3 Micro X-ray Microscopy (MicroXRM)

Figure 5.3 shows the surface renderings of the 3D MicroXRM images of the BW30 (5.3a) and SW30-XLE (5.3b). The polyamide (PA) layers in both membranes were not visible due to their small thickness (<100 nm) which was below the ~1 µm resolution of the instrument. The labels on the image indicate the PSu and PET backing layers. The structure is bi-continuous with the red regions indicating the polymer phase and the blue regions corresponding to the open pore structure. These images can be separated into pore structure phase and polymer matrix phase as indicated by the images on the right. From these images, porosity and tortuosity can be analyzed using the Avizo Fire software package. The porosities and tortuosities of the two membranes calculated from these images are shown in Table 5.1.

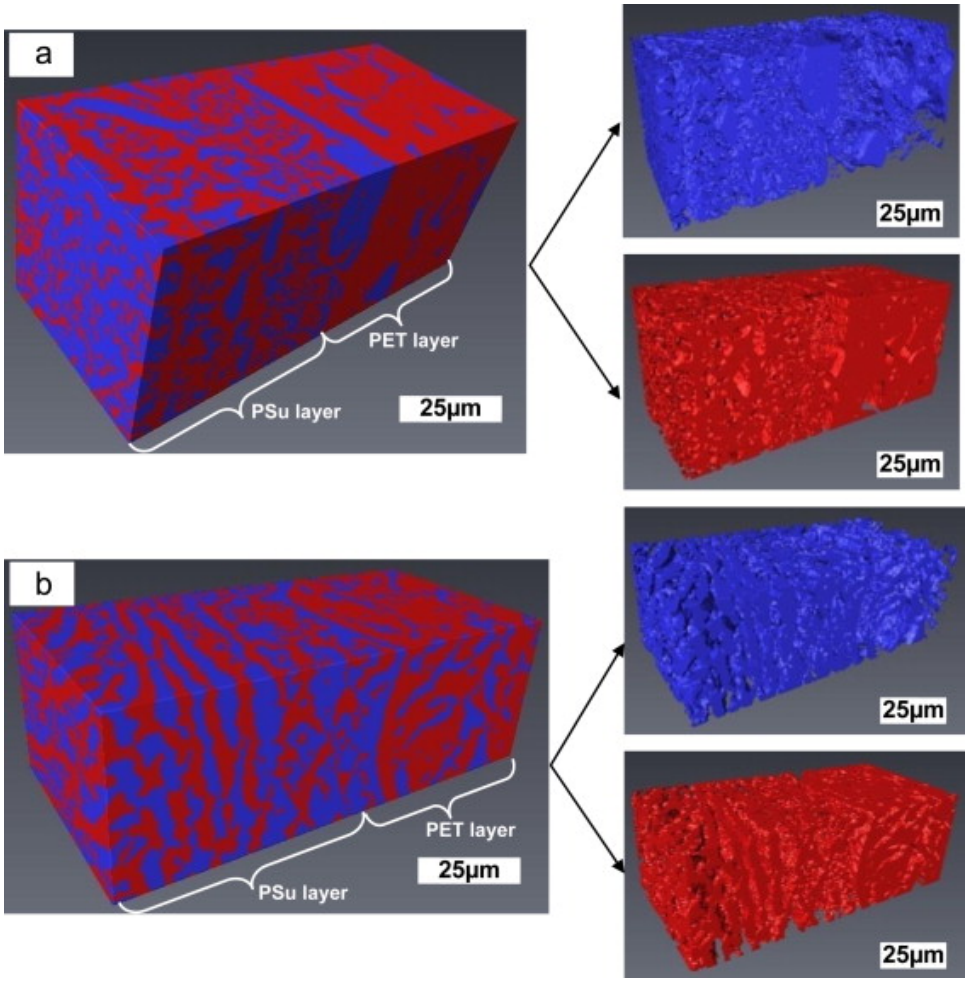

Fig. 5.3.Surface renderings, obtained using Avizo™Fire, of the 3D XRM images of (a) BW30 and (b) SW30-XLE. 5.3a and b show the complete structure of the membrane where blue regions denote pore space and red regions denote the polymer matrix. These images can be deconvoluted into pore phase only and polymer matrix only as shown by the images on the right.

Furthermore, the porosity can be studied as a function of depth. Figure 5.4 shows the porosity distribution as a function of membrane thickness for the BW30 and SW30-XLE. The resolution of the XRM images used for this analysis was ~0.6 µm. Porosities close to the surface of the membranes can be analyzed using these images, from which it was seen that the BW30 exhibits a higher "near surface" porosity than SW30-XLE. In both membranes, a sharp increase in porosity was seen at the interface between the PSu and PET layers. This is indicative of the

macrovoids that exist at the interface of the PSu and PET layers (see SEM images in Figure 5.1). XRM can also be used to examine the interface between the two layers.

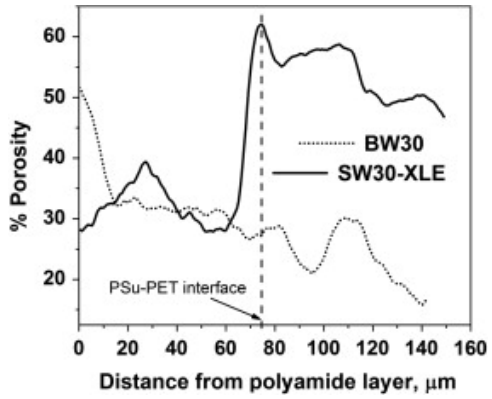

Fig. 5.4. Porosity distribution as a function of distance through the membrane. The distribution was obtained by using an in-built algorithm used to calculate the fraction of pore space (i.e. number of pore pixels) in each 2-D image constituting the 3D volumes shown in Figs. 5.3a and b. Distance at x=0 corresponds to the top of the polysulfone layer. The resolution of the MicroXRM images used for this analysis was ~0.6 μm.

As with MIP, the structural metrics obtained were used to calculate the structural parameter using the data gathered from the XRM. The S values obtained from XRM were found to be smaller than those from MIP. Both methods determine the same thicknesses, but the measured tortuosity and porosity values differ. In the case of tortuosity, MIP suggests a bigger difference in the tortuosities between BW30 and SW30-XLE than that suggested by XRM. It is to be noted that the value reported by MIP accounts for constriction of the pore diameter along with the increase in effective pore length whereas the algorithm used for XRM image analysis accounts only for the increase in effective pore length. It should be noted that the MIP experimental protocol was set to measure pores only down to 1 μm in order to match the resolution of the XRM. Secondly, the porosities calculated by XRM image analysis were higher than that from MIP. This was likely due to two reasons. First, high intrusion pressures compress the soft polymeric structure, lowering the overall pore volume and causing a negative bias in the

measurement [29]. Secondly, mercury intrudes pores in the shape of a capillary [47] and thus prevents the entire volume in a pore from being detected. XRM is a non-destructive technique that places no external stresses on the sample and thus could be used to obtain more accurate porosity estimates without compaction. A higher resolution XRM, such as the UltraXRM^{TM}, offers resolution down to 50nm, and may be used to further examine individual features of an asymmetric or heterogeneous structure with high precision. Figure 5.5 shows an image of both membranes taken with this instrument, from which the BW30 image captures the elongated macrovoids of the PSu midlayer and the SW30-XLE image captures a macrovoid feature. While these images can render the submicron size pores, they are not necessarily representative of the complete structure. Nevertheless, these images can be used to study the localized microstructure of heterogeneous pore structures and help understand transport at this level.

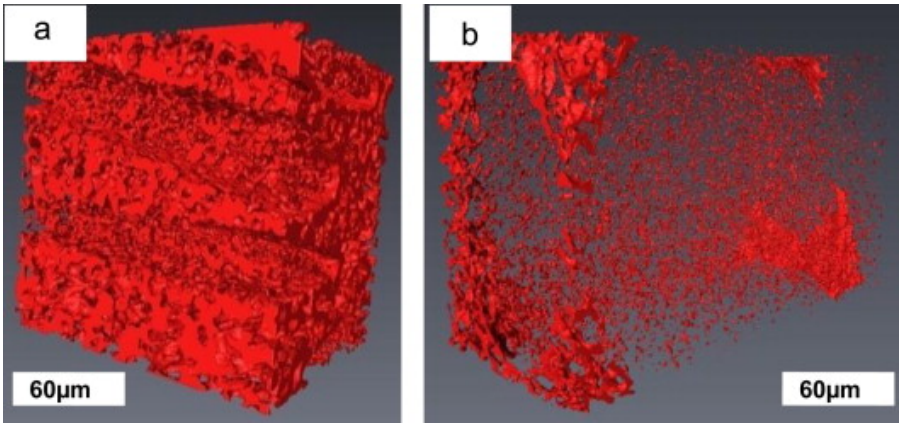

Fig. 5.5. 3D representations of the polysulfone matrix of (a) BW30 and (b) SW30-XLE from nano-scale XRM (Xradia UltraXRM). 5.5a shows the presence of long macrovoids in the matrix and 5.5b is the surface rendering of a single macrovoid showing the presence of pores along the macrovoid wall.

With regard to structural parameter, one other method has been used to measure its value in membranes like these. Since these membranes reject salts, osmotic flux tests combined with mass transfer analysis of boundary layer phenomenon can be used to calculate an effective

structural parameter using equation 2. This empirical approach has so far been the only means of estimating *S* in these materials and is only useable for osmotic membranes, thereby greatly limiting its utility. Structural parameters as measured by this method are given in Table 5.2. It is seen that measured *S* values are 1-2 orders of magnitude higher than the values calculated by XRM and MIP, mostly due to a myriad of mass transfer limitations of this technique. Poor wetting of a hydrophobic structure, hydrodynamic conditions, and even local mixing (or the absence of it) can impact these measurements, making them a poor representation of the true structural parameter.

5.4. Concluding remarks

Internal concentration polarization (ICP) is a major limitation towards realization of high fluxes and commercialization of engineered osmosis (EO) processes. The severity of ICP is greatly influenced by the structural parameter of the support layer. In this study, this parameter was measured for two commercial thin film composite reverse osmosis using analytical (mercury intrusion porosimetry (MIP)) and imaging (x-ray microscopy (XRM)) techniques. The structural parameter, which could be obtained from MIP and XRM, was found to differ substantially from that obtained using currently used techniques. XRM had the added advantage of being able to measure the porosity as a function of depth. In fact, this type of analysis may be useful as advanced mass transfer models are developed to predict diffusion in anisotropic structures. No membrane transport model has been developed to incorporate anisotropy into the structural parameter, primarily because such intrinsic structural information has until now been unavailable. The XRM technique can be used to assess the properties of such anisotropic materials and provide insight into the structure-property relationships in order to better design membranes for engineered osmosis.

References

1. Wong, M.C.Y., K. Martinez, G.Z. Ramon, and E. Hoek, *Impacts of operating conditions and solution chemistry on osmotic membrane structure and performance.* Desalination, 2012. **287**: p. 340-349.
2. Cath, T.Y., M. Elimelech, J.R. McCutcheon, R.L. McGinnis, A. Achilli, D. Anastasio, A.R. Brady, A.E. Childress, I.V. Farr, and N.T. Hancock, *Standard methodology for evaluating membrane performance in osmotically driven membrane processes.* Desalination, 2012. **312**: p. 31-38.
3. McCutcheon, J.R. and M. Elimelech, *Modeling water flux in forward osmosis: Implications for improved membrane design.* AIChE Journal, 2007. **53**(7): p. 1736-1744.
4. S Manickam, S. and J.R. McCutcheon, *Characterization of Polymeric Nonwovens Using Porosimetry, Porometry and X-ray Computed Tomography.* Journal of Membrane Science, 2012. **407-408**: p. 108-115.
5. Mauran, S., L. Rigaud, and O. Coudevylle, *Application of the Carman-Kozeny Correlation to a High Porosity and Anisotropic Consolidated Medium: The Compressed Expanded Natural Graphite.* Transport in Porous Media, 2001. **43**: p. 355-376.
6. Pisani, L., *Simple Expression for the Tortuosity of Porous Media.* Transport in Porous Media, 2011. **88**: p. 193-203.
7. Shen, L. and Z. Chen, *Critical Review of the Impact of Tortuosity on Diffusion.* Chemical engineering science, 2007. **62**: p. 3748-3755.
8. Labbez, C., P. Fievet, A. Szymczyk, C. Simon, A. Vidonne, A. Foissy, and J. Pagetti, *Hydraulic Resistance Measurements Combined with Electrical or Diffusional Resistance Measurements for Determination of Pore Size in MF Membranes.* Desalination, 2001. **141**: p. 291-299.
9. Maskell, W.C., *Tortuosity Factor in Non-Homogeneous Membranes.* Berichte der Bunsengesellschaft für physikalische Chemie, 1993. **97**: p. 680-683.
10. Tye, F.L., *Tortuosity.* Journal of Power Sources, 1983. **9**: p. 89-100.
11. Wang, Y.-N., J. Wei, Q. She, F. Pacheco, and C.Y. Tang, *Microscopic Characterization of FO/PRO Membranes - A Comparative Study of CLSM, TEM and SEM.* Environmental Science & Technology, 2012. **46**: p. 9995-10003.
12. Cath, T.Y., A.E. Childress, and M. Elimelech, *Forward Osmosis: Principles, Applications, and Recent Developments.* Journal of Membrane Science, 2006. **281**: p. 70-87.
13. Zhao, S., L. Zou, C.Y. Tang, and D. Mulcahy, *Recent developments in forward osmosis: Opportunities and challenges.* Journal of Membrane Science, 2012. **396**: p. 1-21.
14. Arena, J.T., B. McCloskey, B.D. Freeman, and J.R. McCutcheon, *Surface Modification of Thin Film Composite Membrane Support Layers With Polydopamine: Enabling Use of Reverse Osmosis Membranes in Pressure Retarded Osmosis.* Journal of Membrane Science, 2011. **375**: p. 55-62.
15. *Hydration Technology Innovations*. [cited; Available from: http://www.htiwater.com/.
16. McGinnis, R. and G. McGurgan, *FORWARD OSMOSIS MEMBRANES*. 2011, WO Patent WO/2011/028,541.
17. Lau, S.H., K.S.C. Wilson, G. Fernando, C. Hauyee, T. Andrei, F. Michael, and Y. Wenbing, *Non Invasive, Multiscale 3D X-Ray Characterization of Porous Functional Composites and Membranes, with Resolution from MM to Sub 50 NM.* Journal of Physics: Conference Series, 2009. **152**: p. 012059.
18. Carniglia, S.C., *Construction of the Tortuosity Factor From Porosimetry.* Journal of Catalysis, 1986. **102**: p. 401-418.
19. Micromeritics, *AutoPoreIV Manual*.

20. Tkachuk, A., F. Duewer, H. Cui, M. Feser, S. Wang, and W. Yun, *X-ray Computed Tomography in Zernike Phase Contrast Mode at 8 keV With 50-nm Resolution Using Cu Rotating Anode X-ray Source.* Zeitschrift für Kristallographie - Crystalline Materials, 2007. **222**: p. 650-655.
21. Gostovic, D., J.R. Smith, D.P. Kundinger, K.S. Jones, and E.D. Wachsman, *Three-Dimensional Reconstruction of Porous LSCF Cathodes.* Electrochemical and solid-state letters, 2007. **10**: p. B214-B217.
22. Mulder, M., *Basic Principles of Membrane Technology*. Second edition ed. 1996: Springer.
23. Giesche, H., *Mercury Porosimetry: A General (Practical) Overview.* Particle & Particle Systems Characterization, 2006. **23**: p. 9-19.

Chapter 6.

Understanding Variations in Structural Parameters – Fabrication and Testing of Model Membranes

6.1. Introduction

Engineered osmosis (EO) is a membrane-based technology platform with several applications in varied fields such as desalination (forward osmosis, FO) [3-7], power production (pressure-retarded osmosis, PRO), concentration [8-10] and dewatering (direct osmotic concentration) [11, 12] and many others. EO relies on water being driven across a selective membrane as a result of osmotic pressure gradients between two solutions, the saline feed and a draw solution with a relatively higher solute concentration. While work in EO has caused a recent flurry of research in systems [38, 48] and draw solution design [38, 48, 49] much of the published work has been centered on membrane design. Many of these efforts have been inspired by the thin film composite (TFC) structure widely used in reverse osmosis (RO). TFC FO membrane design departs from RO TFC membranes, however, by employing a support that is designed for high porosity, low tortuosity, and minimal thickness. These features, while unimportant for RO, minimize the structural parameter, which is a metric that is used to ascertain a membrane's propensity to experience internal concentration polarization (ICP). S can be described as the average diffusive path length through the support structure, and is described by the equation

$$S_{\text{int}} = \frac{t\tau}{\varepsilon} \qquad (1)$$

where t is the thickness, τ is the tortuosity, and ε is the porosity of the membrane structure. S is widely used by both academic and industry researchers as an assessment of membrane structural

characteristics for osmotic processes. To determine the value of S, we might consider calculating the individual values of t, τ and ε. While this may sound like a simple solution, measuring porosity and tortuosity, especially of soft materials that may or may not swell in water, is a challenge. We describe these techniques and challenges in our recent publications [13, 15]. However, most of the research community has not adopted this approach. Instead, they use a fitted parameter mass transfer model to determine S from empirical data. That model is shown below [50]:

For when the selective layer faces the draw solution (the PRO mode),

$$S_{eff} = \frac{D}{J_w} \ln \frac{B - J_w + A\pi_{D,m}}{B + A\pi_{F,b}} \qquad (2)$$

For when the selective layer faces the feed solution (the FO mode),

$$S_{eff} = \frac{D}{J_w} \ln \frac{B + A\pi_{D,b}}{B + J_w + A\pi_{F,m}} \qquad (3)$$

where S_{eff} is the "effective" structural parameter, D is the solute diffusivity, J_w is the average water flux, A is the membrane permeance, B is the membrane salt permeability coefficient, π_D is the osmotic pressure of the draw solution and π_F is the osmotic pressure of the feed solution. Subscripts m and b indicate values at the membrane surface and in the bulk solution respectively. The problems associate with using these models have been examined previously by a number research groups. In one such study where Cath et al. [14] were looking to establish a method to standardize FO testing, the authors reported results obtained by seven research groups in testing two types of membranes, one a TFC membrane and the other, was the asymmetric HTI-CTA tested in this study; the membranes they studied were obtained from the same manufacturing

batch and tested under exactly similar experimental conditions. The average S value obtained by the different lab groups was around 535 μm with a standard deviation of about 163 μm which was found to be a non-negligible variation in the context of the study. Further, Wong et al. [16] reported that S, of the HTI-CTA membrane used in their study, varied with both type and concentration of draw solute and even temperature of the draw and feed solutions. These changes had been attributed to possible swelling and de-swelling behavior of the cellulose tri-acetate polymer which has a tendency to absorb water [51]. Furthermore, another fundamental problem with these models is the values used for A and B. In most of the work, the A and B parameters are obtained from RO tests. This may result in error since A and B are likely different under pressure in RO than they are in FO. Further, the concentration of the solute in contact with the membrane selective layer is much lower in RO tests than that in FO tests. This discrepancy between A & B values in FO being different from that in RO has been pointed out by Tiraferri et al. [52]. They showed that there were variations in the A & B values calculated for the four membranes studied (2 TFC FO, 1 asymmetric FO and 1 TFC RO) using the two approaches (RO versus FO) and the variations in B were found to be quite significant for the 2 TFC FO membranes.

To better understand how these models may or may not be accurate, we consider membranes with a structural parameter that is know *a-priori*. We do this by selecting a support material for a TFC membrane that has an "ideal" pore structure consisting of straight, cylindrical pores, (τ=1) and a well-defined thickness and porosity. The membrane must also be self-wetting (i.e. a hydrophilic polymer). We identified track-etched (TE) membranes as having these necessary characteristics. Building a selective layer on top of these membranes would create a selective osmotic membrane with a well-defined structural parameter. Testing under RO and FO

conditions would allow us to compare this intrinsic value to the effective S value. The comparison identified that the validity of existing models are questionable and that new characterization approaches to emerging osmotic membranes are necessary for appropriate comparison.

6.2. Materials and methods

6.2.1 Materials

6.2.1.1 Choice of support layer

The TE support needed to have a pore size rating capable of supporting the polyamide thin film without causing conformal coating during its formation as well as yield reasonable water permeation rates. A 0.2 µm pore size TE membrane (Maine Manufacturing) made of hydrophilized polycarbonate was identified as a viable candidate and was used as the support for TFC membranes.

6.2.1.2 Reagents and membranes

Aqueous diamine monomer *m*-phenylene diamine (MPD, >99%) and organic acid chloride monomer 1,3,5-benzenetricarbonyl trichloride (TMC, 98%) were purchased from Sigma-Aldrich. De-ionized (DI) water obtained from an ultrapure water purification system (Integral 10, Millipore) was used as the solvent for MPD. Hexane (Fisher Scientific) was used as the solvent for TMC. Sodium chloride, NaCl (Fisher Scientific) was used as the solute for RO and FO testing. Commercially-available asymmetric cellulose triacetate (CTA) FO membranes, provided by Hydration Technology Innovations (HTI, Albany, OR) were tested as a control. These membranes are designated as HTI-CTA throughout this article.

6.2.2 Methods

6.2.2.1 Interfacial polymerization

For *in-situ* formation of the polyamide thin film 1% (w/v) MPD and 0.15% (w/v) TMC solutions were formed by dissolving the monomers in their respective solvents and stirring for at least 3 hours prior to using. First, the TE support was taped onto a glass plate and then immersed into the MPD solution for 120 s. Excess MPD was removed from the surface using a rubber roller following which the support was placed in the TMC solution for 60 s. The resulting composite film was immediately placed in an air-circulation oven, kept at 80 °C for 4 min to dry-cure. Any excess reagents were washed off in two successive DI water baths for 5 min each. The TFC membrane, designated as TE-TFC hereafter, was then stored under DI water at 4 °C until further use.

6.2.2.2 Membrane characterization

Surface morphology and cross-sections of the TFC membrane were obtained using a cold cathode field-emission scanning electron microscope (FE-SEM) JSM-6335F (FEI). A thin layer of platinum was sputter-coated onto the samples prior to imaging to obtain good contrast and avoid charge accumulation. The cross-sections were obtained by freeze-fracturing the sample in liquid nitrogen. Surface images of the TE membrane were also obtained to determine the support's porosity by performing image analysis (ImageJ, National Institutes of Health).

6.2.2.3 Determination of pure water permeance, solute permeability coefficient, and solute rejection from cross-flow RO

Pure water permeance, A, of the TE-TFC membrane was obtained by testing in a cross-flow RO system. The membrane was tested under four trans-membrane hydraulic pressures ranging from 6.89-17.24 bar (100-250 psi) at a cross-flow velocity of 0.26 m/s at 20 °C. Salt permeability coefficient, B and intrinsic salt rejection, $\%R_{int}$ were determined using a 2000 ppm NaCl feed at 15.5 and 27.6 bar. Feed and permeate conductivity measurements were made using a conductivity probe in these tests. A, B and $\%R_{int}$ were calculated using formulae available elsewhere [53]. The HTI-CTA was tested as a control. Triplicate tests were performed for both membranes.

6.2.2.4 Evaluation of osmotic water flux and reverse salt flux

Osmotic water fluxes and reverse salt fluxes of the TE-TFC membrane were determined by testing in a custom-built cross-flow FO system. Details of the system set-up are available elsewhere [54]. Tests were performed by orienting the membrane in both FO (selective layer facing the feed) and pressure-retarded osmosis, PRO (selective layer facing the draw) modes. The membranes were tested at 20 °C at a cross-flow velocity of 0.26 m/s at 0 trans-membrane pressure (3 psi hydraulic pressure on both sides). Draw solution concentrations of 0.5, 1.0 and 1.5M NaCl were used while DI water was used as the feed for all tests. The conductivity of the feed solution was monitored using a conductivity probe to measure the reverse salt flux. A membrane from Hydration Technology Innovations (HTI-CTA) was tested as a control. Triplicate tests were performed for both membranes.

6.2.2.5 Calculation of structural parameters

The intrinsic structural parameter, S_{int} of the TE-TFC membrane was calculated using the porosity value obtained from SEM image analysis. Tortuosity was verified to be unity from

cross-section SEM images and the TE support thickness stated by the manufacturer was verified using a micrometer. The effective structural parameter of the membrane was implicitly calculated using the governing equations for water flux in PRO (Equation 2) and FO modes (Equation 3).

6.3. Results and discussion

6.3.1 Characterization of TE and TE-TFC membranes

Figure 6.1a shows the pores in the track-etched membrane. The average porosity obtained from analysis of multiple images was 13±2%. The cross-section of the support shown in Figure 6.1b shows straight pores and confirms that the tortuosity equals one. Figure 6.1c shows that a polyamide layer, having a rough morphology, was formed after interfacial polymerization on the support. The thickness of the TE membrane was 20 µm and the intrinsic structural parameter was calculated to be 133 µm.

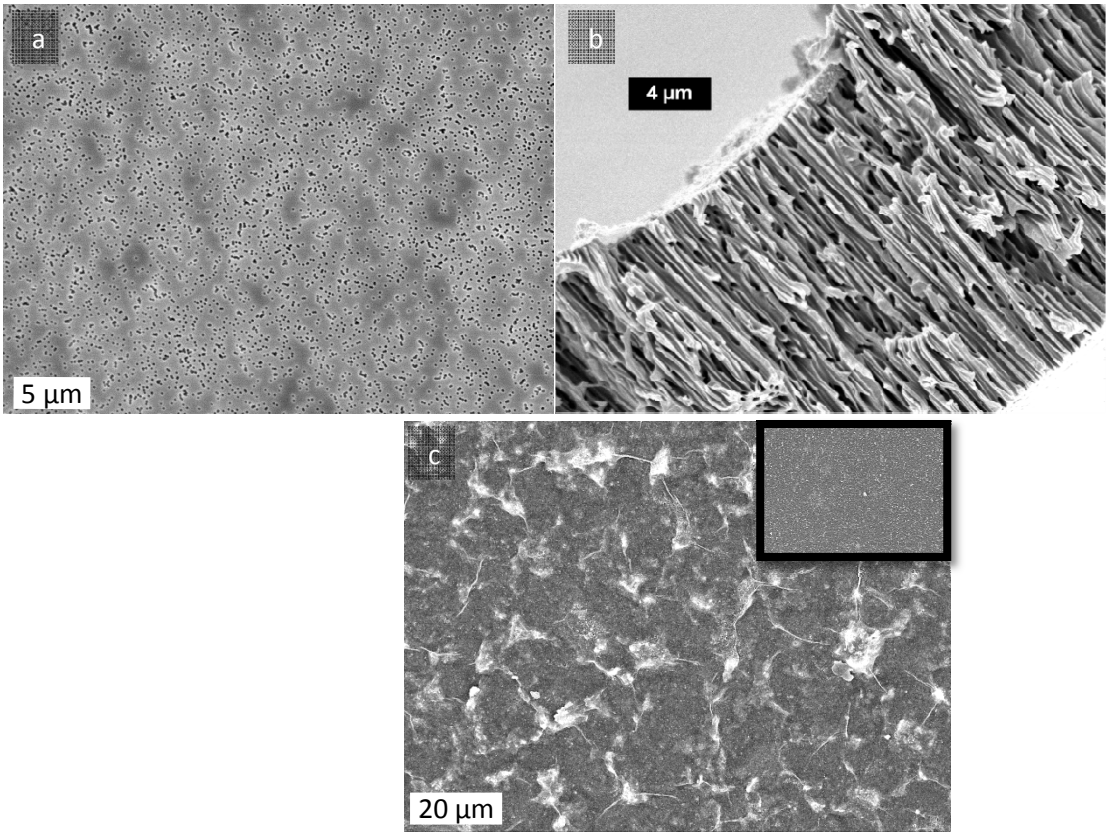

Fig. 6.1. SEM image of (a, b) top and cross-section of 0.2 µm track-etched membrane (TEM) and (c) TE-TFC membrane formed on the TEM. Inset in 1c depicts a larger field-of-view showing the morphology of the polyamide layer. Images 6.1a and b were used to calculate porosity and ascertain tortuosity respectively. Image 1b can also be used to ascertain thickness.

6.3.2 Pure water permeance, solute permeability coefficient, and solute rejection from cross-flow reverse osmosis

Membrane selective layer characteristics, for both the TE-TFC and control HTI-CTA, determined from cross-flow reverse osmosis (RO) tests, are shown in Table 6.1. The salt permeability coefficient, B of the TE-TFC exhibited broader standard deviations than the HTI-CTA, which is common for hand-made membranes. The TE-TFC exhibited reasonable salt rejections, similar to that of the HTI-CTA, and pressure tolerance indicating that the polyamide layer maintained its integrity.

Table 6.1. Membrane selective layer characteristics as determined by cross-flow reverse osmosis tests. Tests were performed at 20°C and 0.26 m/s cross-flow velocity. DI water feed and pressures of 6.89, 10.34, 13.79 and 17.24 bar were used to measure water permeance and a feed consisting of 2000 ppm NaCl was used to measure salt permeability and intrinsic rejections at 15.5 and 27.6 bar.

Membrane	Water permeance, A (lmh/bar)	Salt permeability coefficient, B (lmh)	Intrinsic NaCl rejection, $\%R_{int}$
TE-TFC	0.417±0.012	0.754±0.366	**15.5 bar:** 94.89±2.77
			27.6 bar: 88.63±4.51
HTI-CTA	0.616±0.026	0.699±0.199	**15.5 bar:** 94.11±2.09
			27.6 bar: 95.34±1.29

6.3.3. Osmotic flux performance of TE-TFC membranes

Figure 6.2 shows the osmotic water flux performance of the TE-TFC at draw solution concentrations of 0.5, 1.0 and 1.5 M NaCl with DI water feed. Fluxes of the HTI-CTA are also shown. The water flux increased with draw concentration as expected. The FO and PRO mode fluxes of the TE-TFC matched well for all three draw concentrations indicating that the membrane performance was mostly independent of its orientation. This is a curious result, since usually PRO mode fluxes of EO membranes are almost always greater than their corresponding FO mode counterparts, especially when using a DI water feed, as a result of more severe ICP in the FO mode compared to that in the PRO mode. This typical behavior is seen here in the HTI-CTA performance as well. The reverse solute fluxes, shown in Figure 6.3, show an expected similar trend, increasing with draw concentration for both membranes, with the PRO mode salt fluxes being larger than the corresponding FO mode ones for the HTI-CTA membrane due to the higher water fluxes. No clear differences were visible between the two modes for the TE-TFC membrane since the error bars for the FO mode were large which is common in a number of osmotic tests of hand-made membranes and when deionized water feeds are used.

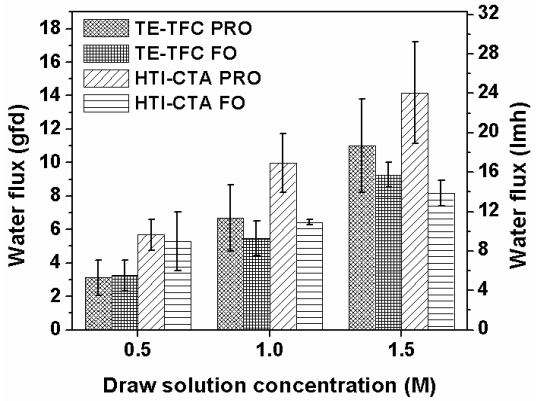

Fig. 6.2. Osmotic water fluxes of the TE-TFC membrane in PRO and FO membrane orientations. Data for a commercial FO membrane, the HTI-CTA is shown for comparison. Tests were

performed at 20°C, 0.26 m/s cross-flow velocity with DI water feed at 0 transmembrane pressure. Three membrane coupons were analyzed for all tests.

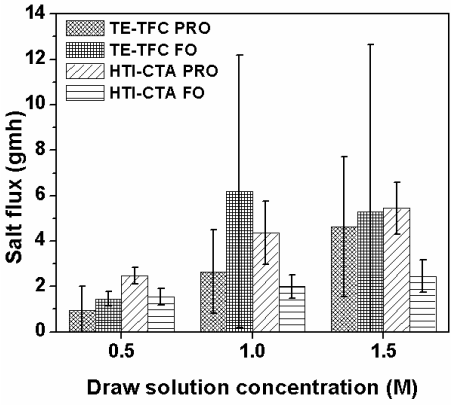

Fig. 6.3. Reverse salt fluxes of the TE-TFC membrane in PRO and FO membrane orientations. Data for a commercial FO membrane, the HTI-CTA is shown for comparison. Tests were performed at 20°C, 0.26 m/s cross-flow velocity with DI water feed at 0 transmembrane pressure. Three membrane coupons were analyzed for all tests.

6.3.4 Structural parameters in FO and PRO modes

The S values of both the TE-TFC and HTI-CTA membrane were calculated, using equations 2 and 3, at the different draw concentrations and are tabulated in Table 6.2. In PRO mode the S values for both membranes were found to vary significantly between the different coupons tested and with change in draw concentration as well. This is possibly due to the differences in A and B values of membranes in an RO versus an FO test [52]. In the PRO mode, both water and salt flux are relatively high implying a greater influence of A and B in the calculation of S. Inaccuracies in the membrane selective layer properties chosen would thus result in a consequent inaccuracy in the S values calculated. The variations between the different membrane coupons at each draw concentration decreased for the TE-TFC membrane whereas for the HTI-CTA they continued to be rather large. In the case of the latter, it is possible that osmotic de-swelling at high solute concentrations, leading to structural changes, could further exacerbate the effect of inaccurate A and B values.

Table 6.2. Effective structural parameters of the TE-TFC membrane in PRO and FO membrane orientations. Data for a commercial FO membrane, the HTI-CTA is shown for comparison. Tests were performed at 20°C, 0.26 m/s cross-flow velocity with DI water feed at 0 transmembrane pressure. Three membrane coupons were used for all tests.

Draw solution concentration, M	TE-TFC		HTI-CTA	
	PRO mode	FO mode	PRO mode	FO mode
0.5	1917±508	621±3	1077±523	485±131
1.0	1165±127	480±15	773±364	445±65
1.5	758±114	219±9	527±377	398±72
Average	1280±588	440±204	793±275	443±43

In the FO mode, a similar decrease in S with increase in draw concentration was observed with the overall change in the value being relatively smaller for the HTI-CTA compared to that of the TE-TFC. This is due to the B value of the hand-made TE-TFC varied over a wider range than their HTI-CTA counterparts (Table 6.2). This variation in salt permeability of the TE-TFC membrane between different coupons, when incorporated in Equation 3, is reflected as a consequent change in S. Not surprisingly, the effective S values of the TE-TFC membrane obtained at different testing conditions were all far removed from the intrinsic S value of 133 μm. There exists a strong dependence of S on the testing conditions and changes to such conditions, which are completely external to the membrane structure itself, cause a non-trivial change to the value of the structural parameter. This clearly necessitates the need for a modification to the current approach of characterizing FO membranes' structure in order to obtain reasonably accurate estimations of their suitability for FO.

6.5. Conclusions

This study confirms that existing methods of calculating S in asymmetric and TFC membranes are inaccurate. These methods, including a number of fitted parameter models, fail to account for the numerous mass transfer resistances present across the membrane. These limitations make fair

comparisons between new membrane types and architectures impossible. One alternative is to accurately account for each resistance and attribute only the structural resistances to the S value. This is difficult, however, since such an analysis would require the use of empirical correlations that may or may not be appropriate for the system geometry or may have inputs (such as diffusivity) that are estimated or unavailable for solutions containing multiple solutes. Another option is to measure the S value using imaging and/or analytical tools. Some of these tools may only offer limited resolution or may have an inherent bias depending on their operating conditions. While a definitive solution to this problem is not offered as part of this study, researchers working in this area should be cognizant of the limitations of the existing methods.

References

1. Cath, T.Y., N.T. Hancock, C.D. Lundin, C. Hoppe-Jones, and J.E. Drewes, *A multi-barrier osmotic dilution process for simultaneous desalination and purification of impaired water.* Journal of Membrane Science, 2010. **362**(1): p. 417-426.
2. Choi, Y.-J., J.-S. Choi, H.-J. Oh, S. Lee, D.R. Yang, and J.H. Kim, *Toward a combined system of forward osmosis and reverse osmosis for seawater desalination.* Desalination, 2009. **247**(1): p. 239-246.
3. Kessler, J.O. and C.D. Moody, *Drinking water from sea water by forward osmosis.* Desalination, 1976. **18**(3): p. 297-306.
4. Martinetti, C.R., A.E. Childress, and T.Y. Cath, *High recovery of concentrated RO brines using forward osmosis and membrane distillation.* Journal of Membrane Science, 2009. **331**(1): p. 31-39.
5. McCutcheon, J.R., R.L. McGinnis, and M. Elimelech, *A novel ammonia-carbon dioxide forward (direct) osmosis desalination process.* Desalination, 2005. **174**(1): p. 1-11.
6. Lee, K.L., R.W. Baker, and H.K. Lonsdale, *Membranes for power generation by pressure-retarded osmosis.* Journal of Membrane Science, 1981. **8**(2): p. 141-171.
7. Sepp□l□, A. and M.J. Lampinen, *Thermodynamic optimizing of pressure-retarded osmosis power generation systems.* Journal of Membrane Science, 1999. **161**(1): p. 115-138.
8. Skilhagen, S.E., J.E. Dugstad, and R.J. Aaberg, *Osmotic power - power production based on the osmotic pressure difference between waters with varying salt gradients.* Desalination, 2008. **220**(1): p. 476-482.
9. Garcia-Castello, E.M. and J.R. McCutcheon, *Dewatering press liquor derived from orange production by forward osmosis.* Journal of Membrane Science, 2011. **372**(1): p. 97-101.
10. Jin, X., J. Shan, C. Wang, J. Wei, and C.Y. Tang, *Rejection of pharmaceuticals by forward osmosis membranes.* Journal of hazardous materials, 2012. **227**: p. 55-61.
11. Kim, T.W., Y. Kim, C. Yun, H. Jang, W. Kim, and S. Park, *Systematic approach for draw solute selection and optimal system design for forward osmosis desalination.* Desalination, 2012. **284**: p. 253-260.
12. Zhao, S., L. Zou, C.Y. Tang, and D. Mulcahy, *Recent developments in forward osmosis: opportunities and challenges.* Journal of Membrane Science, 2012. **396**: p. 1-21.
13. Achilli, A., T.Y. Cath, and A.E. Childress, *Selection of inorganic-based draw solutions for forward osmosis applications.* Journal of Membrane Science, 2010. **364**(1-2): p. 233-241.
14. Manickam, S.S., J. Gelb, and J.R. McCutcheon, *Pore structure characterization of asymmetric membranes: Non-destructive characterization of porosity and tortuosity.* Journal of Membrane Science, 2014. **454**: p. 549-554.
15. S Manickam, S. and J.R. McCutcheon, *Characterization of polymeric nonwovens using porosimetry, porometry and X-ray computed tomography.* Journal of Membrane Science, 2012. **407**: p. 108-115.
16. Loeb, S., L. Titelman, E. Korngold, and J. Freiman, *Effect of porous support fabric on osmosis through a Loeb-Sourirajan type asymmetric membrane.* Journal of Membrane Science, 1997. **129**(2): p. 243-249.
17. Cath, T.Y., M. Elimelech, J.R. McCutcheon, R.L. McGinnis, A. Achilli, D. Anastasio, A.R. Brady, A.E. Childress, I.V. Farr, N.T. Hancock, J. Lampi, L.D. Nghiem, M. Xie, and N.Y. Yip, *Standard Methodology for Evaluating Membrane Performance in Osmotically Driven Membrane Processes.* Desalination, 2012. **312**(0): p. 31-38.

18. Wong, M.C.Y., K. Martinez, G.Z. Ramon, and E. Hoek, *Impacts of operating conditions and solution chemistry on osmotic membrane structure and performance.* Desalination, 2012. **287**: p. 340-349.
19. Mehta, G.D. and S. Loeb, *Performance of Permasep B-9 and B-10 membranes in various osmotic regions and at high osmotic pressures.* Journal of Membrane Science, 1979. **4**: p. 335-349.
20. Tiraferri, A., N. Yin Yip, A.P. Straub, S. Romero-Vargas Castrillon, and M. Elimelech, *A Method for the Simultaneous Determination of Transport and Structural Parameters of Forward Osmosis Membranes.* Journal of Membrane Science, 2013. **444**: p. 523-538.
21. Mulder, M., *Basic Principles of Membrane Technology Second Edition*. Second ed. 1996: Kluwer Academic Pub.
22. Arena, J.T., B. McCloskey, B.D. Freeman, and J.R. McCutcheon, *Surface modification of thin film composite membrane support layers with polydopamine: enabling use of reverse osmosis membranes in pressure retarded osmosis.* Journal of Membrane Science, 2011. **375**(1): p. 55-62.

Chapter 7
Numerical Simulation Of Transport In Forward Osmosis

7.1. Introduction

Engineered osmosis (EO) is an emerging technology platform comprising a number of membrane-based separations. These include subset technologies such as forward osmosis (FO), pressure-retarded osmosis (PRO), direct osmotic dilution and direct osmotic concentration, which can be used for water treatment, power production, emergency relief scenarios and dewatering, respectively, to name a few applications [1-8]. These technologies rely on osmotic pressure gradients between a concentrated draw solution and a relatively dilute feed solution. The water flux performance of EO membranes, typically belonging to the thin film composite (TFC) architecture, is critical for successful commercialization of the technology. This performance is in turn dependent on the osmotic pressure gradient realized over the selective layer of the TFC membrane. The membrane support layer however, poses a resistance to draw (in FO) and feed (in PRO) solute mass transport thus dramatically reducing the available driving force. This phenomenon is referred to as internal concentration polarization (ICP) and is a major limitation in commercializing EO processes [9]. The EO community commonly uses the intrinsic structural parameter, S_{int}, *as a metric to denote the influence of the membrane structure on the severity of ICP.* S_{int} is defined as

$$S_{\text{int}} = \frac{t\tau}{\varepsilon} \qquad (1)$$

where t is the thickness, τ is the tortuosity, and ε is the porosity of the membrane structure. To this end, most EO membrane developers have focused on optimizing the support layer characteristics in order to reduce S_{int} and hence, the severity of ICP. This is typically done by

individually manipulating the different structural metrics (t, τ or ε) to reduce S_{int}. However, post-membrane fabrication, characterizing these metrics and hence, the overall value of S_{int} is a challenge for such soft materials. A common alternative to calculating S_{int} has been to calculate an effective structural parameter, S_{eff}, from osmotic flux measurements. This is done with the use of empirical models derived from the flux governing equation accounting for the different mass transfer resistances across the membrane using chemical engineering film theory principles. A number of assumptions regarding solution properties, among other things, are used in deriving these models and such inherent limitations lead to severe flaws in the use of these models in certain situations. Further, significant deviations between the intrinsic and effective structural parameters have been observed in both previous studies by these authors as well as others [10-12]. In light of this situation, it is seen that there exist no known methodologies to reasonably evaluate the influence of different structural metrics and assess their effect on EO performance. Perhaps, the three structural metrics (t, τ and ε) impact membrane transport to varying degrees and need to be weighted differently. Apart from these three average metrics there also exist other parameters that might influence how the structure affects flux performance, such as pore radius, pore-pore spacing, pore geometry etc. Furthermore, limitations of the structural parameter concept in deducing structural resistance to transport also means that there are currently no methods to reliably compare the new and novel EO membranes being made.

In this work, we propose the use of a numerical simulation approach to study the impact of structural metrics on membrane transport phenomena. Such a computational approach serves as a relatively rapid method of evaluating the effect of different parameters on a given process. Such an approach has, in fact, previously been used to study the impact of support layer properties on reverse osmosis (RO) membrane transport [13]. In this study, a model geometry

similar to that devised by Ramon et al. [13] is used and a mathematical model describing the coupled transport phenomena in both the selective layer (film) and the porous support is developed, along with boundary conditions to solve the equations. The influence of different structural metrics like support pore radius, support porosity and support thickness along with the effect of varying draw and feed concentrations are studied. The simulated results yielded interesting insights on the impact of support layer properties that can inform future osmotic membrane designers on the parameters that would benefit from optimization for enhanced flux performance.

7.2. Theory

7.2.1 Numerical Model

The purpose of the developed model was to assess, quantitatively, the impact of the support structural metrics, namely pore radius, porosity and thickness on the transport phenomena across the membrane. Additionally, the effect of feed and draw concentrations has also been examined. A 2D schematic of the model geometry used in the numerical simulations is shown in Fig.7.1. The geometry was made to be axi-symmetric in order to reduce the computation time be half.

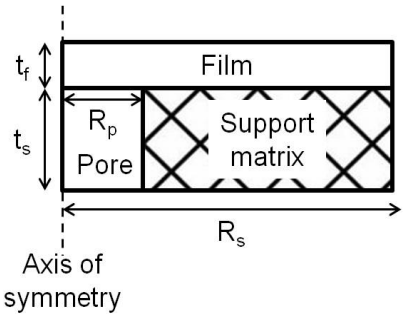

Fig. 7.1. Schematic drawing illustrating the side view of the 2D cell geometry used for the model calculations.

In the following model, it is assumed that the film is perfectly selective, exhibiting 100% solute rejection, and that transport through it occurs solely by solution-diffusion. This transport is dictated by gradients in the chemical potential of the diffusing water across the film. This chemical potential is represented in this model as a concentration of water. The steady state concentration field within the film is governed by the 2D Laplace equation,

$$\frac{1}{r}\frac{\partial}{\partial r}\left(r\frac{\partial c_w}{\partial r}\right)+\frac{\partial^2 c_w}{\partial z^2}=0 \qquad (2)$$

where c_w is the concentration of water and r and z represent the cylindrical coordinates in the system. Two boundary conditions are imposed in solving the above equation:

At the film-draw interface, $c_w = c_{wD}$

At the film-pore interface, we set osmotic water flux = diffusive water flux, i.e.,

$$A\Delta\pi = D\frac{dc_w}{dz} \qquad (3)$$

$$A(\pi_D-\pi_F)=D_w\frac{c_{wD}-c_{wf-s}}{t_f} \qquad (4)$$

In the above equation, A was set to be $2.7*10^{-13}$ m/s/Pa to make it fairly consistent with the use of experimentally determined A values of TFC membranes with a geometry similar to the one in Fig. 7.1 [ref, this dissertation]. While this is recognized as not being a rigorous way of calculating A there is also a lack of reliable data for the isolated thin-film making such an assumption the only possible alternative. The only unknown in Eqn. 4 is the concentration of water at the film-support interface which can then be calculated.

In the support domain, transport is assumed to occur only within the pore and the support matrix is assumed to be impermeable to transport. This is a fair assumption since even in the case of hydrophilic support materials the rate of transport through open pores will far exceed that through the support matrix. In the pore, convective and diffusive transport compete with each other in opposing directions and the advection-diffusion equation is used to describe this:

$$D\left(\frac{1}{r}\frac{\partial}{\partial r}\left(r\frac{\partial c_s}{\partial r}\right)+\frac{\partial^2 c_s}{\partial^2 z}\right)-u_z.\frac{\partial c_s}{\partial z}=0 \qquad (5)$$

A full model should account for the radial variation of the velocity as well but it is assumed that this decays fast and, due to the high aspect ratio of the pore, the problem becomes rapidly one-dimensional. Here again, two boundary conditions are used to solve the above equation. At the pore-feed interface, c_s was set equal to c_{sF}. To calculate u_z in the above equation, the integrated mass flux is averaged over the pore and converted to a velocity:

$$u_z = D_w \int_{\substack{\text{film-pore}\\ \text{interface}}} \frac{dc_w}{dz}\frac{M_{H_2O}}{\rho_{H_2O}.A_p} \qquad (6)$$

The different structural metrics were varied as follows: pore radius was varied over two orders of magnitude from 0.01 µm to 0.1 µm to 1 µm. Pore radii between 0.01 and 0.1 µm can be approximated as the typical size range in phase inversion cast supports [14-16]. Sizes between 0.1 and 1 are typical in newer, more novel supports such as electrospun supports [17]. For porosity, calculated as R_p^2/R_s^2 in Fig.1, values of 45, 65 and 85% were chosen with values around 45% being typical of phase inversion cast supports [12], porosities around 65% being reported for some of the newer EO membranes [18]. Electrospun supports commonly have porosities upwards of 85% [19]. Two thicknesses of 25 and 50 µm were explored: 50 µm is the

average thickness of the HTI-CTA membrane which, for long, was the only FO membrane commercially available from Hydration Technology Innovations. Newer EO membrane supports are constantly pushing the lower limits of thicknesses, with supports as thin as 8-15 μm being fabricated [17, 18]. In varying solution concentrations (the feed and draw solute were both always NaCl), feeds of 0.1, 0.5, 1 and 2M were chosen representing brackish water, seawater. The draw solution was varied between 0.5, 1, 2 and 4M to denote seawater, and brine respectively.

It is to be noted that only one parameter was changed at a time, for instance, when pore radius was varied porosity and thickness were kept constant by tweaking the model geometry accordingly. The geometry in Fig. 1 was meshed in to triangular-shaped elements in order to enable solving the model equations using finite element analysis. A non-linear solver was used to solve the equation using algorithms available in COMSOL Multiphysics, version 4.3a. An extra-fine mesh was used at the film-pore interface to reliable resolve small concentration gradients at this boundary.

7.3. Results and Discussion

7.3.1 Validation of model with experimental data

As a validation of the developed model were run to compare model predictions to experimental results obtained from a model TFC membrane [ref, this dissertation]. Structural metrics in the simulations were matched with that of the actual membrane; pore radius was set at 0.2 μm, porosity was 13%, film and support thickness were 100 nm and 20 μm respectively. The feed was DI water and draw concentrations of 0.1, 0.5, 1 and 1.5M were tested. The conditions of the osmotic flux measurements were: 20 °C, cross-flow velocity of 0.26 m/s and test cell

channel N_{Re} of 1190 [ref, this dissertation]. Comparisons between the experimental and simulated water fluxes are shown in Fig. 7.2.

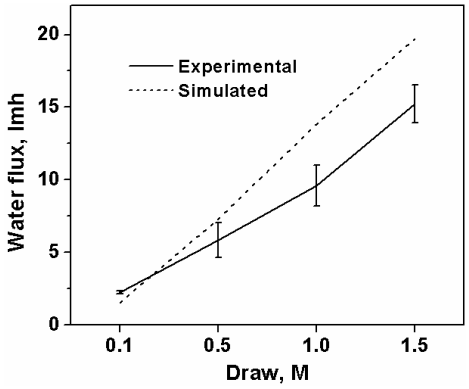

Fig. 7.2. Validation of the developed model with experimental data (FO mode) from [ref, this dissertation]. Simulation conditions matched the experiments with a pore radius of 0.2 μm and a porosity of 13%. The film was 100 nm thick and the support thickness was 20 μm. The feed was DI water. In the osmotic flux tests, temperature was set at 20 °C and the cross-flow velocity was 0.26 m/s. N_{Re} of the test cell channel was 1190 [ref, this dissertation].

The two fluxes followed nearly the same trend with the simulation predicting a lower flux at 0.1M draw and thereafter predicting higher water fluxes. It is to be noted that at 0.1M draw, the water fluxes are pretty low to be reliably accurate. In the case of the model TFC membrane the polyamide layer is not perfectly selective (as in the case of the simulations) and as the water flux increases the salt flux increases as well. This leads to a loss in % driving force available, a fact not reflected in the simulations. Nevertheless, this comparison serves as a reasonable validation of the developed mathematical model.

7.3.2 Film and Pore Transport Profiles

Post-validation, the model was first used to predict film and pore transport profiles with changes in solution concentrations. Fig. 7.3 shows intensity maps depicting transport of water through the film in the FO mode. Feed concentration was fixed at 0.1 M and draw concentration was increased from 0.5 – 4.0M. The color legend corresponds to the concentration of water in

mol/l. As the draw concentration was increased water transport streamlines were seen to become increasingly prominent implying an increase in rate of water flow. Further, the rate of flow is seen to be highest at the center of the pore indicating that the flux is highest along this central axis where it is undisturbed by drag effects of the pore wall.

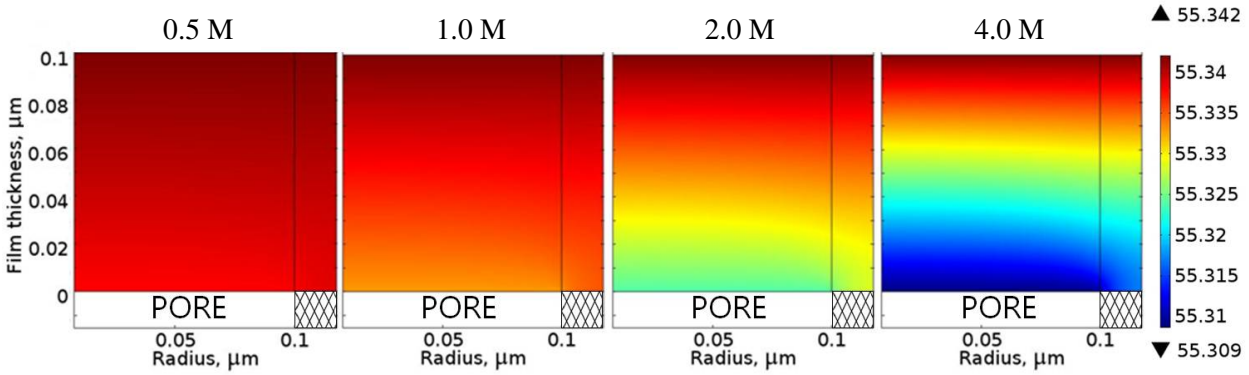

Fig. 7.3. Intensity maps depicting transport of water through the film in the FO mode. More water is transported as draw concentration is increased, from 0.5 – 4.0M to the right. Feed concentration was fixed at 0.1 M. The color legend corresponds to the concentration of water in mol/l.

Fig. 7.4a and b are intensity maps depicting pore solute transport in the FO and PRO mode respectively. In Fig. 7.4a feed concentration increases from 0.1 – 2.0 M to the right. Draw concentration was fixed at 4.0 M. In Fig. 7.4b, draw concentration increases (water flux increases) from 0.5 – 4.0 M to the right. Feed concentration was fixed at 0.1 M. In both 7.4a and b, pore radius was 0.1 µm, porosity was 65% and support thickness was 50 µm. From Fig. 7.4a it is seen that as feed concentration is increased, and hence water flux decreases, the severity of dilutive ICP decreases. A progressively larger fraction of the pore was seen to be equilibrium with the bulk draw concentration as the feed increased from 0.1 to 2M. Similarly, for the PRO mode, it can be seen from Fig. 7.4b that an increase in water flux with an increase in draw concentration leads to more severe ICP. These intensity maps in Fig. 7.3 and 7.4 ratify that the

developed model can be used to reasonably evaluate the effect of different the structural metrics on transport.

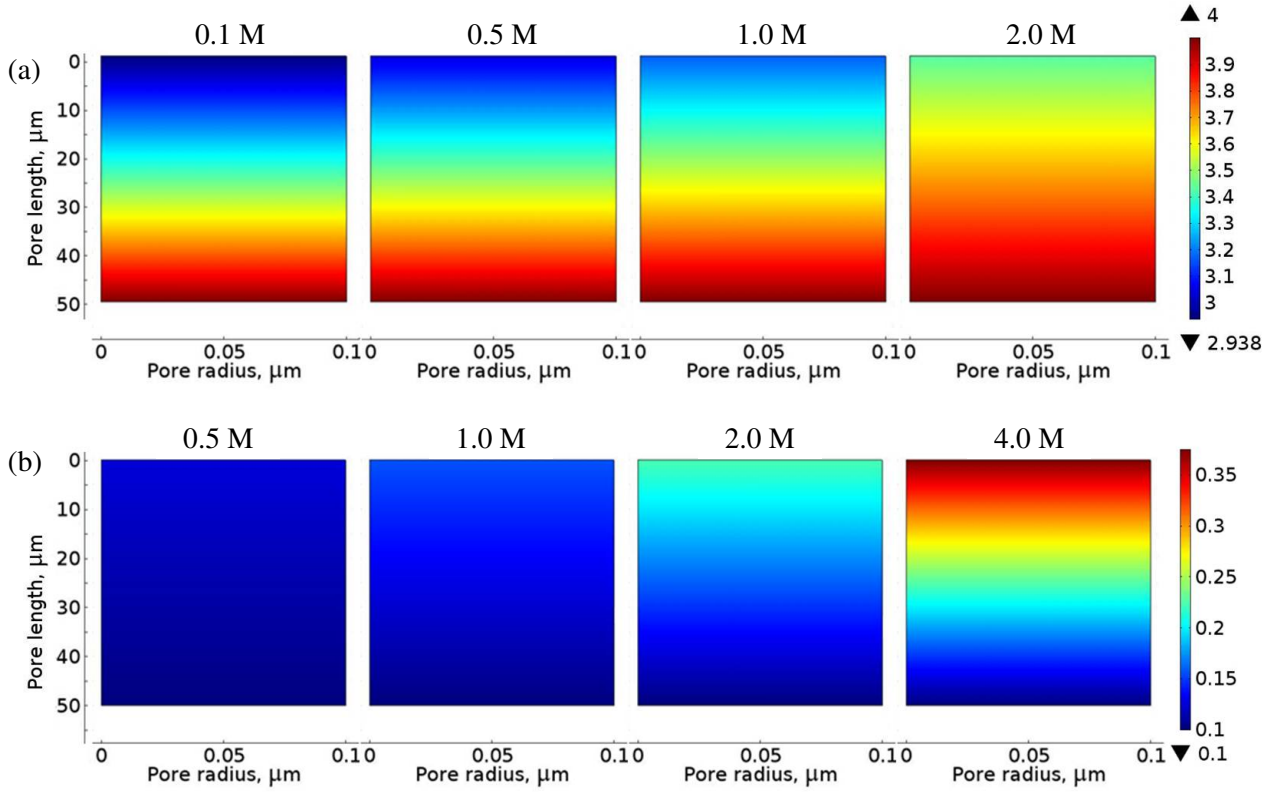

Fig. 7.4. Intensity maps depicting solute (NaCl) concentration profiles in the pore for FO mode (a) and PRO mode (b). (a) Severity of dilutive ICP is seen to decrease as feed concentration increases (water flux decreases) from 0.1 – 2.0 M to the right. Draw concentration was fixed at 4.0 M. (b) Severity of concentrative ICP is seen to increase as draw concentration increases (water flux increases) from 0.5 – 4.0 M to the right. Feed concentration was fixed at 0.1 M. R_p = 0.1 µm, ε = 65% and t_s = 50 µm in both 4a and b. The color legend corresponds to the concentration of NaCl in mol/l.

7.3.3 Effect of Pore Radius

The effect of pore radius on transport is shown in Fig. 7.5 where 7.5a represents the severity of ICP in terms of an ICP modulus. ICP modulus can be given as

$$ICP\ modulus = \frac{Concentration\ at\ \ film - pore\ interface}{Concentration\ at\ \ pore - draw(feed)\ interface} \qquad (7)$$

An infinitesimal difference in performance was observed upon increasing the pore radius from 0.01 to 0.1 µm but upon further increasing to 1 µm a small yet noticeable improvement in performance was seen for both modes. Fig. 7.5a seems to imply that concentration of the dilute feed in PRO mode results in perhaps more severe polarization than dilution of the concentrated draw in FO mode. However, when these ICP moduli are translated into a % loss in driving force across the support layer (due to ICP) it can be seen that FO mode ICP is far more severe than that in PRO mode. In these simulations feed and draw were 0.1 M and 4.0 M NaCl, respectively, porosity was 65% and support thickness was 50 µm.

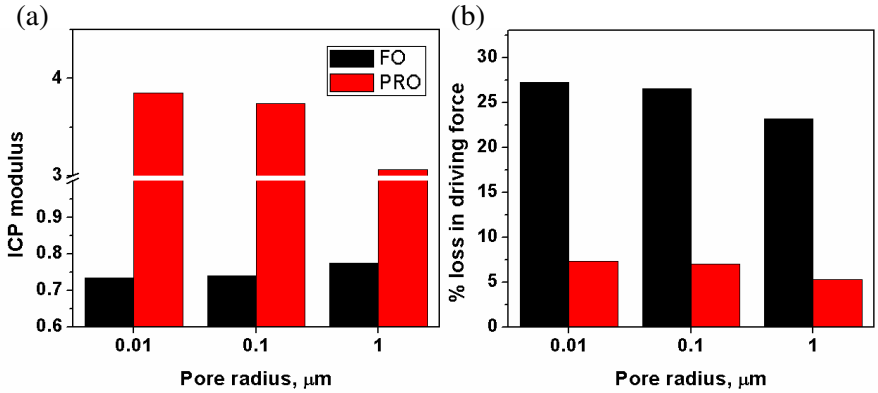

Fig. 7.5. (a) Effect of pore radius on severity of ICP for FO and PRO modes. (b) % driving force lost across the support layer due to ICP. Feed and draw were 0.1 M and 4.0 M NaCl, respectively. $\varepsilon = 65\%$ and $t_s = 50$ µm.

This improvement in performance upon increasing pore radius can be translated into a flux (in velocity units), as shown in Fig. 7.6. The simulation conditions were the same as in Fig. 7.5. This velocity is akin to water flow rate in a pipe where for a fixed quantum of water, the flow rate decreases with increase in pipe diameter. The drop in velocity is shaper upon going from 0.1 to 1 µm than going from 0.01 to 0.1 µm. Fig. 7.7 hypothetically demonstrates this effect of flux rate on ICP. In this schematic, the three membranes have different pore radius and the porosity is kept constant by increasing the support width. This reflects the scenario in the actual simulation. The membranes are all subject to the same driving force. The illustration is shown

for the PRO mode and the hypothesis is the same for FO mode. In smaller pores the higher velocities carry along more solute molecules to the pore-film interface where they are then distributed over a smaller interfacial area compared to the larger pores. This directly corresponds to a more severe ICP in smaller pores.

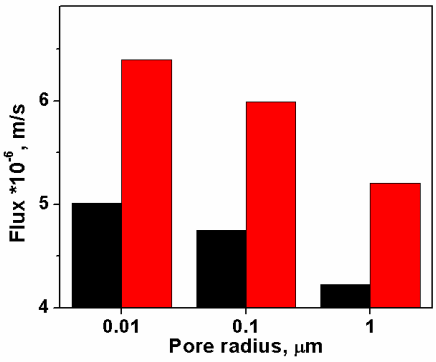

Fig. 7.6. Flux (in velocity units) as a function of pore radius. Feed and draw were 0.1 M and 4.0 M NaCl, respectively. ε = 65% and t_s = 50 μm.

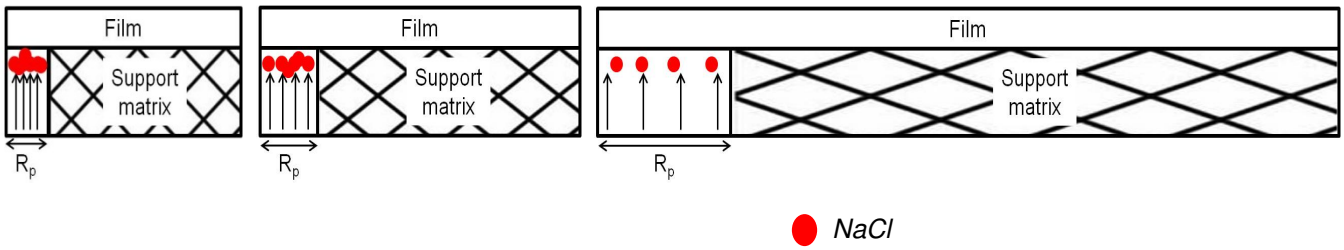

Fig. 7.7. Schematic showing the hypothetical effect of pore radius on severity of ICP, using the PRO mode for illustration. Note that all three membranes are subjected to the same driving force, i.e. similar draw and feed concentrations. For smaller pore sizes, higher convective flux (indicated by arrows) carries along more solute molecules to the pore-film interface which are then subsequently distributed over a smaller area thus leading to more severe ICP.

7.3.4 Effect of Porosity

Fig. 7.8 demonstrates the effect of porosity on pore transport. Here, feed and draw were 0.1 M and 4.0 M NaCl, respectively, pore radius was 0.1 μm and support thickness was 50 μm. It was found from Fig. 7.8a that the increments in porosity gave a step-wise improvement in performance here, as opposed to the effect of pore radius. A similar correlation to % loss in

driving force was observed where ICP severity in FO mode far outweighs that in PRO mode. It was found, again, that the flow rates in the pore were larger for smaller porosities than for the larger porosities implying that both pore radius and porosity affect transport along similar principles, outlined in Fig. 7.7.

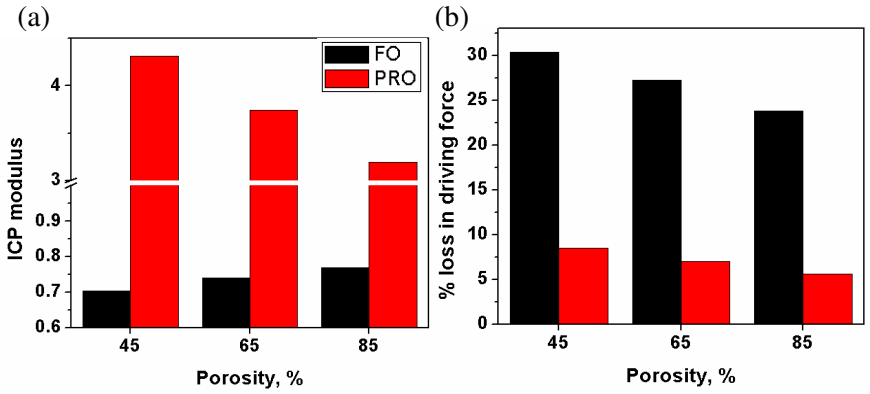

Fig. 7.8. (a) Effect of porosity on severity of ICP for FO and PRO modes. (b) % driving force lost across the support layer due to ICP with FO mode losses being much more severe than PRO mode ones. Feed and draw were 0.1 M and 4.0 M NaCl, respectively. R_p = 0.1 µm and t_s = 50 µm.

7.3.5 Effect of Thickness

The influence of support thickness on ICP is depicted in Fig. 7.9. Feed and draw were 0.1 M and 4.0 M NaCl, respectively, pore radius was 0.1 µm and porosity was 65%. Fig. 7.9a shows a sharp decline in ICP severity as the thickness in decreased by half from 50 to 25 µm. this relates to a similar dramatic drop in % driving force lost as seen in Fig. 7.9b. Driving force losses of around 15% in the FO mode were among the lowest values observed in this study among all parameters studied. Such an enhancement in performance with reduction in support thickness can be attributed to a direct increase in driving force for solute back diffusion. Fick's first law of diffusion states that diffusive flux, $J_i = D.(dc_i/dz)$. Reducing thickness implies decreasing the dz term thus directly corresponding to an increase in driving force for solute back diffusion.

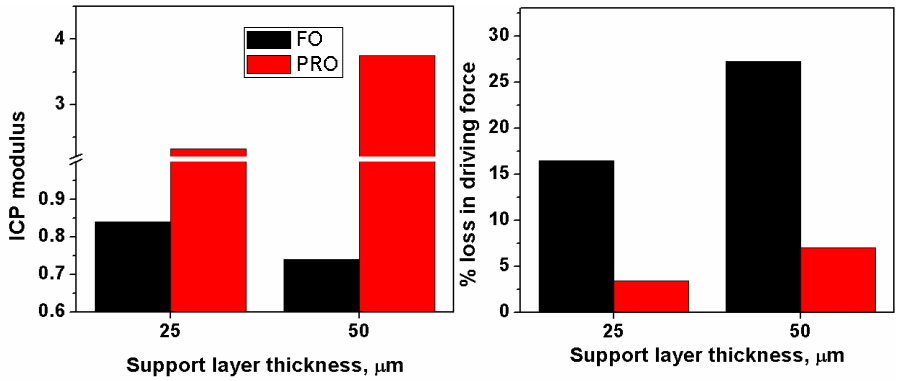

Fig. 7.9. (a) Effect of thickness on severity of ICP for FO and PRO modes. (b) % driving force lost across the support layer due to ICP with FO mode losses being much more severe than PRO mode ones. Feed and draw were 0.1 M and 4.0 M NaCl, respectively. R_p = 0.1 μm and ε = 65%.

7.3.6 Relative Influence of Porosity vs. Thickness

Among the structural metrics in the S_{int} formula (Eqn. 1), tortuosity was held constant at 1 in this study and porosity and thickness were both doubled and halved by 50% respectively. As seen in the previous section a reducing thickness seemed to show the maximum enhancement in performance compared to either increasing pore radius or porosity. This finding has, in fact, been previously experimentally observed by Bui [19] in work on electrospun nanofiber-supported EO membranes. In order to reliably evaluate our observation the intrinsic structural parameters were kept constant between two sets of simulations in which porosity and thickness were increased and decreased, by 89% respectively. One parameter was kept constant when the other one was varied. Thickness was fixed at 50 μm when porosity was varied between 45 and 85% and porosity was kept constant at 65% when thickness was changed between 38 and 72 μm. Fig. 7.10 summarizes the results for the FO (Fig. 7.10a) and PRO (Fig. 7.10b) modes. It can be seen that, in both modes, reducing the thickness showed a more significant enhancement in performance compared to increasing the porosity. The direct reduction in the path length for solute back diffusion upon decreasing the thickness seemed to far outweigh improvements in performance as a result of marginal decreases in flux rates that are derived from increasing porosity.

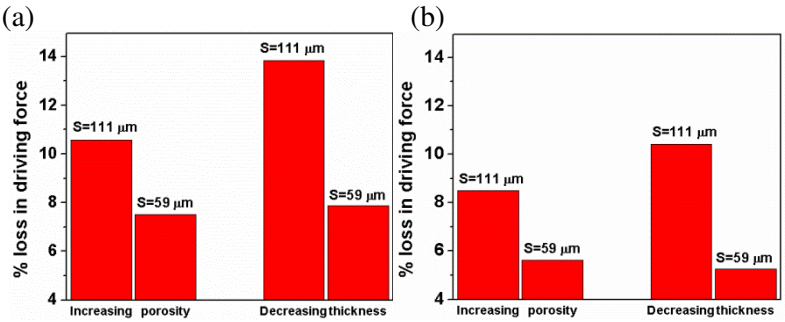

Fig. 7.10. Relative influences of changing porosity and thickness independently while varying structural parameter between two values, viz. 111 and 59 μm. While porosity was increased from 45 to 85% the thickness was kept constant at 50 μm and when thickness was decreased from 72 to 38 μm porosity was kept constant at 65%. It is to be noted that both porosity and thickness were changed by 89%. Feed and draw were 0.1 M and 4.0 M NaCl, respectively and pore radius was 0.1 μm.

7.3.7 Effect of Varying Draw and Feed Concentrations

Fig. 7.11 shows the effect of varying draw and feed concentrations on pore transport in FO (Fig. 7.11a) and PRO (Fig. 7.11b) modes. For the sake of brevity, only changes in performance as a function of pore radius are shown here. However, similar trends were observed upon changing solution concentrations while varying porosity and thickness as well. It was seen, from Fig. 7.11a, that upon increasing the draw concentration and hence waster flux, the % driving force lost increased as well.

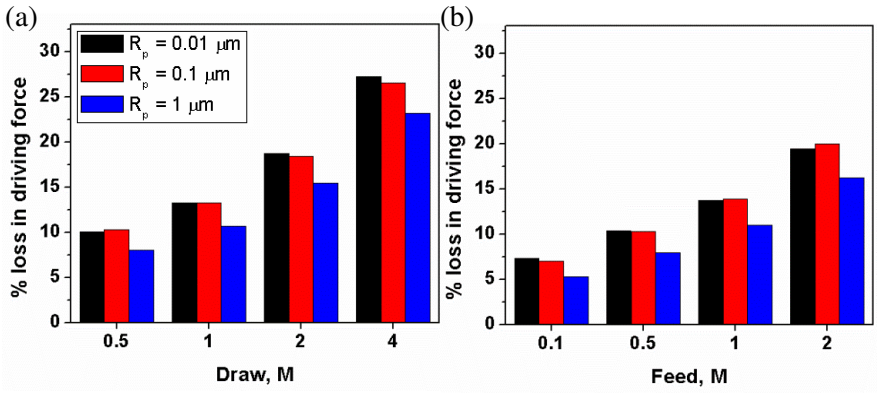

Fig. 7.11. Effects of varying concentrations of (a) draw in the FO mode and (b) feed in the PRO mode on the severity of ICP, depicted here as a % loss in driving force. ε = 65% and t_s = 50 μm.

7.3.8 Sensitivity Analysis

To determine the influence of the assumption of a water permeance (A) value on the simulation outcome, a sensitivity analysis was performed where the A value was changed between $1.7*10^{-13}$ and $3.7*10^{-13}$ m/s/Pa with the median value ($2.7*10^{-13}$) being our assumption in all the other simulations. The results of this analysis are presented in Fig. 7.12 where the influence of changing A on % driving force lost is shown. The FO mode simulations seem to be more sensitive to changes in A than their PRO mode counterparts. This is due to the fact that FO mode ICP is typically more pronounced than PRO mode ICP, especially in the absence of a reverse salt flux (possible only in membranes with solute rejection less than 100%). While the developed model was seen to be moderately sensitive to changes in A value in the FO mode it was seen that the different A values did not affect the overall trends outlined in sections 7.3.3, 7.3.4 and 7.3.5. The findings presented in this study are mainly illustrative of physical trends and are not intended to provide any predictive capacity.

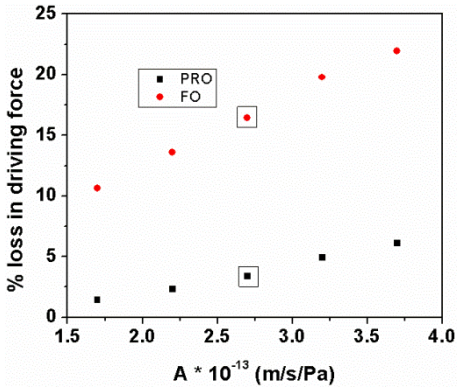

Fig. 7.12. Analysis of the sensitivity of the developed model to changes in the membrane permeance, A, in both FO and PRO mode. The data points that are highlighted with a square refer to the "base" A value used in all other simulations in this study. The FO mode simulations were more sensitive to changes in A values compared to the PRO mode ones. Feed and draw were 0.1 M and 4.0 M NaCl, respectively.

7.4. Concluding Remarks

This study provides insight into the influence of different structural metrics on membrane transport. Flux performance is largely affected by ICP and thus membrane structure optimization efforts should focus on effective ways of mitigating this detrimental phenomenon. This was seen to be best done by decreasing support thickness over either increasing porosity or support pore radius. The results also indicate that there is a need to look beyond the traditional optimization of thickness, tortuosity and porosity as even parameters like support pore radius, which do not feature in the intrinsic structural parameter formula, seem to affect performance to a non-insignificant degree. Future osmotic membrane designers could benefit from these findings when weighing the effects of manipulating one parameter versus another.

References

1. Frank, B.S., *Desalination of sea water*. 1972, US Patent 3,670,897.
2. Jellinek, H.H.G., *Osmosis process for producing energy*. 1976, US Patent 3,978,344.
3. Kessler, J.O. and C.D. Moody, *Drinking water from sea water by forward osmosis.* Desalination, 1976. **18**(3): p. 297-306.
4. Loeb, S., *Method and apparatus for generating power utilizing pressure-retarded-osmosis*. 1975, US Patent 3,906,250.
5. McGinnis, R.L., *Osmotic desalination process*. 2011, US Patent 8,002,989.
6. Stache, K., *Apparatus for transforming sea water, brackish water, polluted water or the like into a nutrious drink by means of osmosis*. 1989, US Patent 4,879,030.
7. Weingarten, M.H. and R.J. Weingarten, *Power generating means*. 1971, US Patent 3,587,227.
8. Yaeli, J., *Method and apparatus for processing liquid solutions of suspensions particularly useful in the desalination of saline water*. 1992, US Patent 5,098,575.
9. Cath, T.Y., A.E. Childress, and M. Elimelech, *Forward osmosis: principles, applications, and recent developments.* Journal of membrane science, 2006. **281**(1): p. 70-87.
10. Cath, T.Y., M. Elimelech, J.R. McCutcheon, R.L. McGinnis, A. Achilli, D. Anastasio, A.R. Brady, A.E. Childress, I.V. Farr, and N.T. Hancock, *Standard methodology for evaluating membrane performance in osmotically driven membrane processes.* Desalination, 2012. **312**: p. 31-38.
11. Wong, M.C.Y., K. Martinez, G.Z. Ramon, and E. Hoek, *Impacts of operating conditions and solution chemistry on osmotic membrane structure and performance.* Desalination, 2012. **287**: p. 340-349.
12. Manickam, S.S., J. Gelb, and J.R. McCutcheon, *Pore structure characterization of asymmetric membranes: Non-destructive characterization of porosity and tortuosity.* Journal of membrane science, 2014. **454**: p. 549-554.
13. Ramon, G.Z., M.C.Y. Wong, and E. Hoek, *Transport through composite membrane, part 1: Is there an optimal support membrane?* Journal of membrane science, 2012. **415**: p. 298-305.

14. Ghosh, A.K. and E. Hoek, *Impacts of support membrane structure and chemistry on polyamide-polysulfone interfacial composite membranes.* Journal of membrane science, 2009. **336**(1): p. 140-148.
15. Singh, P.S., S.V. Joshi, J.J. Trivedi, C.V. Devmurari, A.P. Rao, and P.K. Ghosh, *Probing the structural variations of thin film composite RO membranes obtained by coating polyamide over polysulfone membranes of different pore dimensions.* Journal of membrane science, 2006. **278**(1): p. 19-25.
16. Tiraferri, A., N.Y. Yip, W.A. Phillip, J.D. Schiffman, and M. Elimelech, *Relating performance of thin-film composite forward osmosis membranes to support layer formation and structure.* Journal of membrane science, 2011. **367**(1): p. 340-352.
17. Bui, N.-N. and J.R. McCutcheon, *Hydrophilic nanofibers as new supports for thin film composite membranes for engineered osmosis.* Environmental science & technology, 2013. **47**(3): p. 1761-1769.
18. Huang, L., N.-N. Bui, M.T. Meyering, T.J. Hamlin, and J.R. McCutcheon, *Novel hydrophilic nylon 6, 6 microfiltration membrane supported thin film composite membranes for engineered osmosis.* Journal of membrane science, 2013. **437**: p. 141-149.
19. Bui, N.-N., *Engineered Osmosis for Sustainable Water and Energy: Novel Nanofiber-supported Thin-film Composite Membrane Design & Updated Flux Model Proposal*. 2013, University of Connecticut: Storrs.

Chapter 8

Conclusions and Recommendations

8.1 Concluding remarks

This dissertation focuses on an important but oft-neglected area in applications involving soft materials – comprehensive structural characterization. The structures of asymmetric membranes, employed in osmotic separations, were examined in detail and their relation to transport phenomena in such materials was studied. Early work on the fabrication and characterization of ACNFN as an anode material for MFCs served as the motivation for examining the impact of structure on transport in soft materials. The porous structure of the carbon nanofibers-based nonwoven, along with its large bioaccessible surface areas resulted in impressive electrochemical performances in lab-scale MFC testing. Following this study, pore structure characterization of asymmetric membrane materials were used to understand the effect of structure on transport phenomena. Direct approaches of characterizing membrane materials revealed that the alternate, commonly-used indirect methods (i.e. semi-empirical models) were fraught with several limitations thus making analyses based on the resulting information severely flawed. This is worrisome since membrane scientists rely on the results of the semi-empirical approaches to inform further membrane design. The study on numerical transport modeling and simulation also revealed that there exist other facets of membrane structures whose design optimization would yield benefits in performance. The study proved to be also be insightful in revealing that the different structural features exhibited varying levels of impact on performance and thus need to be weighted differently during membrane design. Finally, while the structural characterization approaches developed in this work used asymmetric membranes used in EO as a platform, these methods can be readily extended to other soft materials used in separations technologies.

8.2 Recommendations

There were a number of interesting preliminary results and experimental observations noticed during this study that require further consideration to advance the field of engineered osmosis.

8.2.1 Future studies on ACNFN

It was observed that mechanical strength was a key limiting factor in applying novel materials, like ACNFN in different applications, for e.g. in MFCs. Nanofibrous nonwovens inherently have low strength and the pyrolysis steps involved in fabricating ACNFN further weaken the material. One alternative could be to increase carbonization times high enough to graphitize the material, however, it is expected that the increase in strength will only occur along one axis and not uniformly across the structure. Possible avenues for increasing strength could be to look at bigger fiber sizes in the precursor nonwoven, milder methods of activation, using composite nanofibers as the precursor or tuning the chemistry of the precursor polymer in order to achieve highly cross-linked nanofibers. Alternatively, pyrolysis at reduced temperatures could also be considered which is expected to not significantly reduce the conductivity of the final material (due to incomplete removal of non-carbon atoms), should conductivity be an important factor in applications where ACNFN is used as an electrode material. In any application where the high surface area aspect of ACNFN is sought to be used it is to be noted that there will always be a trade-off between surface area and strength and these two parameters then need to be optimized according to the specific needs.

8.2.1 Future directions for characterizing soft materials

Soft materials characterization is a challenging field with several restrictions on both sample preparation as well as the applicability of techniques. While this dissertation has addressed many

of those challenges there are a lot more avenues that can be explored. Particularly, in the case of membranes used for water treatment there has always been an interest to characterize membranes in their hydrated state since that is their working state. Characterizing wetted soft materials could be done using both analytical and imaging methods. Among the analytical methods, the only technique currently available is a water intrusion porosimeter, the Aquapore from Porous Materials Inc., Ithaca, NY. This is similar in principle to the MIP except that here instead of mercury, water is used as the intrusion test liquid. Two main limitations remain: one is the high test pressures required that pose dangers of sample compression and distortion. Secondly, all analytical techniques use assumptions of cylindrical pore geometries that can be highly idealistic especially for some of the more complex pore structures. Additionally, there is always an interest to visualize wetted pore structures rather than to merely derive quantitative data on the same. Some of the imaging options available are Confocal laser scanning microscopy (CLSM), environmental SEM (ESEM) and XCT. CLSM has been used previously to characterize wetted EO membranes, however optics based techniques have certain resolution limitations that can cause the 2D slices to be less informative as we move deeper into the structure. With ESEM, the issue has been with operating in a non-vacuum state in the sample chamber. Some chamber pressure is required in order to keep the water used for hydrating the sample in the liquid state. This air pressure causes the electron beam to scatter thus significantly reducing the resolution of the otherwise-successful electron optics-based technique. The last option available is XCT which also poses significant challenge with respect to sample preparation and contrast obtainable. The three phases that we're trying to differentiate – air, water and polymer – all have densities relatively close to one another and since XCT works by obtaining contrast as a result of density differences such three-phase studies can be challenging. A recommended rule-of-thumb is

having at least a 0.2-0.3 g/cc difference in density between the different phases that need to be identified. This is usually hard in the case of most polymeric membranes, with the density differences lying barely above this minimum target. Several iterations were made as part of my research work on sample stages and configurations that can be used to obtain the best possible x-ray transmissions and pixel counts with limited success. Imaging wetted membranes is an arduous task that involves a number of iterations in both experiment setup and sample preparation in order to obtain an optimum recipe and decent final image quality. However, it is not impossible to do this since some of the initial trials in my work have shown some promise in this regard.

8.2.3 Future directions in membrane structure optimization for EO

Some areas of future work in the field of membrane structure optimization and fabrication for EO are also suggested here. From the work outlined in Chapter 7 it was seen that support layer thickness played a more prominent role in reducing ICP severity over either porosity or support pore radius. This simulated result was in fact experimentally observed by Bui [ref] in work on nanofiber-supported TFC EO membranes. This is an interesting result in light of the fact that both highly porous serve to reduce mechanical strength. A trade-off between porosity and thickness in favor of the latter could perhaps help offset some of the strength issues associated with newer, more novel supports while still maintaining their superior transport behaviors. Further, the results of Chapter 7 showed, for the first time quantitatively it is believed, that there is a need to look beyond the traditional optimization of thickness, tortuosity and porosity as even parameters like support pore radius, which do not feature in the intrinsic structural parameter formula, seem to affect performance to a non-insignificant degree. A detailed experimental study where support pore radii are systematically changed and the resulting changes (if any) in

performance are noted will help to validate the claim made using numerical methods. Lastly, for the work on fabricating TFC membranes, in Chapter 6, I initially explored layer-by-layer deposition (LbL) techniques for forming the selective layer. While the support material used may not have been conducive for LbL, there have been other studies, at the National Institute of Standards and Technology, where a stand-alone polyamide layer was formed using LbL methods and their mechanical properties tested. A free-standing selective layer remains the ultimate goal of researchers in the EO community and if some work is begun in this area it could be the first step in a long process to realize that dream. Perhaps even up to 100 LbL layers could be formed that would, upon sufficient cross-linking be able to negate the need for a support layer, thus eliminating the drawbacks of the ICP phenomenon altogether.